

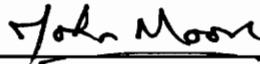
**3-D Flow and Performance of a Rocket Pump Inducer
at Design and Off-Design Flow Rates**

by

Andrew W. Doan

Thesis submitted to the Faculty of the
Virginia Polytechnic Institute and State University
in partial fulfillment of the requirements for the degree of
Master of Science
in
Mechanical Engineering

APPROVED:



Dr. John Moore, Chairman



Dr. Eugene F. Brown



Dr. Clinton L. Dancey

August 1994
Blacksburg, Virginia

C.2

LD
S655
V855
1994
D636
C.2

3-D Flow and Performance of a Rocket Pump Inducer at Design and Off-Design Flow Rates

by

Andrew W. Doan
Dr. John Moore, Chairman
Mechanical Engineering

(ABSTRACT)

The ADP rocket pump inducer was studied computationally using a 3-D Navier-Stokes solver, The Moore Elliptic Flow Program. Design and off-design flow rates were simulated to qualitatively and quantitatively study the effects of flow rate on the flow and performance. Several views of the results were created to aid flow visualization.

The 3-D laser measurements made by Rocketdyne were used for comparison. The velocity magnitudes as well as the flow patterns within the inducer match well between the calculated and measured results. The axial velocity distribution and the rotary stagnation pressure, losses, are predicted very well by the calculation.

The internal flow patterns developed in the simulation as expected, with radial outflow in the blade boundary layers. The tip leakage flow formed a recirculation region, a toroidal shaped vortex at the tip leading edge of the blades. The associated backflow forms a blockage which varies with flow rate.

The thermodynamic performance was evaluated by calculating the contributions to pressure rise, the pump characteristic, the contributions to moment of momentum, and the efficiency. The centrifugal effect and relative velocity effect were found to vary with flow rate. The effective inlet throat radius, which governs these two effects, changes with flow rate because of the recirculation blockage. The shear on the blades was found to produce a small fraction of the work in the inducer, and most was produced by the pressure difference across the blade. The inducer efficiency was about 89%, and increased with decreasing flow rate in the range of flow rates considered, from 89% to 110% of the design flow rate.

Acknowledgements

I would like to thank God, and all those who helped me through this year of graduate studies. Special thanks go to Dr. John Moore and Joan Moore for their timely guidance and words of wisdom, and for always being cheerful and encouraging. Dr Moore "led me in the paths of righteousness", as he would say. Under his direction I was never overwhelmed with large projects and distant goals. He always kept me focused on the next task at hand. Joan took the pain out of learning how to use the workstation for flow modeling. This project would not have been possible without her patient teaching and vast knowledge of the workstation. I also thank Dr. Brown and Dr. Dancey for being on my advisory committee. I would also like to thank Tony Eastland, Lou Rojas, and Laura Brozowski of the Rocketdyne Division of Rockwell International Corporation, and Robert Garcia of the NASA Marshall Pump Consortium for their support for this project and providing the geometry and data for the Rocketdyne inducer test.

TABLE OF CONTENTS

1	INTRODUCTION
2	LITERATURE REVIEW
	2.1 Experimental Inducer Studies
	2.2 Computational Inducer Studies
	2.3 The Moore Elliptic Flow Program (MEFP)
	2.4 Definitions of Pressures and Kinetic Energies
3	SCOPE AND OBJECTIVES OF THIS THESIS
4	GEOMETRY AND GRID
	4.1 Calculation Grid Generation
	4.2 Calculation Grid
	4.3 Calculation Details
5	CALCULATION RESULTS
6	COMPARISON OF CALCULATION TO MEASUREMENT
	6.1 Comparison of Internal Data Planes
	6.2 Comparison of Overall Performance
7	RECIRCULATION
8	THERMODYNAMIC PERFORMANCE
	8.1 Mass Averaged Properties
	8.2 Contributions to Static and Total Pressure Rise
	8.3 Pump Characteristic
	8.4 Moment of Momentum
	8.5 Efficiency
9	CONCLUSIONS
	BIBLIOGRAPHY
	APPENDIX A
	Derivation of the Tangential Moment of Momentum Equation
	APPENDIX B
	Rotary Stagnation Pressure, P^* , loss
	VITA

LIST OF FIGURES

- Figure 1.1 ADP inducer designed by Rocketdyne
- Figure 1.2 Photograph of Rocketdyne inducer
- Figure 2.1 Inducer flow patterns (reference 4)
- Figure 2.2 Reverse flow catchers, and their location (reference 5)
- Figure 2.3 Four axial measurement planes on a Worthington Pump Inducer (reference 6)
- Figure 2.4 Velocity contour plot for flow coefficient $\phi = .129$, Worthington Pump Inducer (reference 6)
- Figure 2.5 Velocity contour plot for flow coefficient $\phi = .109$, Worthington Pump Inducer (reference 6)
- Figure 2.6 The SEP inducer (reference 8)
- Figure 2.7 Meridional views of the calculated velocity vectors at mid-passage, near the blade pressure side and suction side, SEP inducer (reference 8)
- Figure 2.8 Secondary velocities in 3 iso-theta planes, SEP inducer (reference 8)
- Figure 2.9 Tip leakage velocity vectors, SEP inducer (reference 8)
- Figure 2.10 Contributions to work input through the SEP inducer (reference 9)
- Figure 2.11 Development of performance parameters through the SEP inducer (reference 9)
- Figure 4.1 The Rocketdyne inducer test setup (reference 17)
- Figure 4.2 Rocketdyne inducer geometry (reference 17)
- Figure 4.3 6 laser velocimetry measurement planes within the inducer, and one at the impeller inlet plane (reference 17)

- Figure 4.4 Very dense blade geometry grid from Rocketdyne
- Figure 4.5 Leading and trailing edge shapes
- Figure 4.6 Meridional view (r vs z) of the un-meshed calculation region
- Figure 4.7 Meridional view (r vs z) of the optimized grid
- Figure 4.8 Meridional view (r vs z) of the final design flow rate calculation grid
- Figure 4.9 Meridional view of the calculation grid for the 89% flow rate
- Figure 4.10 Blade-to-blade view ($r\theta$ vs z) of the blade tip leading edge and an axial view (x vs y) of a constant i plane
- Figure 4.11 Blade shape at the leading and trailing edge, and the tip gap
- Figure 4.12 Inlet plane velocity values (reference 16)
-
- Figure 5.1 Meridional view near pressure surface of calculated velocity vectors at design flow rate.
- Figure 5.2 Meridional view near suction surface of calculated velocity vectors at design flow rate.
- Figure 5.3 Meridional view at mid-passage of calculated velocity vectors at design flow rate.
- Figure 5.4 Meridional slices showing P^* at design flow rate
- Figure 5.5 Meridional view near pressure surface of calculated P^* with velocity vectors at design flow rate.
- Figure 5.6 Meridional view near suction surface of calculated P^* with velocity vectors at design flow rate.
- Figure 5.7 Meridional view at mid-passage of calculated P^* with velocity vectors at design flow rate.

- Figure 6.1 Axial comparison plane at $z/D = -0.0083$ showing calculated and measured velocity components at design flow rate.
- Figure 6.2 Axial comparison plane at $z/D = 0.1222$ showing calculated and measured velocity components at design flow rate.
- Figure 6.3 Axial comparison plane at $z/D = 0.1790$ showing calculated and measured velocity components at design flow rate.
- Figure 6.4 Axial comparison plane at $z/D = 0.2925$ showing calculated and measured velocity components at design flow rate.
- Figure 6.5 Axial comparison plane at $z/D = 0.4644$ showing calculated and measured velocity components at design flow rate.
- Figure 6.6 Circumferentially averaged pressures and velocities at impeller inlet survey plane; comparison of calculated and measured:
 - tangential, radial, and axial velocities
 - static, total, rotary stagnation, and reduced pressures
- Figure 7.1 Blade-to-blade view showing tip leakage flow
- Figure 7.2 Meridional views of calculated static pressure at design flow rate. 12 view locations from the suction surface to the pressure surface, labeled in percent of the blade spacing
- Figure 7.3 Meridional view near pressure surface of calculated velocity vectors at 110% flow rate.
- Figure 7.4 Meridional view near suction surface of calculated velocity vectors at 110% flow rate.
- Figure 7.5 Meridional view at mid-passage of calculated velocity vectors at 110% flow rate.
- Figure 7.6 Meridional slices showing P^* at 110% flow rate
- Figure 7.7 Meridional view near pressure surface of calculated velocity vectors at 89% flow rate.
- Figure 7.8 Meridional view near suction surface of calculated velocity vectors at 89% flow rate.

- Figure 7.9 Meridional view at mid-passage of calculated velocity vectors at 89% flow rate.
- Figure 7.10 Meridional slices showing P^* at 89% flow rate
- Figure 7.11 Backflow normalized with flow rate, plotted as a function of the axial parameter, A , at 89%, design, and 110% flow rates
- Figure 8.1 The development of the pressures as a function of the axial parameter, A , at 89% flow rate
- Figure 8.2 The development of the pressures as a function of the axial parameter, A , at design flow rate
- Figure 8.3 The development of the pressures as a function of the axial parameter, A , at 110% flow rate
- Figure 8.4 Pump Characteristic - static pressure rise characteristic plotted as a function of flow rate
- Figure 8.5 Pump Characteristic - total pressure rise characteristic plotted as a function of flow rate
- Figure 8.6 Velocity triangles showing the recirculation region blockage effects
- Figure 8.7 Development of work through the inducer

LIST OF TABLES

Table 4.1	Table of inducer parameters
Table 8.1	Mass averaged pressures and velocities in the inducer
Table 8.2	Components of static pressure rise
Table 8.3	Components of total pressure rise
Table 8.4	Moment of momentum components through the inducer

NOMENCLATURE

ADP	=	Advanced Design Project	
r	=	radius, or radial direction	
θ	=	theta angle, or tangential direction	
z	=	axial distance, or axial direction	
\mathbf{m}_r	=	unit vector in the radial direction	
\mathbf{m}_θ	=	unit vector in the tangential direction	
\mathbf{m}_z	=	unit vector in the axial direction	
i	=	axial grid index	
j	=	blade-to-blade grid index	
k	=	hub-to-shroud grid index	
A	=	axial distance parameter	Section 4.1
B	=	blade-to-blade distance parameter	Section 4.1
C	=	hub-to-shroud distance parameter	Section 4.1
U	=	blade velocity	
W	=	relative velocity	
V	=	absolute velocity	
V_r	=	absolute velocity in the radial direction	
V_θ	=	absolute velocity in the tangential direction	
V_z	=	absolute velocity in the axial direction	
ϕ	=	flow coefficient	V_x/U_{tip}
\dot{m}	=	flow rate	
ρ	=	density	
μ	=	viscosity	
T	=	temperature	
R	=	ideal gas constant	
H	=	rothalpy	
c_p	=	specific heat	

s	=	entropy	
L	=	mixing length	
N	=	angular velocity (rpm)	
ω	=	angular velocity (rad/s)	
Re_D	=	Reynolds number = $\rho U_{tip} d / \mu$	
P	=	static pressure	Section 2.4
P_t	=	total pressure	Section 2.4
P_r	=	reduced pressure	Section 2.4
P^*	=	rotary stagnation pressure	Section 2.4
P_o	=	reference pressure	Section 2.4
ψ	=	head coefficient	
η	=	efficiency	
T_p	=	torque due to pressure	
T_{Sr}	=	torque due to shear at the rotor	
T_{Ss}	=	torque due to shear at the shroud	
ψ_E	=	work coefficient	eqs. 8.3 and 8.4
ψ_{TP}	=	pressure torque coefficient	eqs. 8.3 and 8.4
ψ_{TSr}	=	rotor shear torque coefficient	eqs. 8.3 and 8.4
ψ_{TSs}	=	shroud shear torque coefficient	eqs. 8.3 and 8.4
ψ_t	=	total pressure coefficient	eq. 8.6
ψ_{loss}	=	loss coefficient	eq. 8.7

1 INTRODUCTION

Rocket engines require high specific power turbine pumps to deliver a large amount of fuel to the nozzle in a short time. The cryogenic fuel is stored at 30 psia to reduce the storage tank weight. At these low pressures the liquid hydrogen and oxygen are near the boiling point and cavitation is inevitable. Cavitation degrades the performance of the turbine pump, therefore, it is desirable to reduce or even eliminate cavitation from the pump. A cavitating inducer upstream of the pump eliminates cavitation in the main impeller by increasing the pressure of the fluid beyond the cavitation point of the main impeller. Cavitation still occurs in the inducer but is usually contained along the inducer suction surface.

Inducers usually have 3 to 4 blades that each wrap almost completely around the hub. The blade angle and the solidity are typically high because inducers are designed for a low flow coefficient. The passages between the blades are sufficiently long and narrow to allow the cavitation bubbles to collapse before the exit.

Computational Fluid Dynamics, CFD, has become more accurate and less time consuming. With improvements in programming and hardware, flow programs can now run effectively in a workstation environment. The design process can be improved and shortened by using CFD. Also, the testing necessary for a new component may be reduced to the areas of interest revealed by the computational analysis.

CFD routinely provides velocity, pressure, and loss information anywhere in the flow. Computational analysis is capable of revealing much more detail about a flow than an experiment. Flow measurement techniques for experimentation have improved as well. The state of the art 3-D laser velocimeter can measure internal flow, but only provides velocities. Furthermore, the laser anemometer is disrupted by regions of strong turbulence, or cavitation, and can not penetrate areas hidden behind blade structure. Even so, experimentation is still very important for verifying calculation results and revealing calculation errors.

A cavitating inducer designed by Rocketdyne, Figures 1.1 and 1.2, was analyzed computationally in this research. The same inducer was tested experimentally by Rocketdyne using 3-D laser anemometry to investigate the 3-D flow within the inducer passages. The detailed measurements were also intended to validate the 3-D flow code used in this research, as well as any other codes that may be capable of inducer design and analysis. This is a rare opportunity to use highly detailed laser measurements for flow code validation.

The thesis begins with a literature review of work on inducers focusing on 3-D flow, recirculation, off-design flow, and performance analysis. The literature discussed includes examples of most experimental and computational analysis techniques.

The scope and objectives of this thesis are presented in section 3. The following section covers the generation of the computational grid and the preparation of the boundary conditions and initial conditions for the flow calculations.

The calculation results are analyzed and discussed in four sections. The first section, section 5, introduces the figures used to visualize the flow field and points out the characteristics of the typical inducer flow patterns. Section 6 is the comparison of the calculated flow field to the measured flow field. The comparison was made to validate the Moore Elliptic Flow Program, which was used to calculate the flow field. Section 7 discusses the shape, sources, and effects of the leading edge recirculation region. The contributions to pressure rise, the pump characteristic, and the contributions to moment of momentum are calculated and discussed in the thermodynamic performance section, section 8.

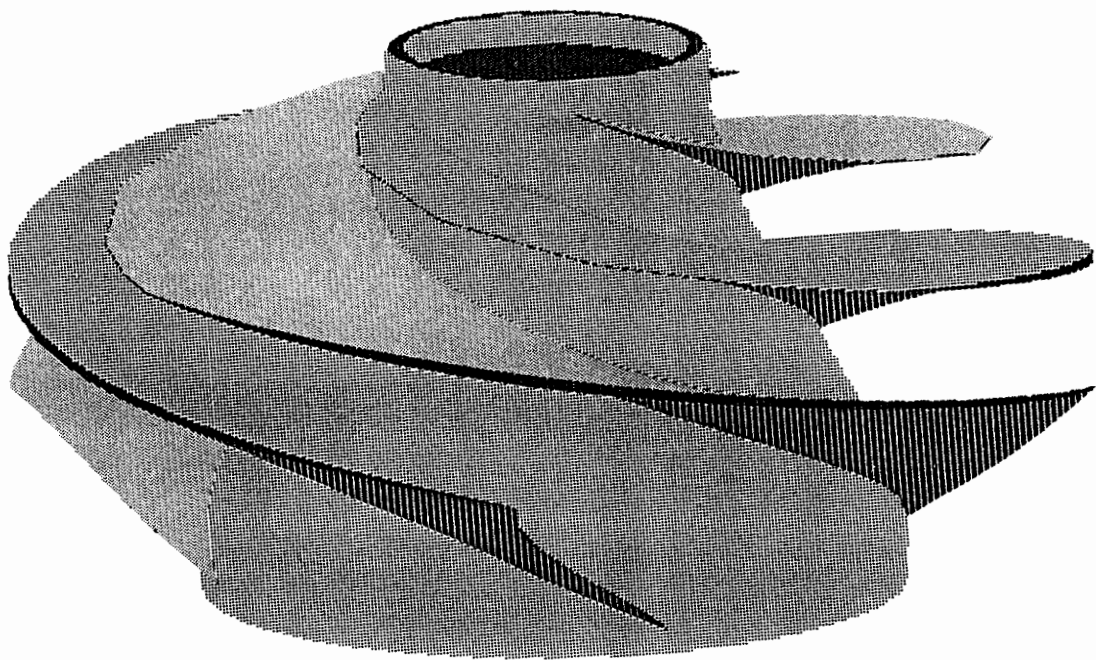


Figure 1.1 **ADP inducer designed by Rocketdyne**

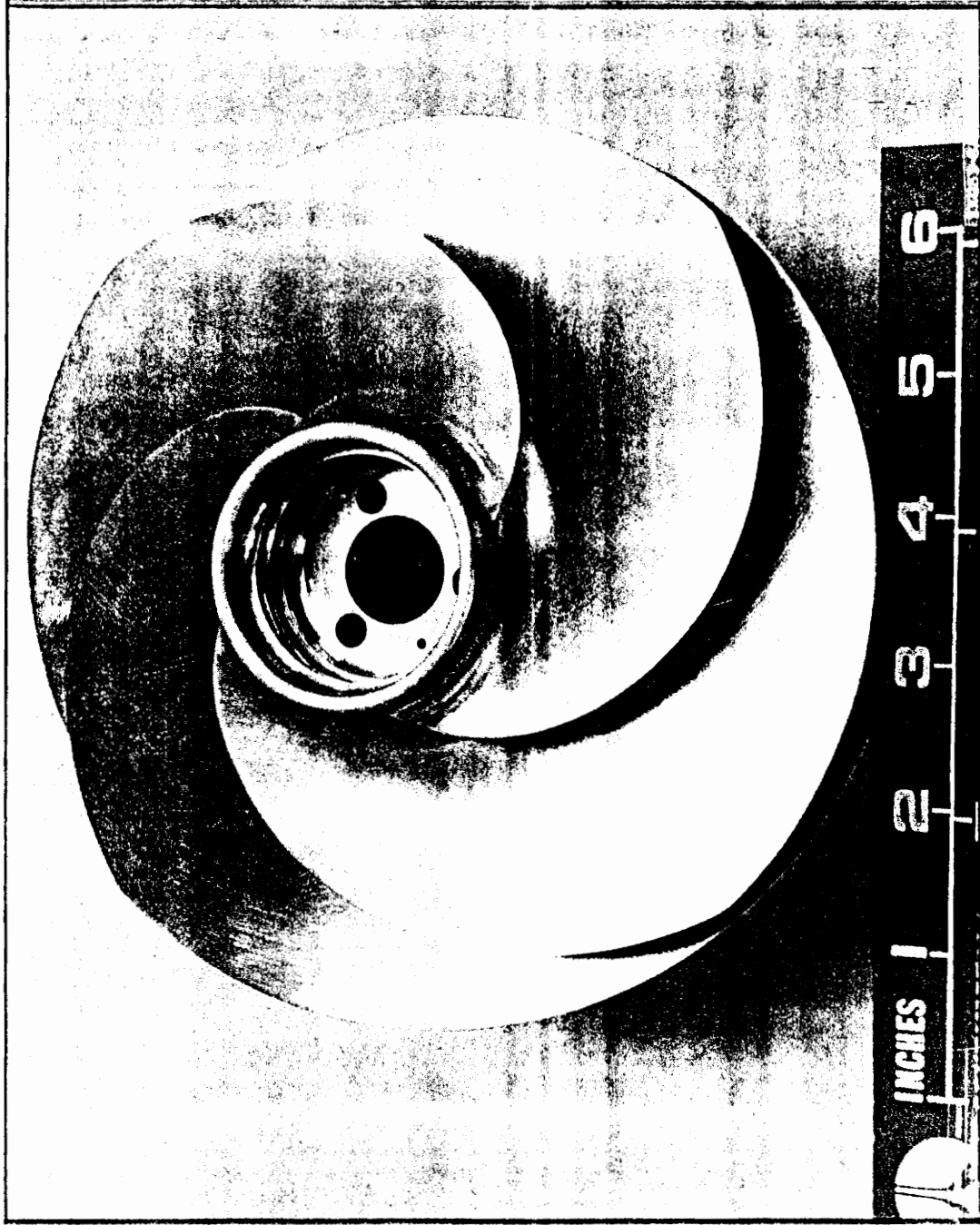


Figure 1.2 Photograph of Rocketdyne Inducer

2 LITERATURE REVIEW

It has been known that axial inducers operate well under cavitating conditions. For this reason axial inducers have been used to pump fluid that is close to boiling. For example, cryogenic fuel and oxidizer for a rocket is pumped to the burner by rocket turbine pumps. The fuel is stored at 30 psia to reduce storage tank weight. At this low pressure the fuel is close to boiling and cavitation is inevitable. Therefore axial inducers are used in the first stage of the turbine pump to avoid cavitation in the main impeller. Furst of Rocketdyne (1,2), in the design of the Space Shuttle Main Engine, used axial inducers in the first stage of the liquid hydrogen and oxygen rocket turbine pumps. NASA has been interested in axial inducers for rocket pump applications and has funded inducer research for about forty years.

2.1 Experimental Inducer Studies

The flow field within an inducer is complex, and has taken some time to understand. Lakshminarayana (3,4) at Pennsylvania State University studied the flow field within an inducer from 1964 to 1982. The results of his studies, as well as others, have shown the flow through an inducer is turbulent, and three-dimensional in nature. Also, the viscous shear is significant due to the very long blade surfaces. The radial velocities are of the same order of magnitude as the axial velocities. Shown in Figure 2.1, the secondary flow is radially outwards along the blade surfaces and radially inwards at mid-passage.

Backflow is also found to occur at the tip leading edge, and increases as the flow rate is reduced below the design flow. The area where backflow occurs is also known as the recirculation region. Following Lakshminarayana's studies, this recirculation region was studied by Tanaka 1980, Carey 1985, Howard 1987, and Perdichizzi 1989 (see reference 6).

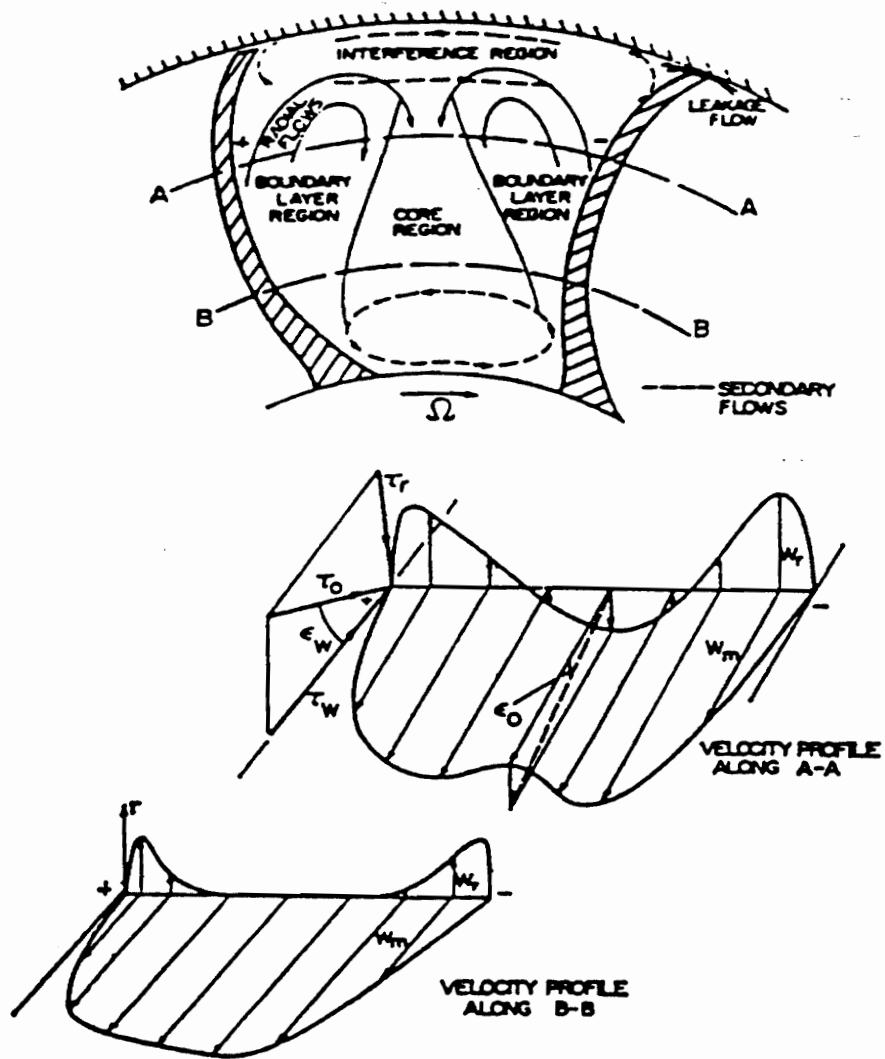
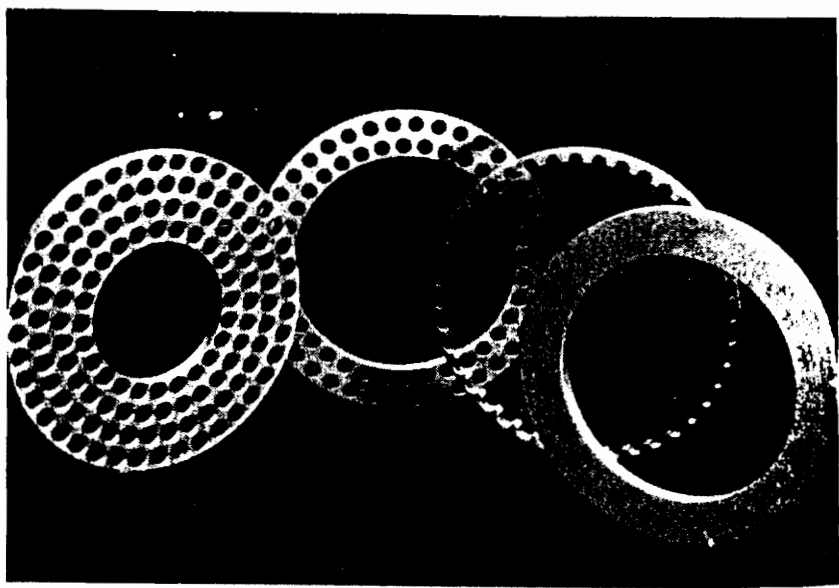
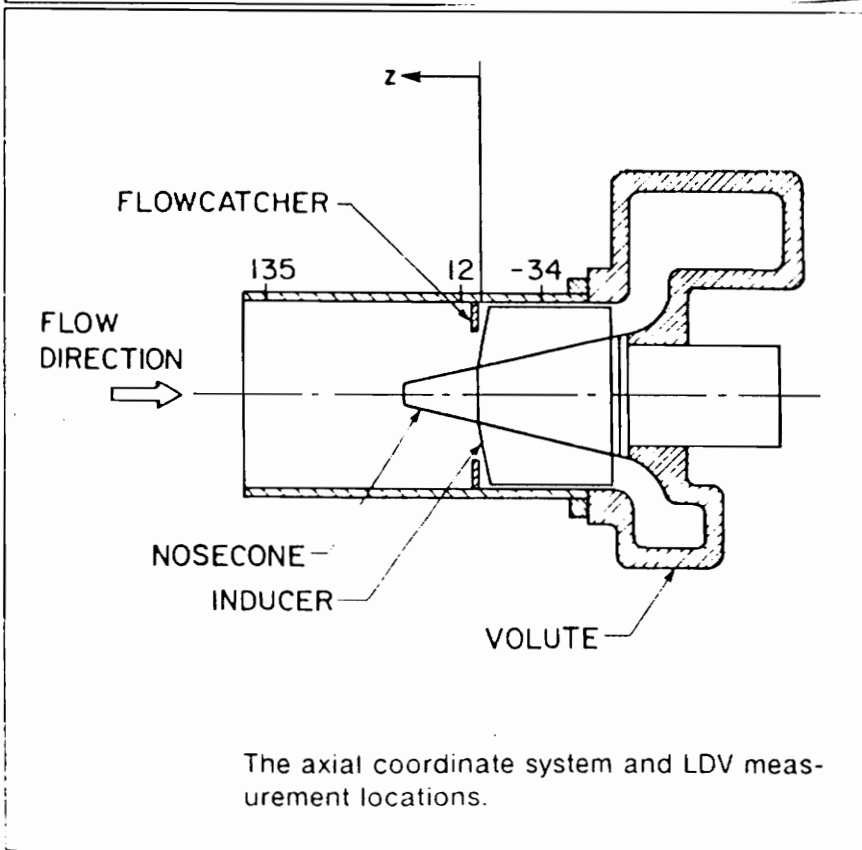


Figure 2.1 Inducer flow patterns (reference 4)

Recirculation has been known to affect the performance and stability of inducers, especially at low flow rates. Abramian and Howard (5) in 1988 used reverse flow catchers to reduce recirculation in an attempt to improve the performance and stability of an inducer at low flow rates. The reverse flow catcher, as shown in Figure 2.2, consists of a flat perforated disk which covers the outer fraction of the inlet annulus where backflow occurs. They found that the flow catchers did in fact stop the backflow, and improve the stability at low flow rates. The recirculation region acts as a variable blockage, while the flow catcher acts as a permanent blockage. Therefore, the minimal gains were negated by a slight degradation in performance at design flow.



The Reverse-Flow-Catchers



The axial coordinate system and LDV measurement locations.

Figure 2.2 Reverse flow catchers, and their location (reference 5)

The laser doppler velocimeter is a relatively new measurement technique, capable of measuring the flow field inside the inducer passages. In 1989, Boccazzi, Perdichizzi, and Tabacco (6) used two component laser anemometry to study the flow-field in a commercial Worthington pump inducer. This is an early and rare example of measuring an inducer internal flow field using laser anemometry. The experiments performed by Boccazzi, Perdichizzi, and Tabacco are similar to the tests done on the Rocketdyne inducer using three component laser anemometry.

The Worthington low solidity inducer was tested in water at three flow rates approaching backflow. Figure 2.3 shows the four axial measurement planes: upstream, within, and downstream of the inducer. At the flow coefficient $\phi = .109$ (66% of the design flow coefficient), the backflow is just beginning and is confined to a thin layer close to the casing. Reverse flow was detected using flow visualization with air injected at the casing wall.

Contour plots for the flow coefficient $\phi = .129$ and $.109$ are shown in Figures 2.4 and 2.5 respectively. The results at the low flow coefficient at plane A compared with those obtained at $\phi = .129$ show a significant decrease of axial velocities near the casing and an increase of negative tangential velocities which lead to high incidence angles. At plane B, low axial velocities and high positive tangential components are detected at the tip revealing an appreciable decrease of relative velocity. These features affect the flow field in the inlet region, reducing the upstream axial velocity component and producing radially inward flow. A further reduction in the flow rate would produce even smaller axial velocities, with a reverse flow in front of the blade suction side. The head rise in the inducer was observed using pressure tappings in the wall. As expected the head rise was higher at the lower flow coefficient.

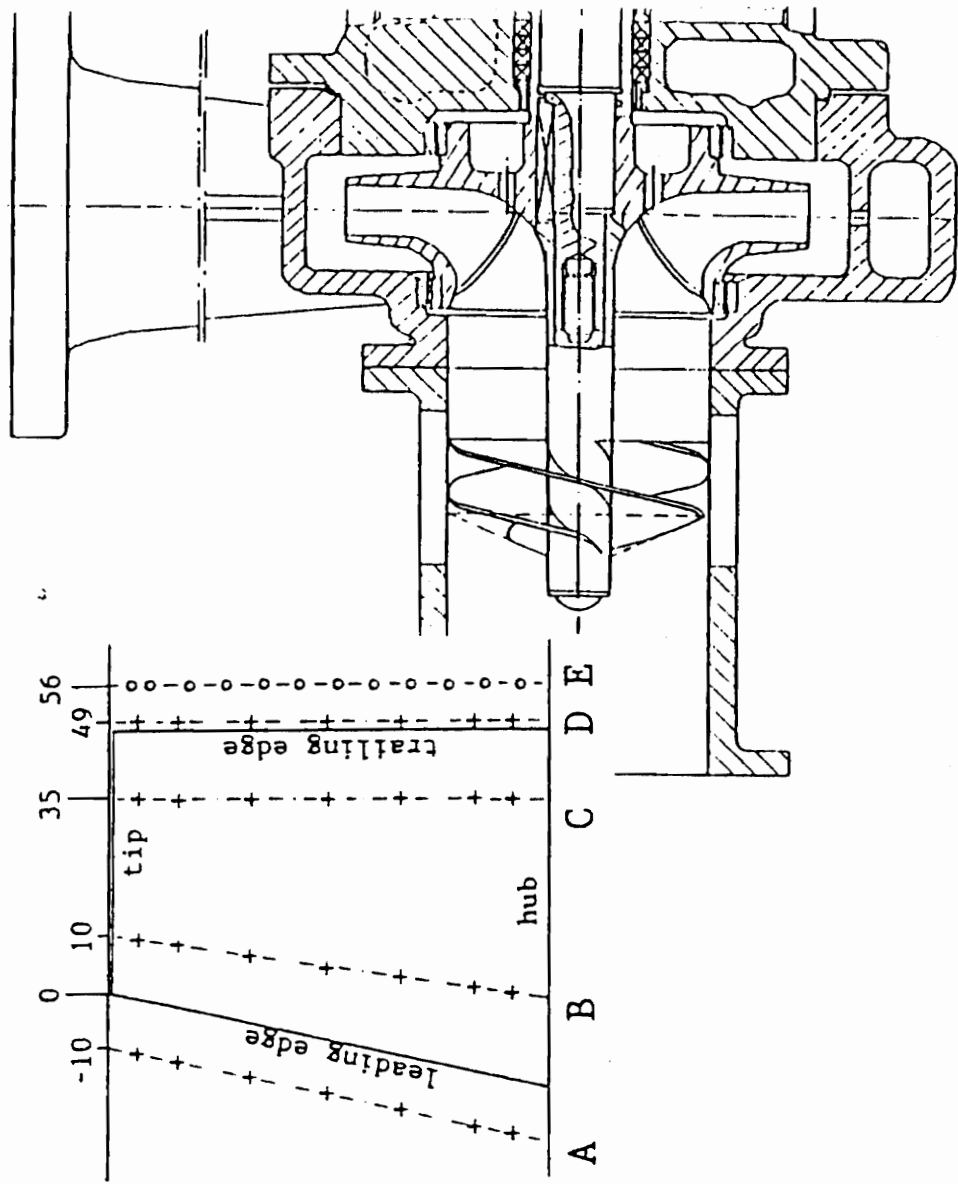


Figure 2.3 Four axial measurement planes on a Worthington Pump Inducer (reference 6)

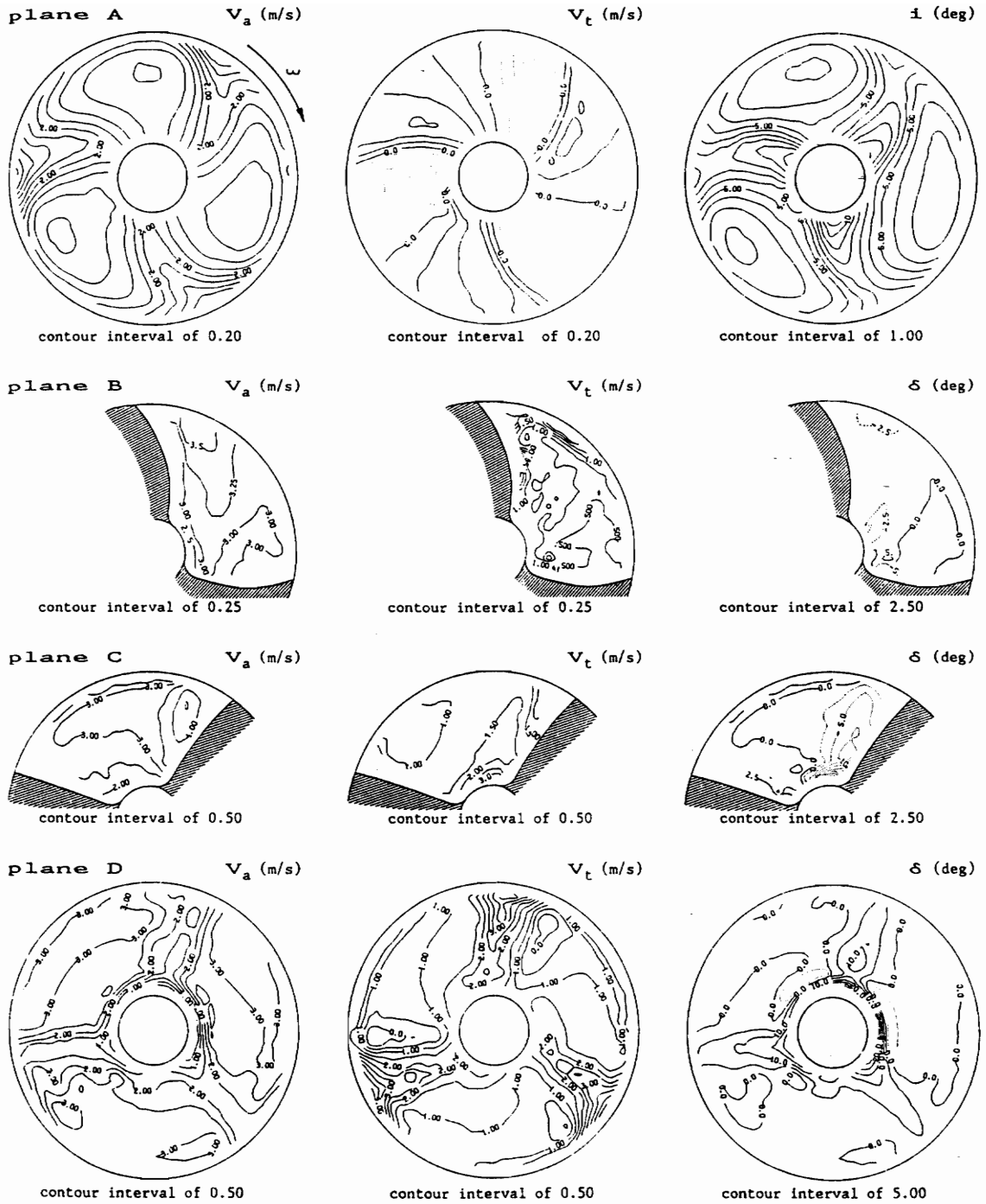


Figure 2.4 Velocity contour plot for flow coefficient $\phi = .129$
 Worthington Pump Inducer (reference 6)

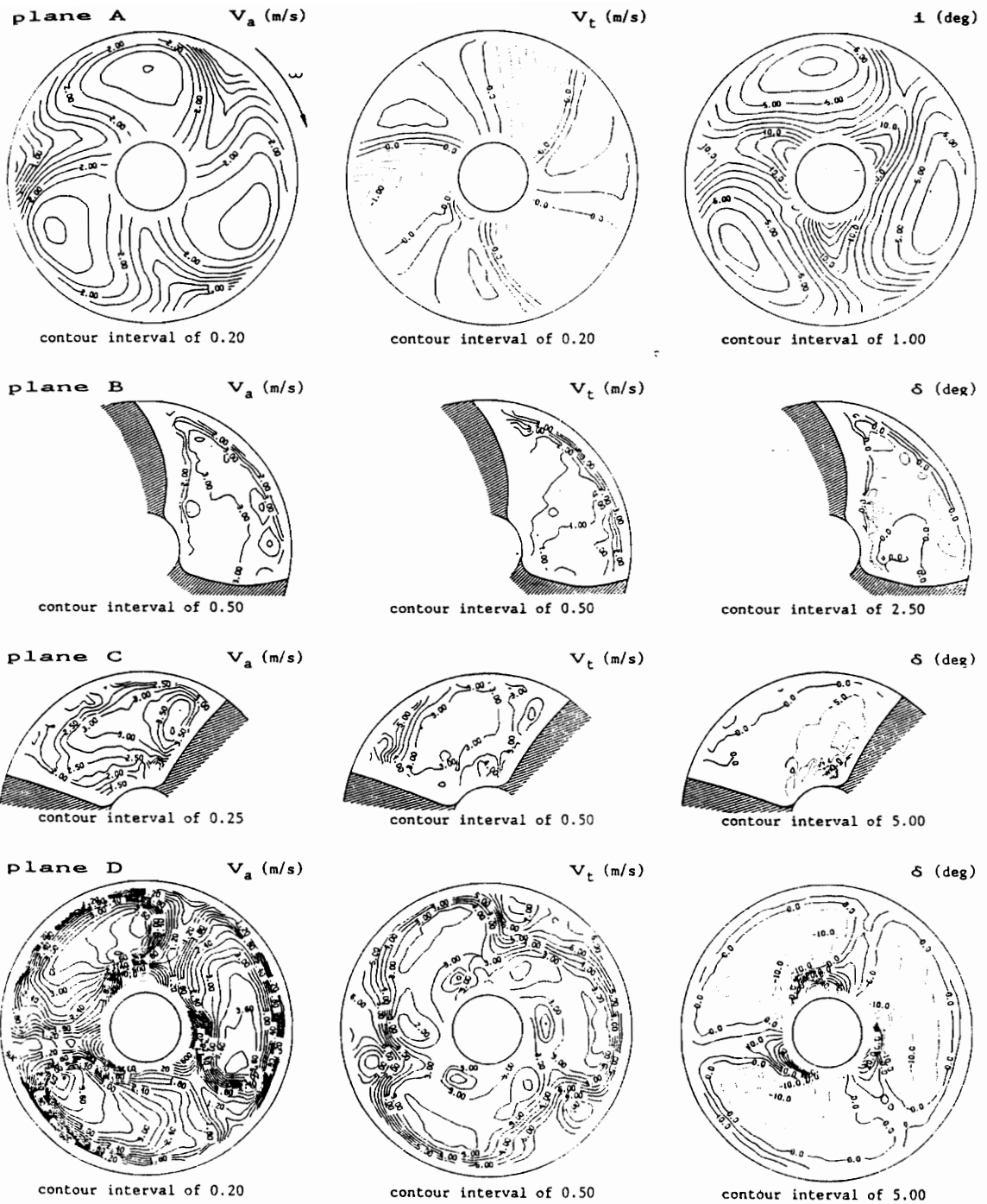


Figure 2.5 Velocity contour plot for flow coefficient $\phi = .109$
 Worthington Pump Inducer (reference 6)

2.2 Computational Inducer Studies

The inducer designed for the VULCAIN engine by the French company Societe Europeenne de Propulsion, SEP, is shown in Figure 2.6. The SEP inducer was analyzed experimentally by Bario, Barral, and Bois (7) at Lyon in 1989. The results were limited to pressure probe data at the inlet and exit which defined the overall performance of the inducer. However, the flow field within the inducer was still unknown. The SEP inducer was therefore analyzed computationally by Le Fur (8) in 1989 and Excoffon (10) in 1992 using MEFP, the Moore Elliptic Flow Program. MEFP will be discussed later in the literature review.

The calculation performed by Le Fur was probably the first of its kind and it served two purposes: to verify MEFP on the high blade angle and high solidity of an inducer, and to investigate the three-dimensional flow field in detail. The results agreed well with the air tests performed in Lyon.

Figure 2.7 shows meridional views of the calculated velocity vectors at mid-passage, near the pressure side and suction side of the blade. Figure 2.8 shows the secondary velocities in 3 iso-theta planes. The flow is radially outward on both sides of the blade and radially inward at mid-passage.

The tip leakage can also be seen in Figure 2.9. At the tip leading edge, the leakage is strong enough to produce a vortex, seen in Figures 2.7 and 2.8, which is then amplified by each leading edge. The vortex extends from blade to blade to form a torus shaped recirculation region. The recirculation region acts as a blockage causing the primary flow to enter at a smaller mean radius.

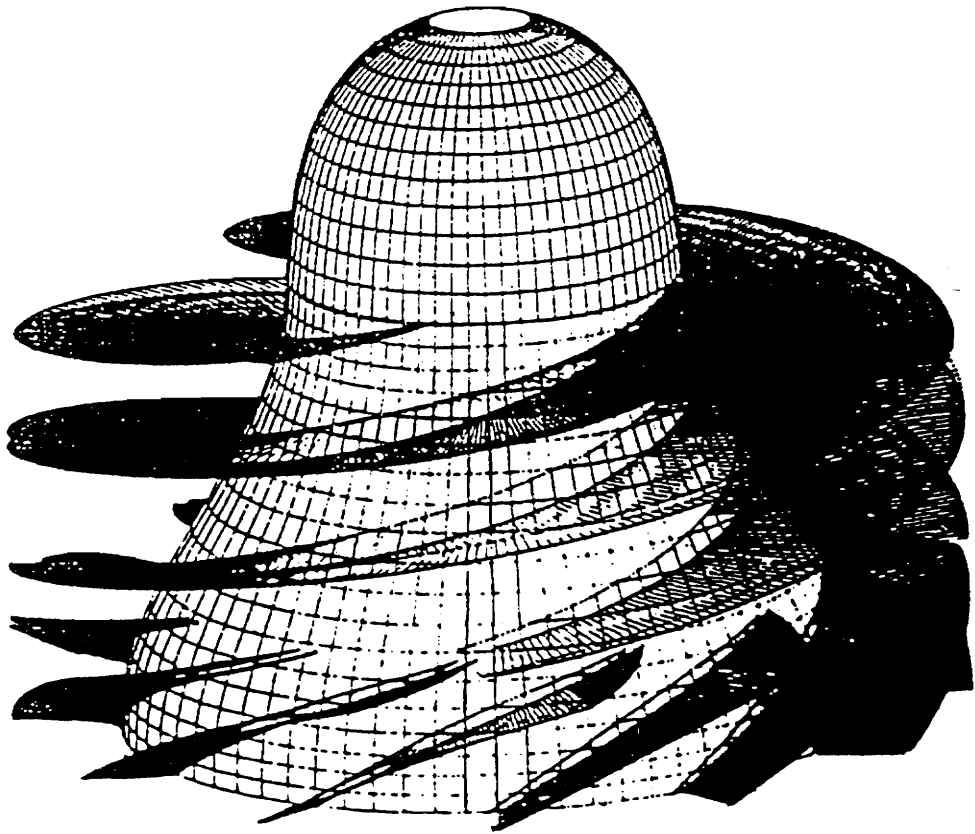


Figure 2.6

**The SEP inducer
(reference 8)**

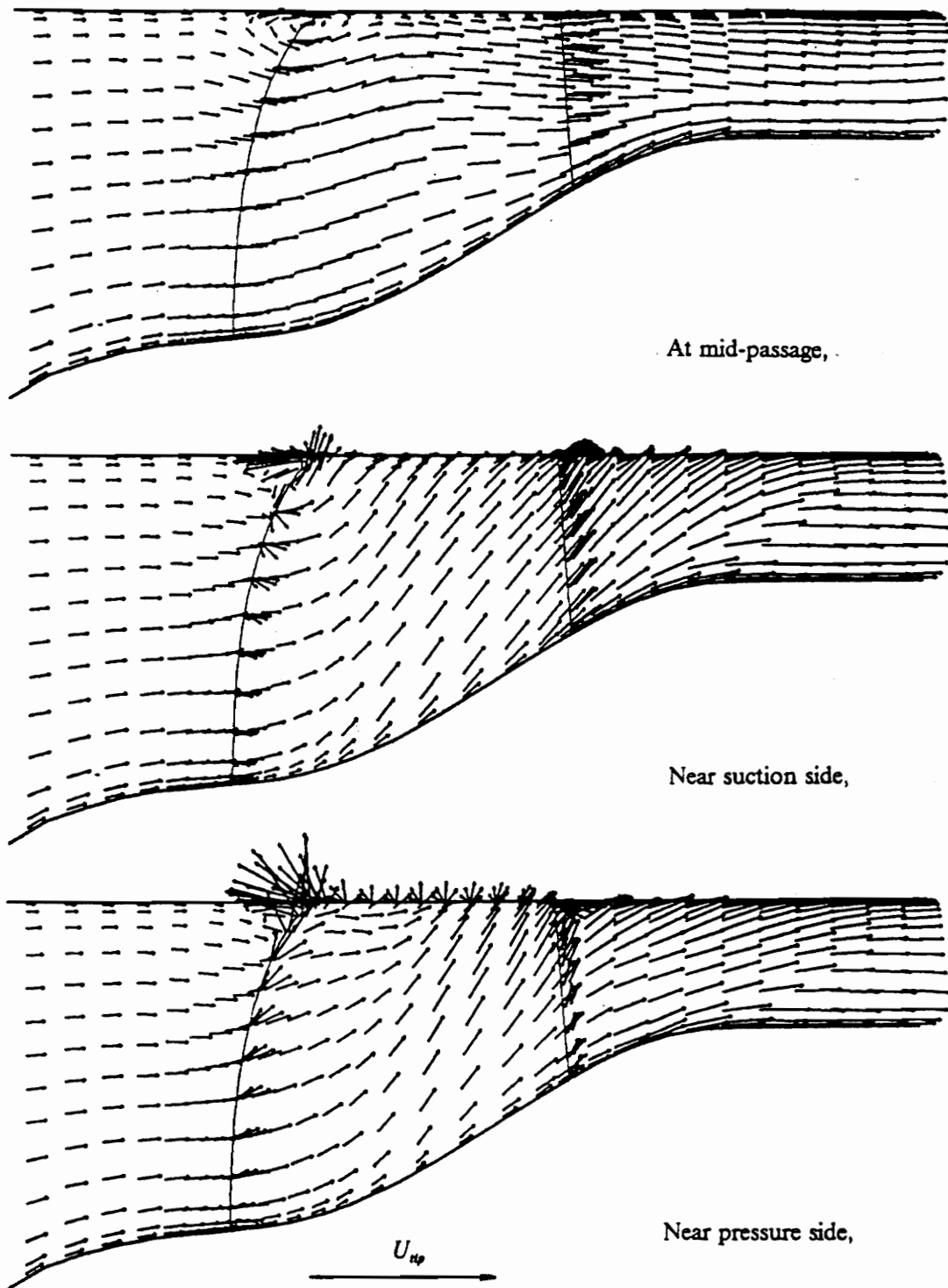


Figure 2.7 Meridional views of the calculated velocity vectors SEP inducer (reference 8)

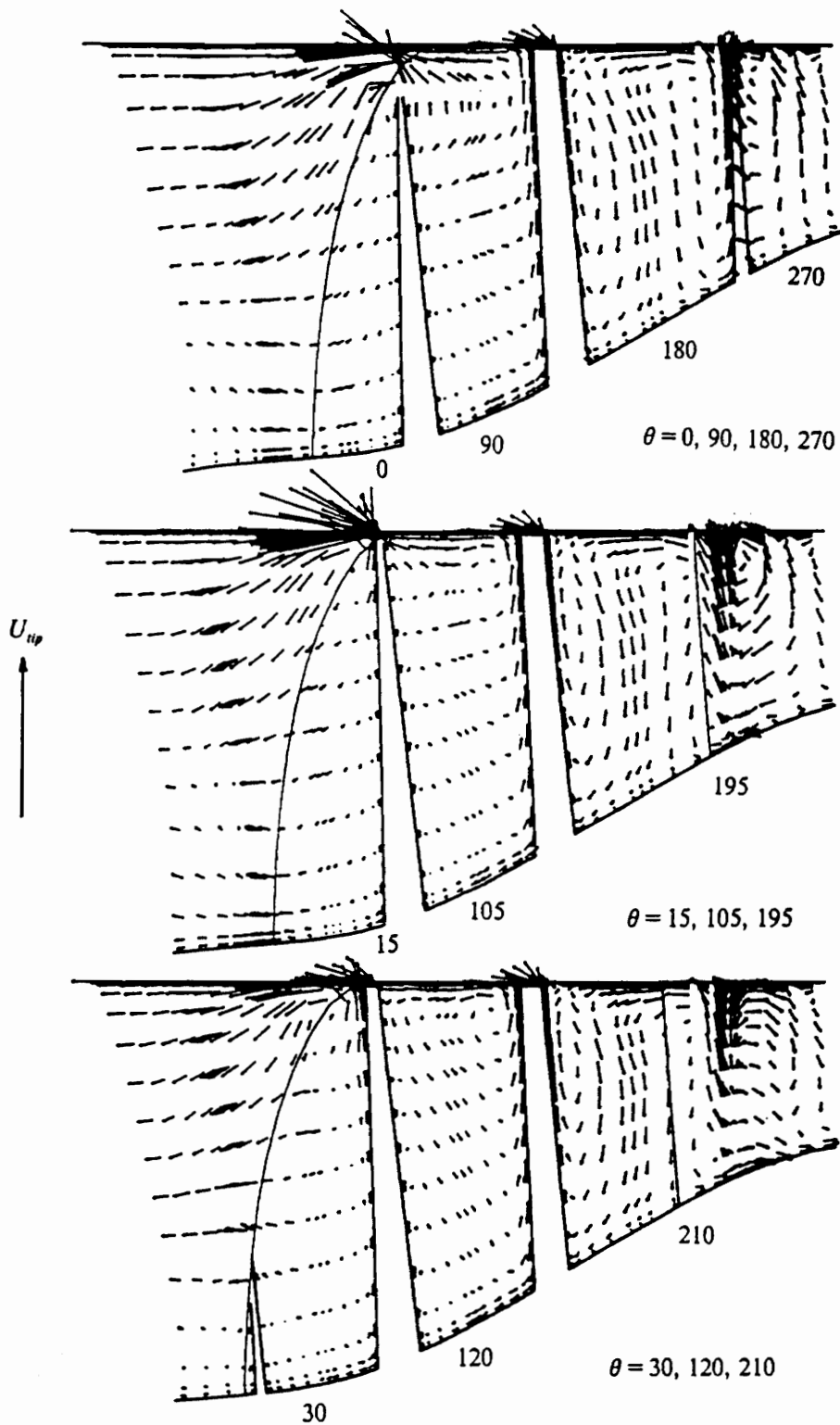


Figure 2.8 Secondary velocities in 3 iso-theta planes SEP inducer (reference 8)

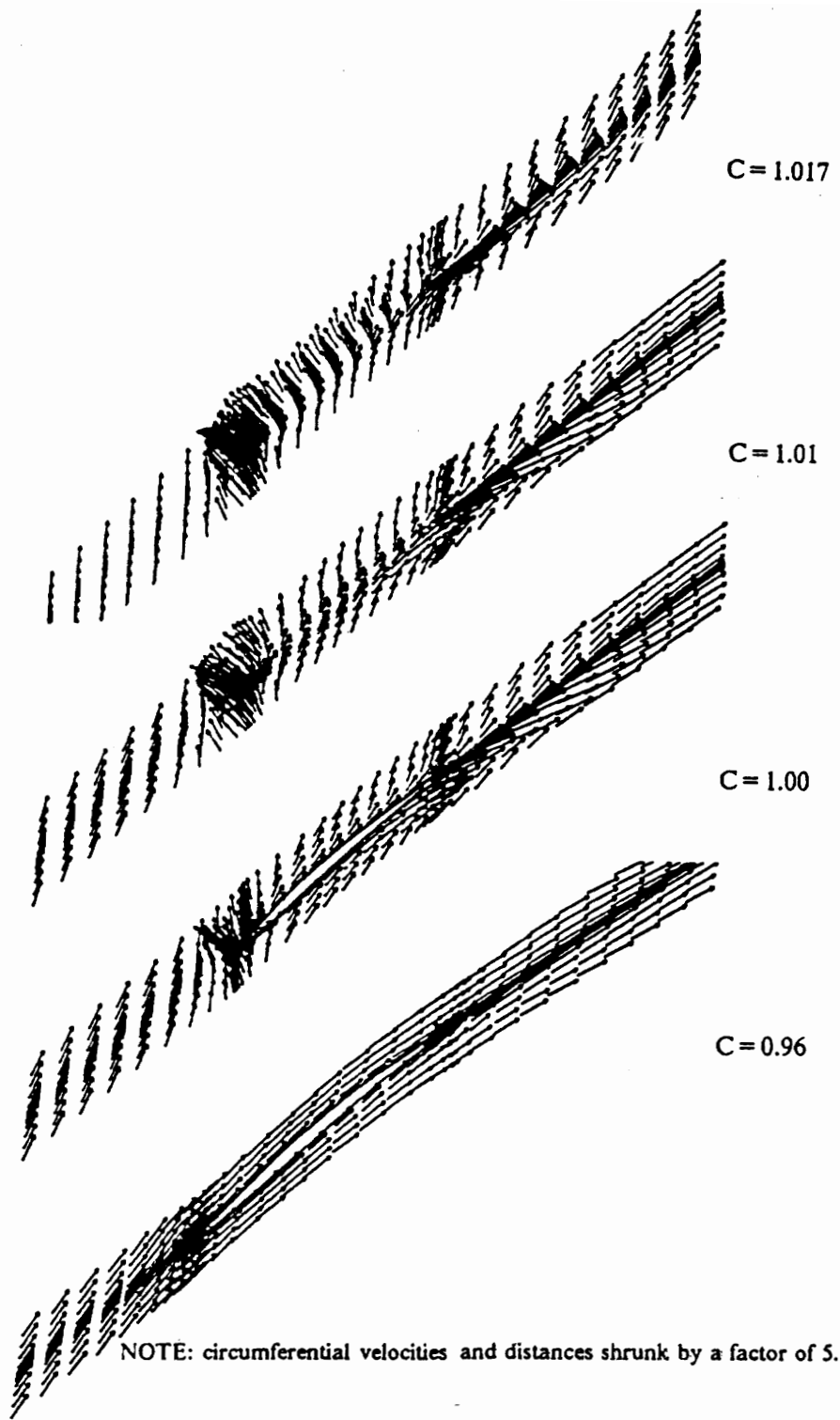


Figure 2.9 Tip leakage velocity vectors , SEP inducer (reference 8)

Later, from the same results Moore, Le Fur, and Moore (9) calculated the moment of momentum components, shown in Figure 2.10. This was done to quantify in detail the work contributions and losses within the inducer. The total moment of momentum was calculated by integrating rV_θ , ψ_E . The difference in pressure across the blade, ψ_{TP} , produced 60% of the moment of momentum. Shear at the shroud, ψ_{TSs} , dissipated moment of momentum. The shear on the blades, ψ_{TSr} , produced the remaining 40% of the moment of momentum, and was found by difference. These work coefficients, ψ , are defined and discussed in Section 8.4. Note that the Rocketdyne inducer is analyzed in a similar fashion in this research.

The inducer efficiency was calculated as follows.

$$\eta = \frac{\text{total pressure rise}}{\text{work}} \quad (1)$$

The contributions to total pressure rise were also calculated to determine their relative importance, shown in Figure 2.11. The centrifugal effect, $U_2^2 - U_1^2$, is the largest contribution to the pressure. The blockage formed by the leading edge vortex enhances the centrifugal effect by reducing the effective mean radius at the inlet.

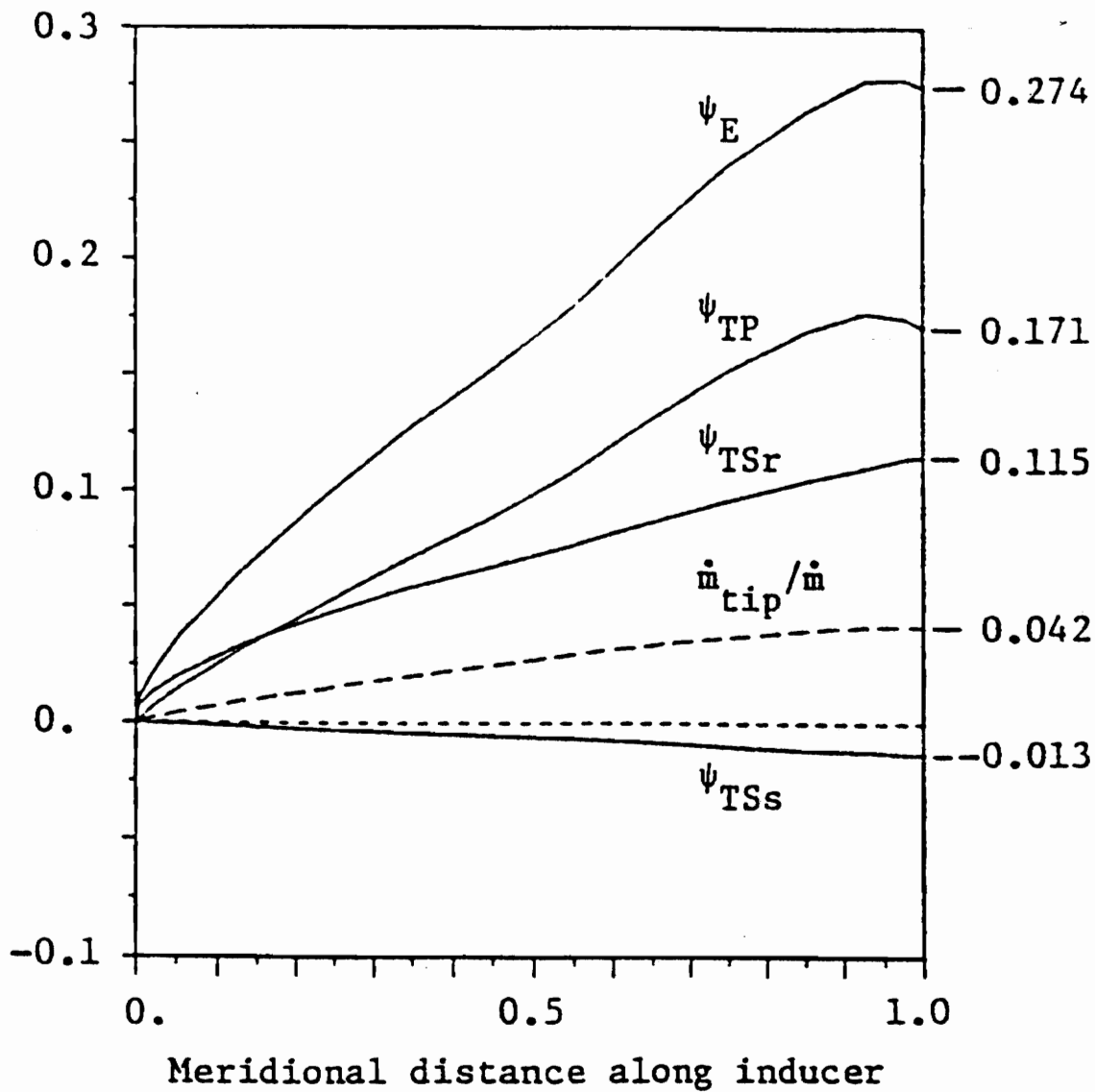


Figure 2.10 Contributions to work input through the SEP inducer (reference 9)

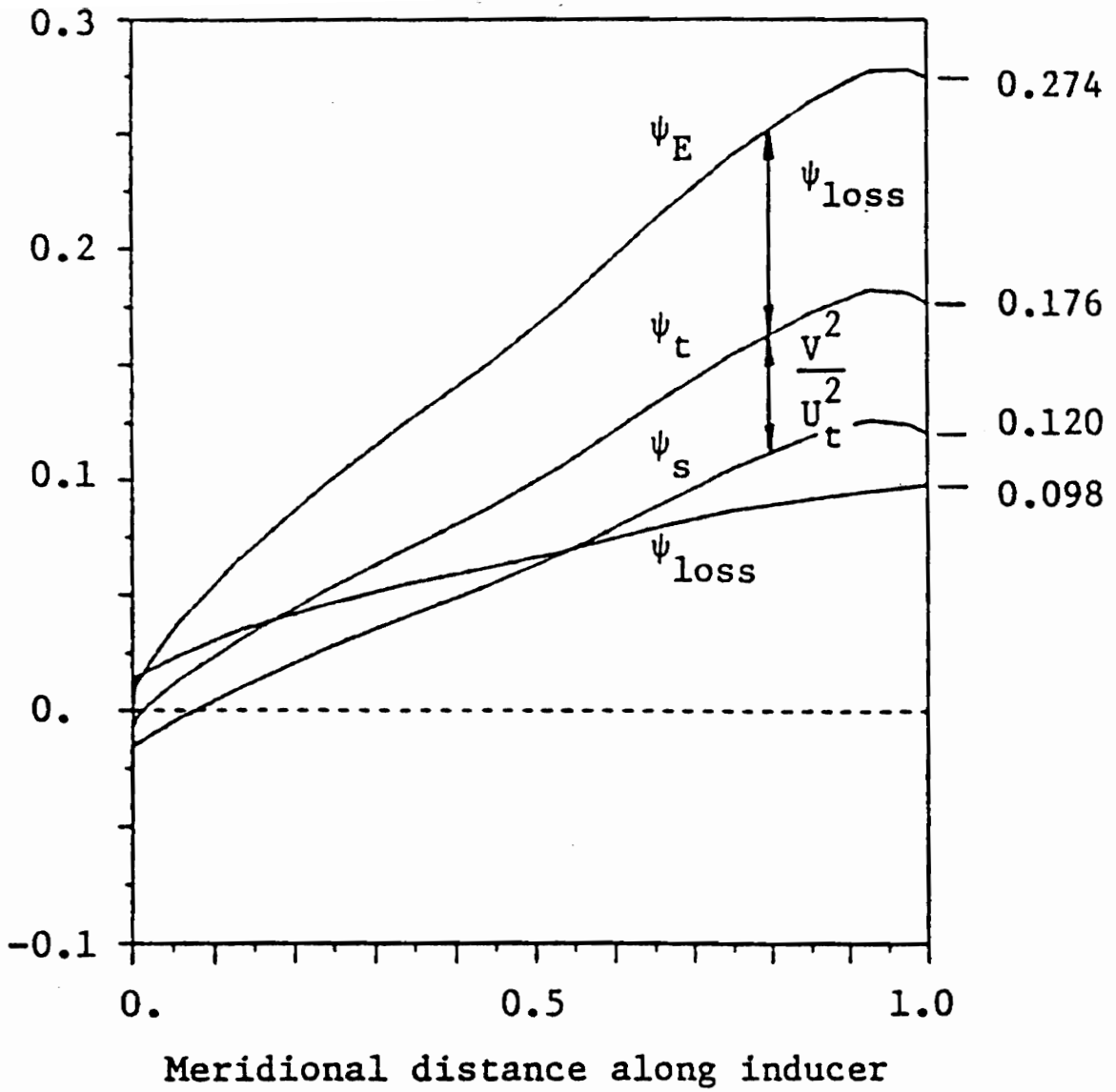


Figure 2.11 **Development of performance parameters through the SEP inducer, (reference 9)**

2.3 The Moore Elliptic Flow Program (MEFP)

The Moore Elliptic Flow Program is written for steady incompressible or compressible turbulent flow in turbomachinery. MEFP has been used to study steady 3-D flow in axial and centrifugal pumps. For example T. Le Fur (8), J. Moore, T. Le Fur, J.G. Moore (9), and T. Excoffon (10) studied a SEP inducer using MEFP. Also J. Moore, J.G. Moore, A. Lupi (11) studied blade lean in impellers, and later A. Lupi (12), contributed to the redesign of the NASA Marshall Pump Consortium impeller using MEFP.

The flow is described by the following steady flow conservation equations in the rotating reference frame:

Mass:

$$\nabla \cdot \rho \mathbf{W} = 0 \quad (2)$$

Momentum:

$$\rho \mathbf{W} \cdot \nabla \mathbf{W} - (\nabla \cdot \mu \nabla) \mathbf{W} = \nabla \cdot \mu \overline{\nabla \mathbf{W}^T} - \nabla p - 2\rho \boldsymbol{\Omega} \times \mathbf{W} - \rho \boldsymbol{\Omega} \times (\boldsymbol{\Omega} \times \mathbf{r}) \quad (3)$$

Equation of state:

$$p = \rho RT \quad (4)$$

Rothalpy(energy):

$$\rho \mathbf{W} \cdot \nabla H - (\nabla \cdot \mu \nabla) H = 0 \quad (5)$$

Second law of thermodynamics:

$$s - s_0 = c_p \ln\left(\frac{T}{T_0}\right) - R \ln\left(\frac{p}{p_0}\right) \quad (6)$$

The momentum equation is used for the three components of the relative velocity vector, \mathbf{W} . The energy equation is used to find rothalpy, H . For compressible flows, the temperature, T , is obtained using the definition of rothalpy, and the entropy, s , is found using the second law equation. The Moore viscous 3-D flow program uses a

pressure-correction calculation procedure, and thus, the continuity equation is used to solve for the pressure, p , while the equation of state gives the density, ρ . In time-marching methods, the unsteady continuity equation gives the density and the equation of state the pressure.

In the present study the fluid is water and the flow can be assumed incompressible. For incompressible flow only the mass and momentum equations are used, and the state equation is replaced by: $\rho = \text{constant}$.

For the turbulent flow calculation performed, the flow equations are coupled with a Prandtl mixing length model of turbulent viscosity, with a Van Driest correction, as follows:

$$\mu = \mu_{laminar} + \mu_{turbulent} \quad (7)$$

$$\mu_{turbulent} = \rho L^2 \frac{du}{dy} \quad (8)$$

where L is the smaller of:

0.08 times the width of the shear or boundary layer,

0.41 times the distance to the nearest wall.

In the 0.41 y region the Van Driest correction is used:

$$L = 0.41y(1 - \exp[-y \frac{\sqrt{\rho\tau}}{26\mu_{laminar}}]) \quad (9)$$

Between the wall and the near-wall grid points a near-wall correction is used:

$$\mu = \sqrt{\mu_{laminar}} \cdot \sqrt{\mu_{laminar} + \mu_{turbulent}} \quad (10)$$

For 3-D flow y is the distance to the nearest wall and du/dy is the square root of the velocity deformation.

The Moore Elliptic Flow Program is described in greater detail in the MEFP users guide (13). The discretization of the equations and the details of the pressure-correction method for an elliptic flow calculation are discussed in reference 14.

2.4 Definitions of pressures and kinetic energies

The pressure levels are determined by a reference pressure, which is set to zero. The maximum total pressure at the pump inlet is chosen as the reference pressure.

$$P_o = P_{t,max,inlet} = 0 \quad (11)$$

The total pressure, P_t , reduced pressure, P_r , and rotary stagnation pressure, P^* , are defined as follows.

$$P_t = P + \frac{1}{2}\rho V^2 \quad (12)$$

$$P_r = P - \frac{1}{2}\rho \omega^2 r^2 \quad (13)$$

$$P^* = P + \frac{1}{2}\rho W^2 - \frac{1}{2}\rho \omega^2 r^2 \quad (14)$$

Where $V^2/2$ is the absolute kinetic energy, $\omega^2 r^2/2 = U^2/2$ is the blade kinetic energy, and $W^2/2$ is the relative kinetic energy. These calculated pressures are often normalized with $1/2\rho U_{tip}^2$. The kinetic energies, U^2 , W^2 , and V^2 , are commonly normalized with U_{tip}^2 . Rotary stagnation pressure, P^* , is conserved in steady inviscid incompressible flow in a rotor. Rotary stagnation pressure and its significance is explained in more detail in Appendix B. A loss coefficient,

$$\frac{P_o - P^*}{\frac{1}{2}\rho U_{tip}^2} \quad (15)$$

is used to present computed loss contours in this thesis.

3 SCOPE AND OBJECTIVES OF THIS RESEARCH

Computational studies of inducers are rare. Axial flow inducers are more commonly studied experimentally, if at all. The experiments normally use pressure probes or hot wires for flow measurements and only cover the inlet and exit to rate the overall inducer performance. Highly detailed studies of the flow within the inducer passages have not been done until recently using 3-D laser anemometry.

Rocketdyne has work in cooperation with the NASA Marshall Pump Consortium to provide detailed experimental data for verifying 3-D flow codes as well as for studying the flow fields. The Rocketdyne inducer was tested in water using 3-D laser anemometry by L. Brozowski, L. Rojas, and T. Eastland (16,17,18). Detailed data was recorded for six axial measurement planes: at the inducer inlet, four planes within the inducer, and at the inducer exit.

The NASA Marshall Pump Consortium requested a computational analysis of the Rocketdyne inducer to demonstrate the capability of the Moore Elliptic Flow Program in a predictive mode. The research discussed in this thesis involved the computational analysis of the Rocketdyne inducer before the experimental results were available. The flow calculation used MEFP which is able to accurately represent the backflows and swirling flows found in an inducer. Since 3-D laser anemometry data was available for the Rocketdyne inducer, this study was a rare opportunity to compare the calculated flow field to the actual flow field measurements within the inducer. The results of the Rocketdyne 3-D laser anemometry studies were used to verify the calculated flow field at the design flow rate. Then the flow field was calculated for 89% and 110% flow rates to observe the changes in recirculation and work production as a function of flow rate.

This thesis will present the highlights of the calculations made with MEFP, the comparison of the computational results to the experimental results, an analysis of the recirculation in the inducer, and an analysis of the thermodynamic performance.

4 GEOMETRY AND GRID

The Rocketdyne inducer is used as the first stage in the Pump Consortium test rig for axial and centrifugal pump flow studies, shown in Figure 4.1. The Rocketdyne inducer geometry is shown in Figures 1.1 and 4.2. The annulus has a ramped hub and a cylindrical tip. The rotor has four unshrouded blades, and the stagger angle is very high due to the low flow coefficient. There is no spinner on the nose of the inducer, the flow stagnates on the nut on the end of the shaft.

The Pump Consortium test setup at Rocketdyne was previously used for impeller tests. Rocketdyne had provided 2-D laser velocimetry measurements at the impeller inlet plane, shown in Figure 4.3, for impeller flow calculations. Rocketdyne then made 3-D laser velocimetry measurements for the inducer flow calculations. The six measurement planes through the inducer are also shown in Figure 4.3.

4.1 Calculation Grid Generation

The inducer calculation grid was assembled in cylindrical (r, θ, z) coordinates with the z -axis as the axis of rotation. The dimensionless spatial parameters A , B , and C were used to create and manipulate the grid. The axial distance parameter, A , is defined as -1 at the inlet plane, 0 at the blade leading edge, 1 at the blade trailing edge, and 2 at the exit plane. The blade-to-blade distance parameter, B , is defined as 1 at the pressure surface and 0 at the suction surface. The hub-to-tip distance parameter, C , is defined as 0 at the hub, 1 at the tip, and -1 at the axis of rotation. At locations between these defined boundaries, the distance parameters are approximately proportional to the distance to the boundaries.

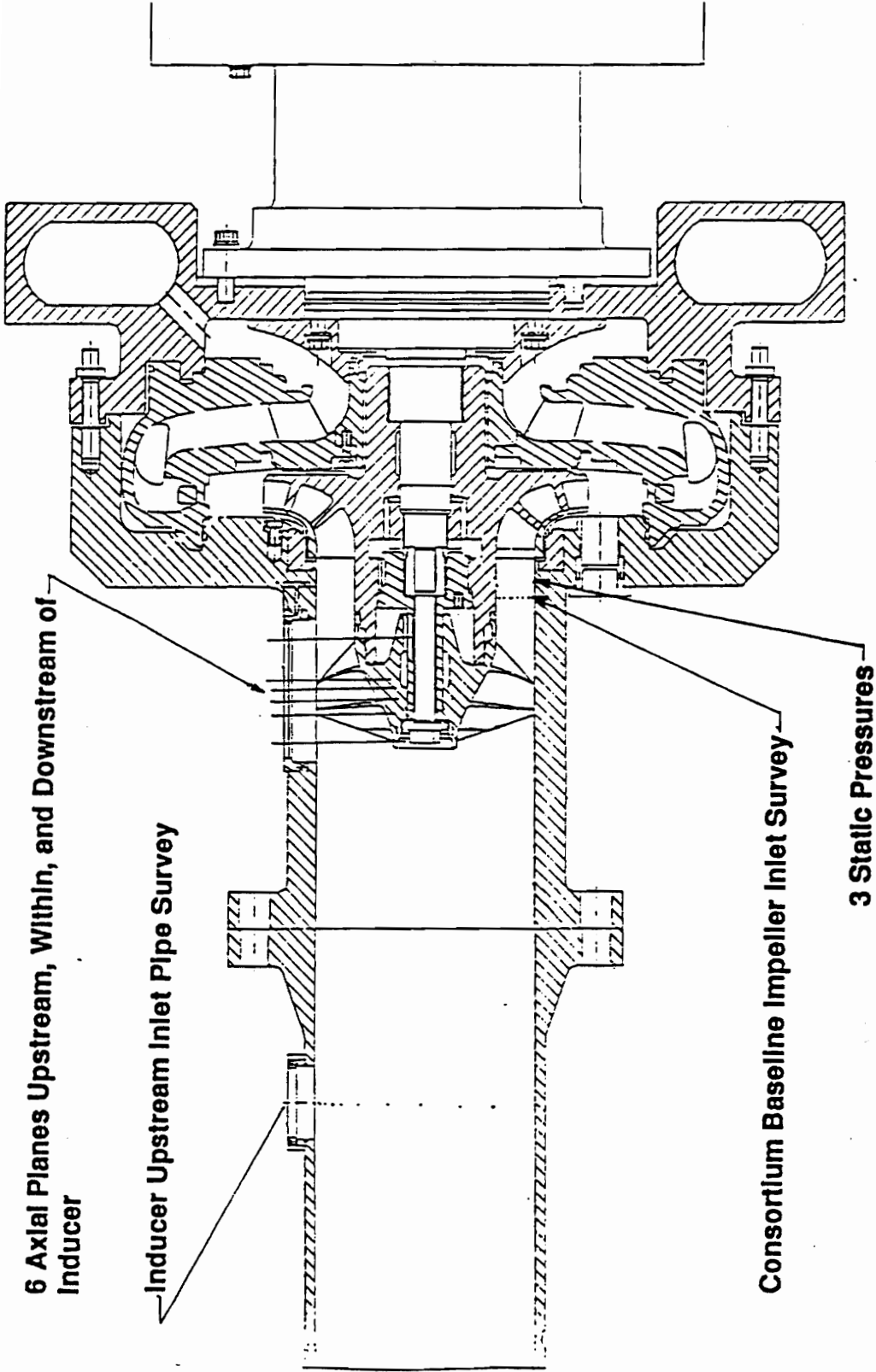


Figure 4.1 The Rocketdyne inducer test setup (reference 17)

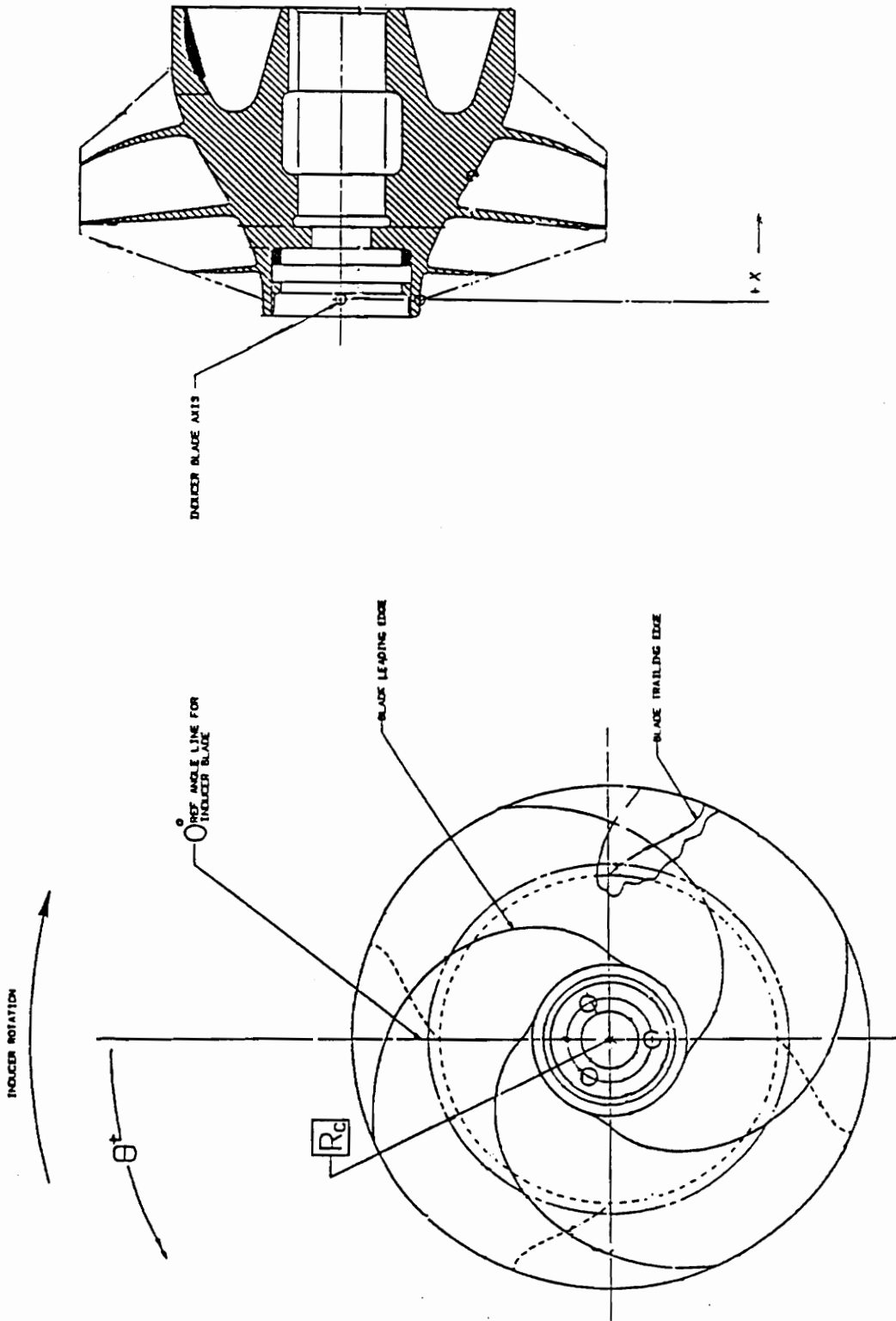


Figure 4.2 Rocketdyne inducer geometry (reference 17)

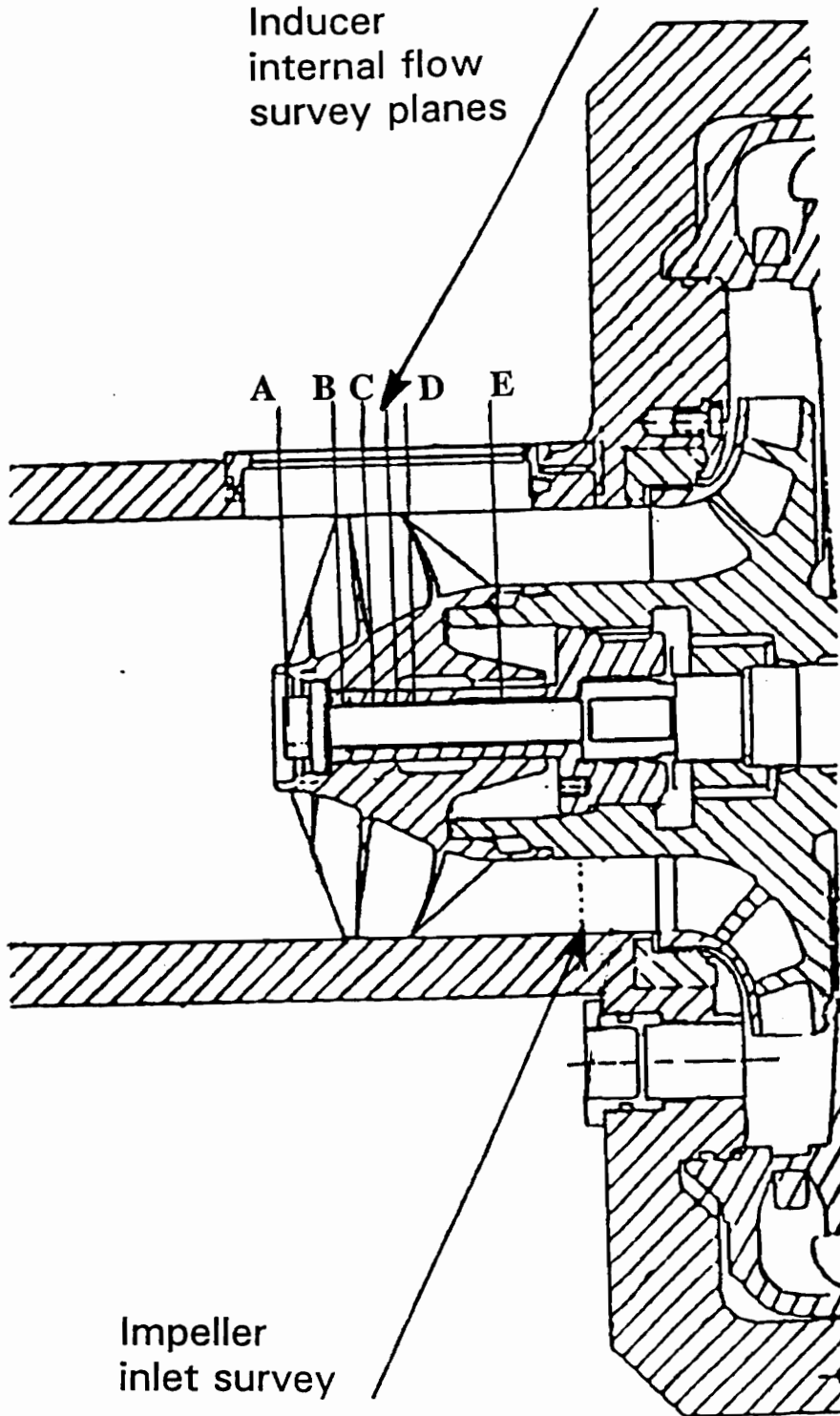
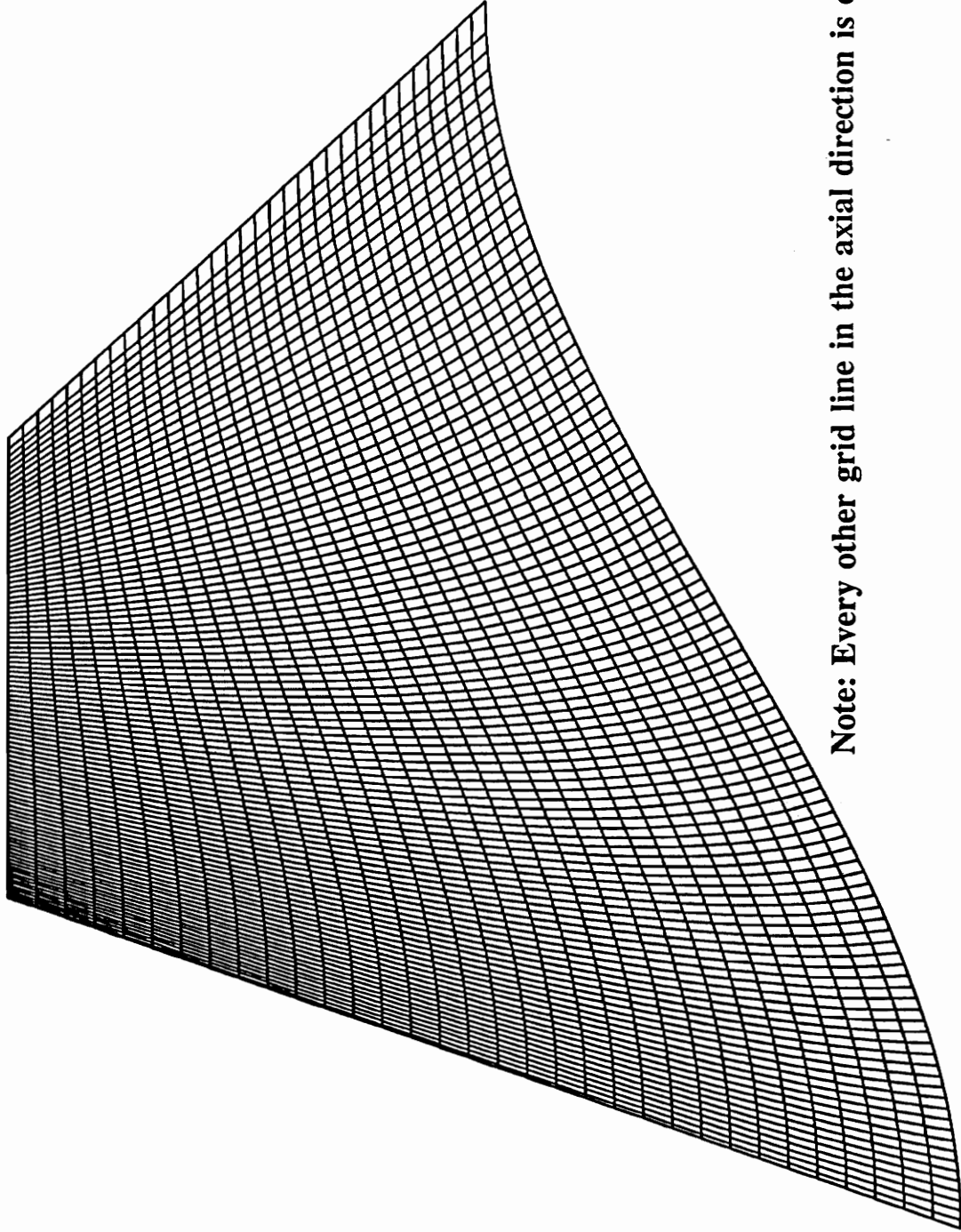


Figure 4.3 6 laser velocimetry measurement planes within the inducer, and one at the impeller inlet plane (reference 17)

The calculation grid was based on very dense blade geometry grids from Rocketdyne, Figure 4.4. Note that the blade is shown in a meridional view, meaning that only the axial and radial components of the blade geometry are shown. The tangential component is removed in a meridional view so that the blade no longer wraps around the hub, but is shown in a single plane. The final version of the calculation grid was produced in the following steps:

- 1 The grid was converted from x,y,z coordinates to r,θ,z coordinates, then the excess grid lines were removed to make it more manageable. This was done with a simple C program.
- 2 The suction side and pressure side grids were joined, and the leading and trailing edge shapes were approximated as shown in Figure 4.5.
- 3 The boundary lines for the upstream, downstream, spinner, casing walls, and tip-gap were added. Figure 4.6 shows a meridional view of the un-meshed calculation region. Steps 2 and 3 were combined in a C program.
- 4 The grid was meshed with optimized grid spacing. The areas of interest (leading and trailing edges, hub, tip, tip gap, and near the walls) had higher density grids. The grid was coarse at the middle of the flow where only a sparse grid was necessary. Figure 4.7 shows a meridional view (r vs z view of the i - k grid lines) of the optimized grid. Optimization is a very important step since it is desirable to limit the number of grid points, yet a dense grid is required to model boundary layer effects. The actual grid spacing used is detailed in the figures and discussions that follow.
- 5 The grid was smoothed to make the changes in grid spacing more gradual throughout the flow field and make the grid elements as close to square as possible. The calculation grid was meshed, optimized, and smoothed using GOPTW, a grid optimization program written by J. G. Moore for generating MEFP calculation grids. The rest of the figures in this section show the final smoothed calculation grid.



Note: Every other grid line in the axial direction is omitted

Figure 4.4 Very dense blade geometry grid from Rocketdyne



Leading Edge



Trailing Edge

Leading and trailing edge shapes

Figure 4.5

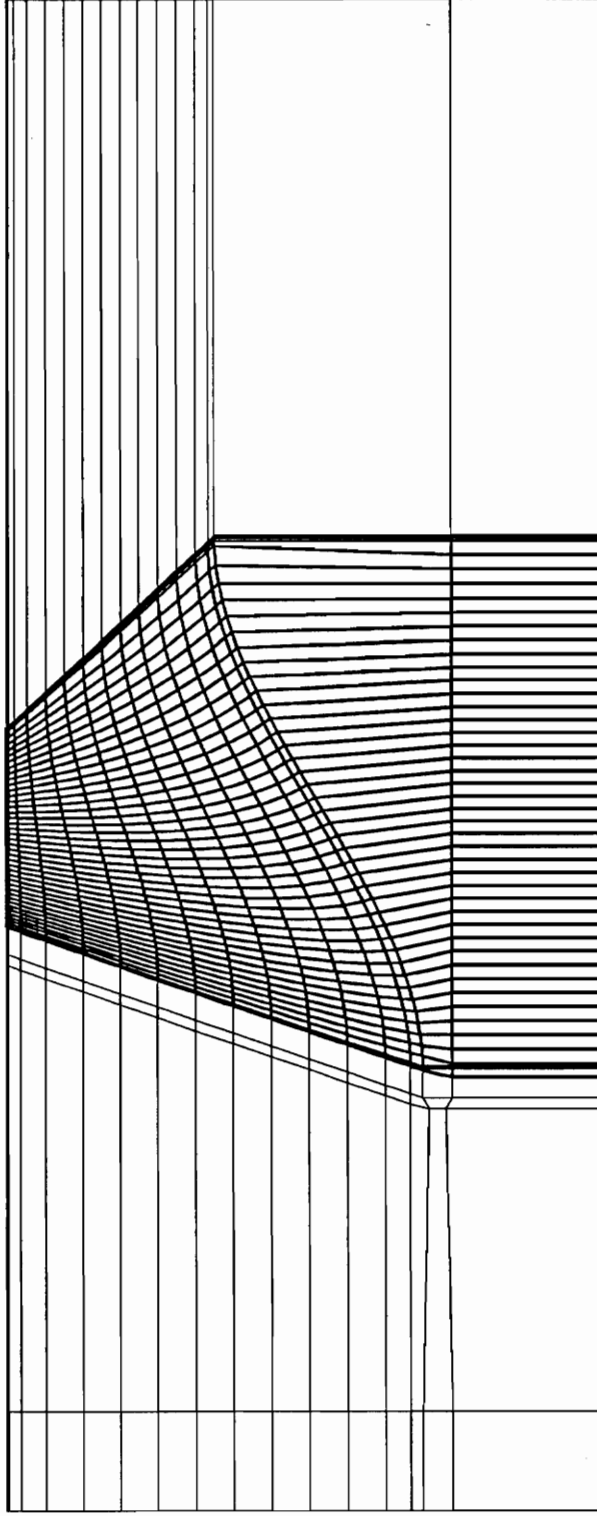


Figure 4.6 Meridional view (r vs z) of the un-meshed calculation region

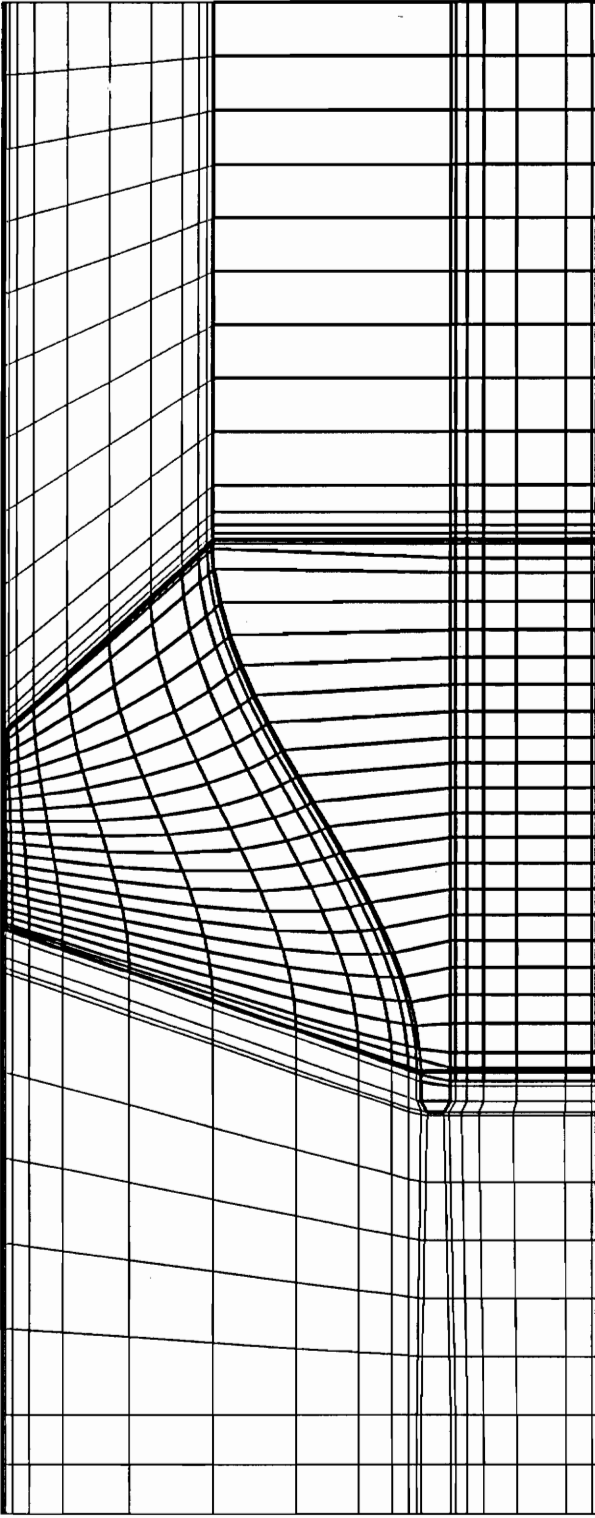


Figure 4.7 Meridional view (r vs z) of the optimized grid

A = -1.
inlet

A = 0.
L.E.

A = 1.
T.E.

A = 2
exit

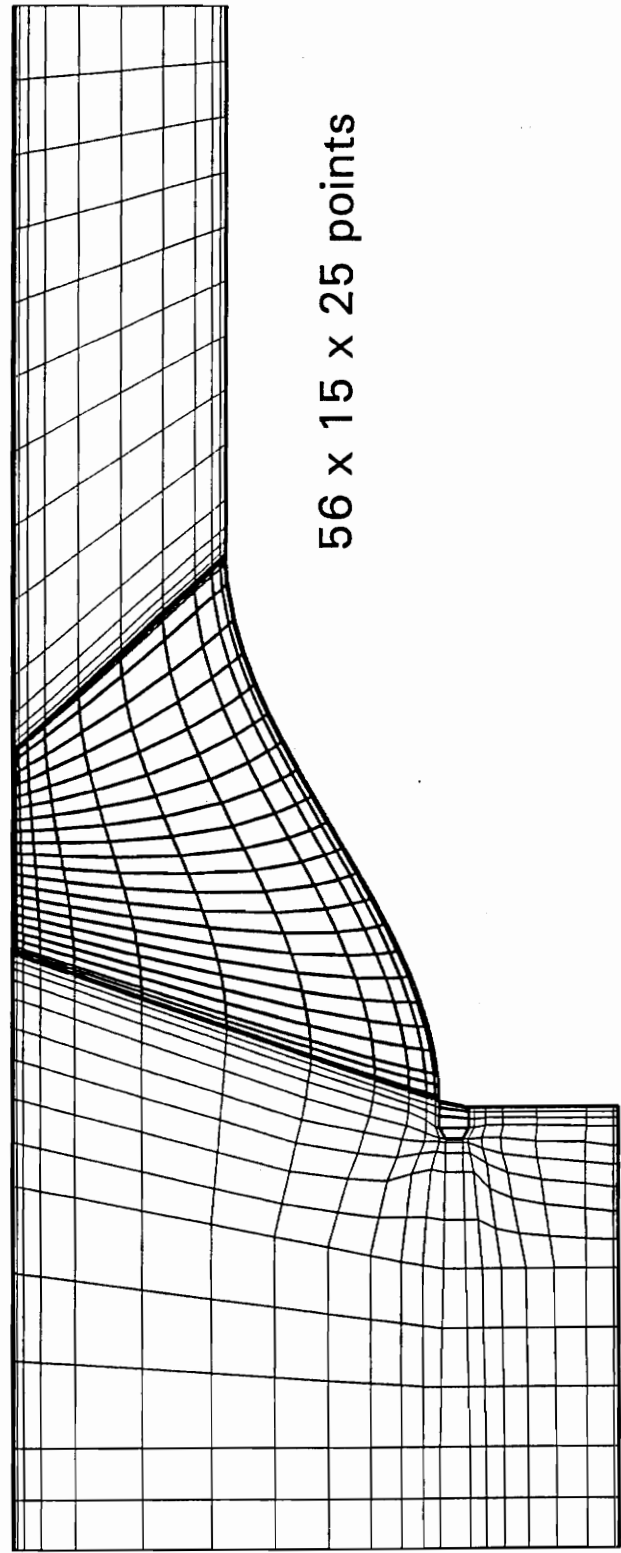


Figure 4.8 Meridional view (r vs z) of the final design flow rate calculation grid

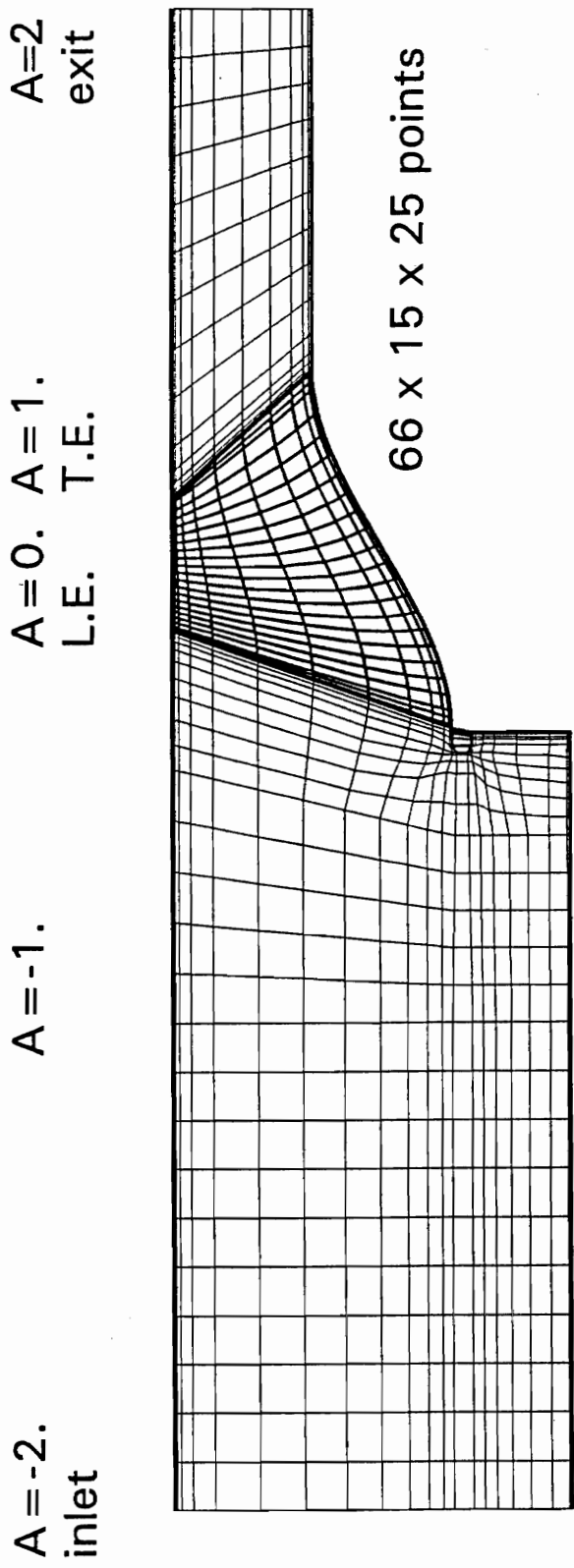
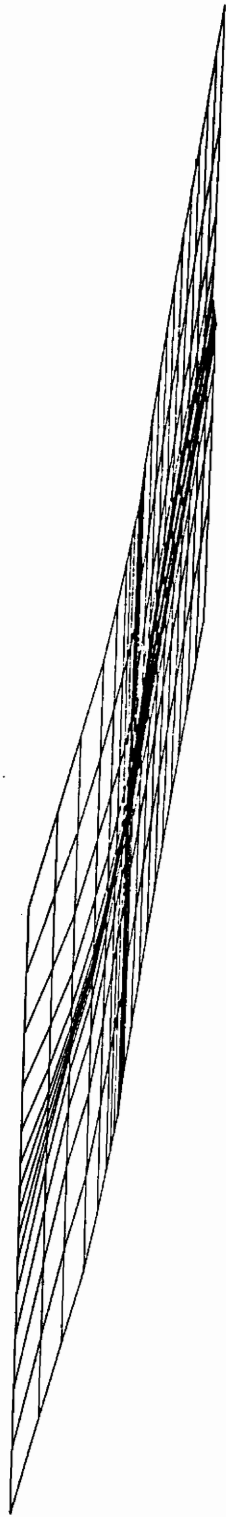
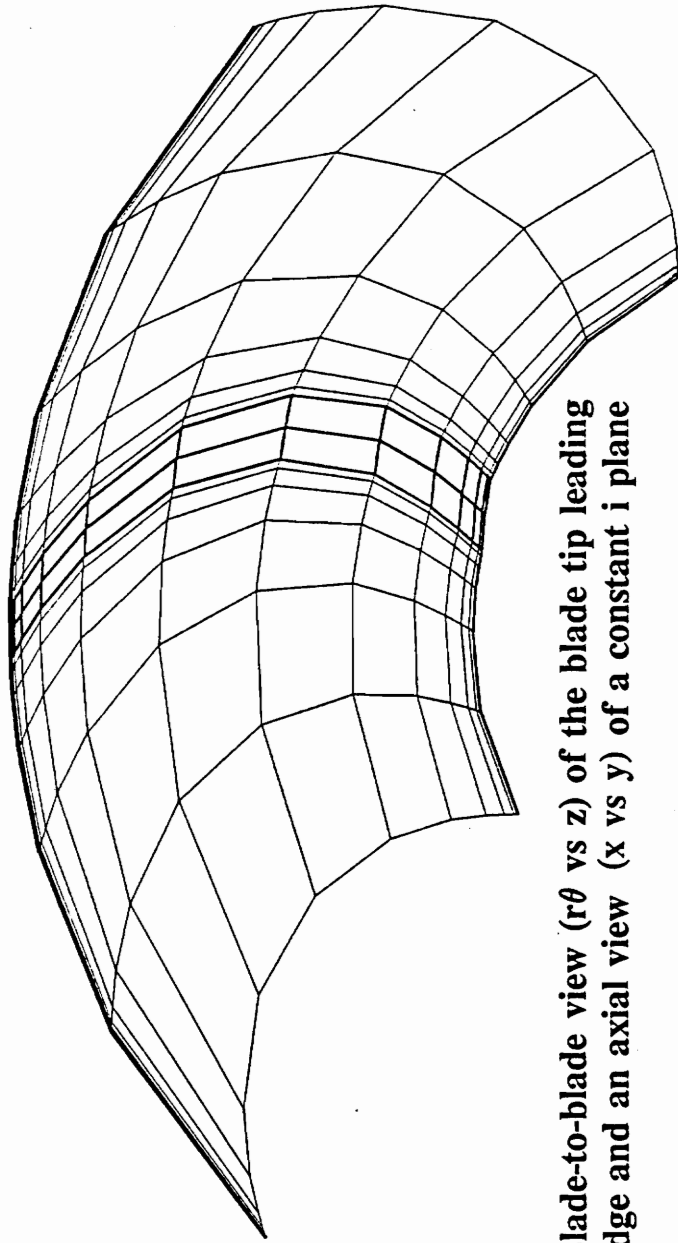


Figure 4.9 Meridional view of the calculation grid for the 89% flow rate

Blade-to-blade grid near L.E. at tip



Axial view of i-plane mid-way thru inducer



Blade-to-blade view ($r\theta$ vs z) of the blade tip leading edge and an axial view (x vs y) of a constant i plane

Figure 4.10

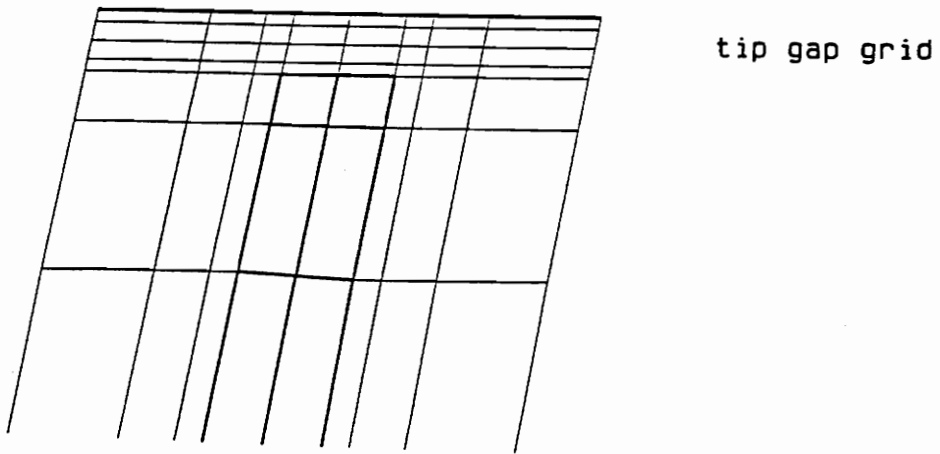
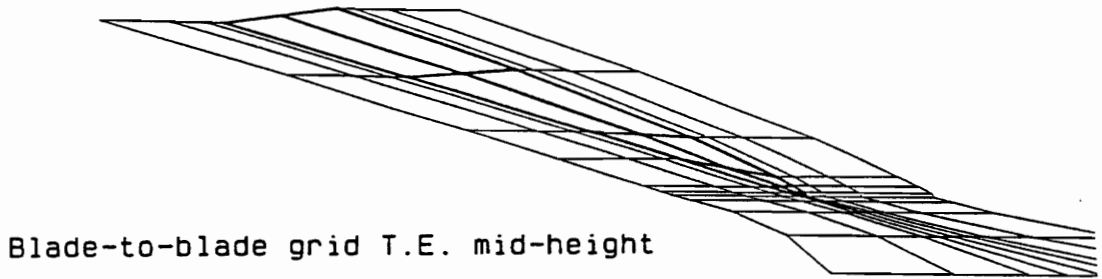
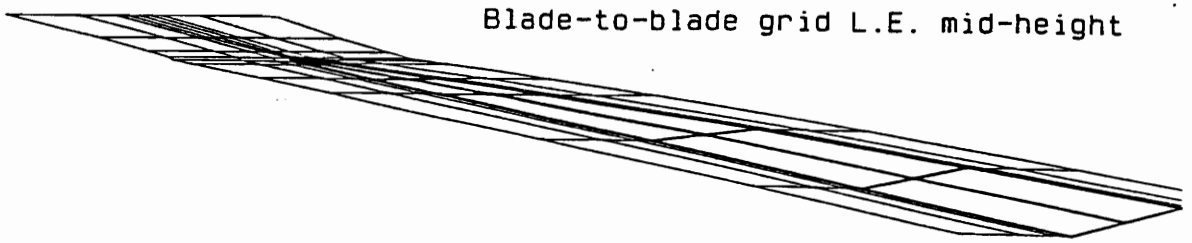


Figure 4.11 Blade shape at the leading and trailing edge, and the tip gap

4.3 Calculation Details

Inducer geometry, flow condition, and performance parameters are provided in Table 4.1. The shroud, from inlet to exit, is a stationary wall, with zero absolute velocity. The inducer blades and the hub, extending from the nut to the exit, are rotating walls, with zero relative velocity. The axial grid line near the centerline upstream of the nut is specified slightly off the axis of rotation, and is modelled as an inviscid wall. The inlet plane velocity profile, shown in Figure 4.12, was obtained from the Rocketdyne water tests carefully documented in reference 16. The pressure is uniform on the inlet plane.

Table 4.1 Table of inducer information

tip radius	r_{tip}	0.0762 m	(3.00 in)
tip gap		0.254 mm	(0.01 in)
target design flow rate	\dot{m}	1210	gpm
design flow rate	\dot{m}	18.145	(kg/s)/blade
density (water)	ρ	1000	kg/m ³
laminar viscosity	μ_{lam}	.001	kg/(m s)
shaft speed	N	6322	rpm
angular velocity	ω	662.04	rad/s
blade tip speed	U_{tip}	50.447	m/s
Reynolds Number	Re_D	7.69×10^6	$\rho U_{tip} d / \mu$
flow coefficient	$\phi = V_x / U_{tip}$		
design		.091	
89%		.081	
110%		.100	

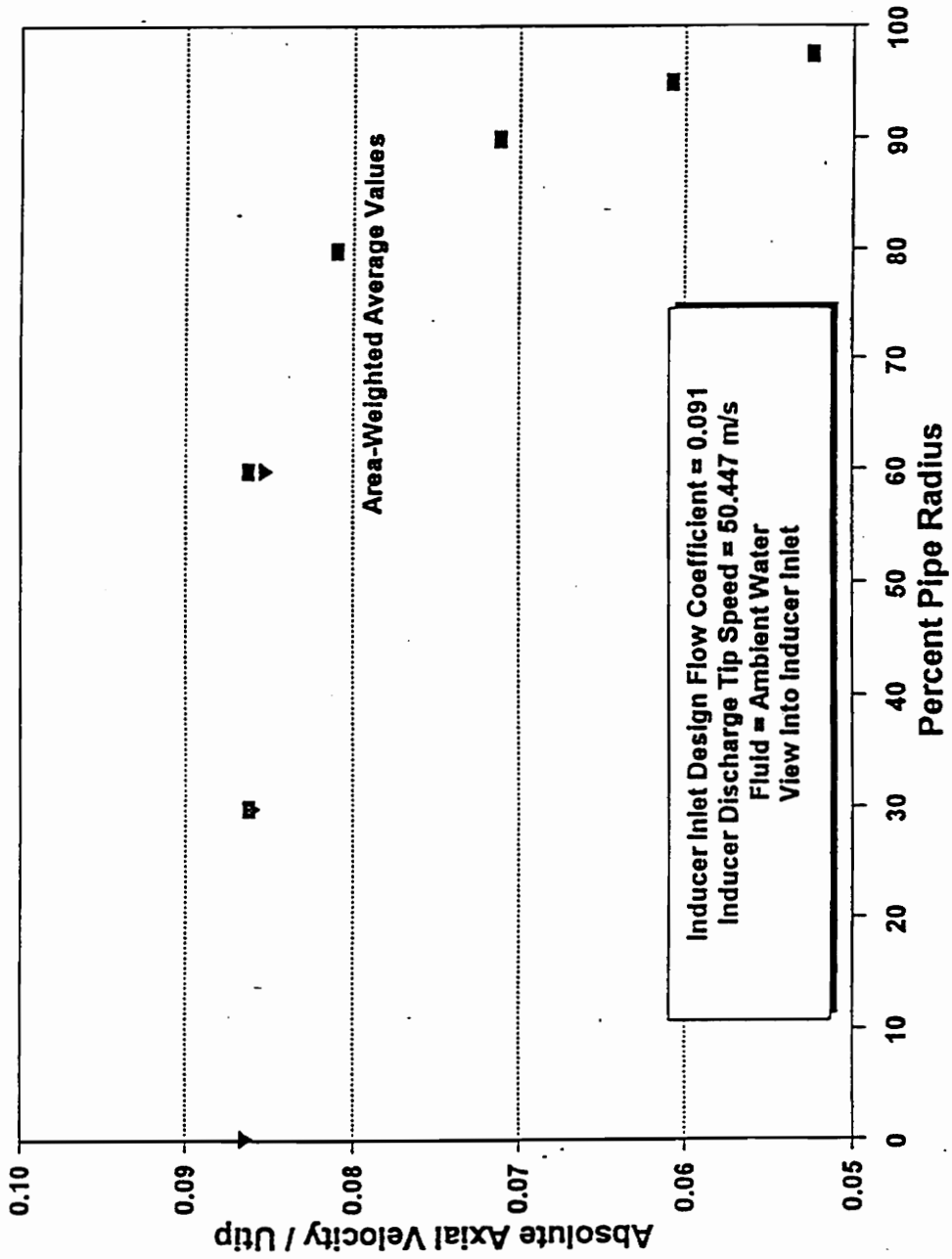


Figure 4.12 Inlet plane velocity values (reference 16)

5 CALCULATION RESULTS

The calculations were carried out on an HP 720 workstation. Each run required 100 iterations and took about 24 hours. At the completion of the calculations, several views had to be created to visualize the flow field. Figures 5.1 through 5.7 illustrate the general flow patterns within the inducer at the design flow rate.

Meridional views of calculated velocity vectors, Figures 5.1, 5.2, and 5.3, show the inlet and exit boundary layer profiles. Notice the non-uniform exit velocity profile. The velocity vectors shown are the vectors projected in the view; the tangential components are much larger except for in the tip region. The blade tip speed vector, U_{tip} , is shown on each plot for comparison. The flow entering the tip gap is shown on the pressure side by velocity vectors that are about 0.6 of the tip speed. Here the flow is turned from the tangential direction as it enters the tip gap such that there is a large component in the r-z plane. Figures 5.1 and 5.2 show there is a radially outward component of velocity near the blades. This is associated with secondary flows caused by the nonuniform velocity profile in the blade boundary layer. There is also a centrifuging effect near the blade surface that drives the radially outward flow. Similarly, Figure 5.3 shows a radially inward velocity component at mid-passage. These secondary flows are consistent with the inducer internal flow patterns presented by Lakshminarayana as shown in Figure 2.1. These figures also show backflow at the tip leading edge.

Contours of rotary stagnation pressure loss coefficient (Eq. 16, Section 2.4), for the design flow rate are shown in Figure 5.4. To obtain this figure, the calculation results were interpolated to 6 tangential locations. Each plot cuts through 2 or 3 blades. The meridional location of the blade leading and trailing edges has been superimposed on each plot as was shown in Figure 4.2. The results show losses produced near the blade surface, which are centrifuged out toward the shroud by the secondary flow in the blade boundary layers as seen in Figures 5.1 and 5.2. The losses accumulate at the shroud, and are then convected downstream along the shroud. The figures also show that

some of the losses are carried upstream by the tip leakage flow, and into the recirculation region at the inlet.

Figures 5.5, 5.6, and 5.7 are meridional views at near pressure side, near suction side, and mid-passage respectively, showing the velocity vectors and the rotary stagnation pressure together. The losses in the inlet boundary layer are negligible compared to the losses produced in the inducer.

All the figures show the recirculation region, which is marked by the area of swirling velocity vectors at the tip leading edge. A cell of low rotary stagnation pressure can also be seen centered on the recirculation region. Also note that the flow does not separate over the nut at the nose. Therefore, a spinner is not really needed since the flow over the nose is already clean.

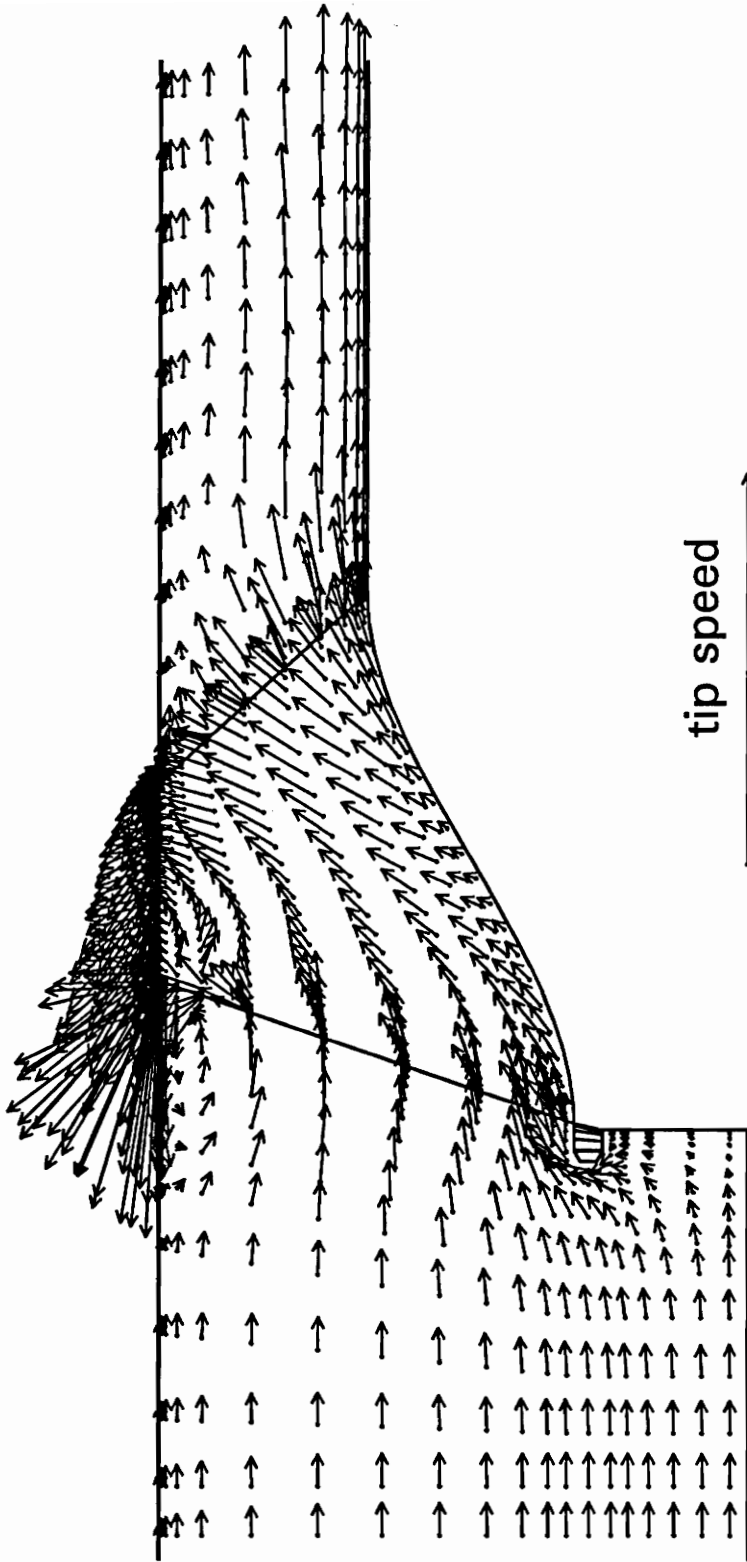


Figure 5.1 Meridional view near pressure surface of calculated velocity vectors at design flow rate.

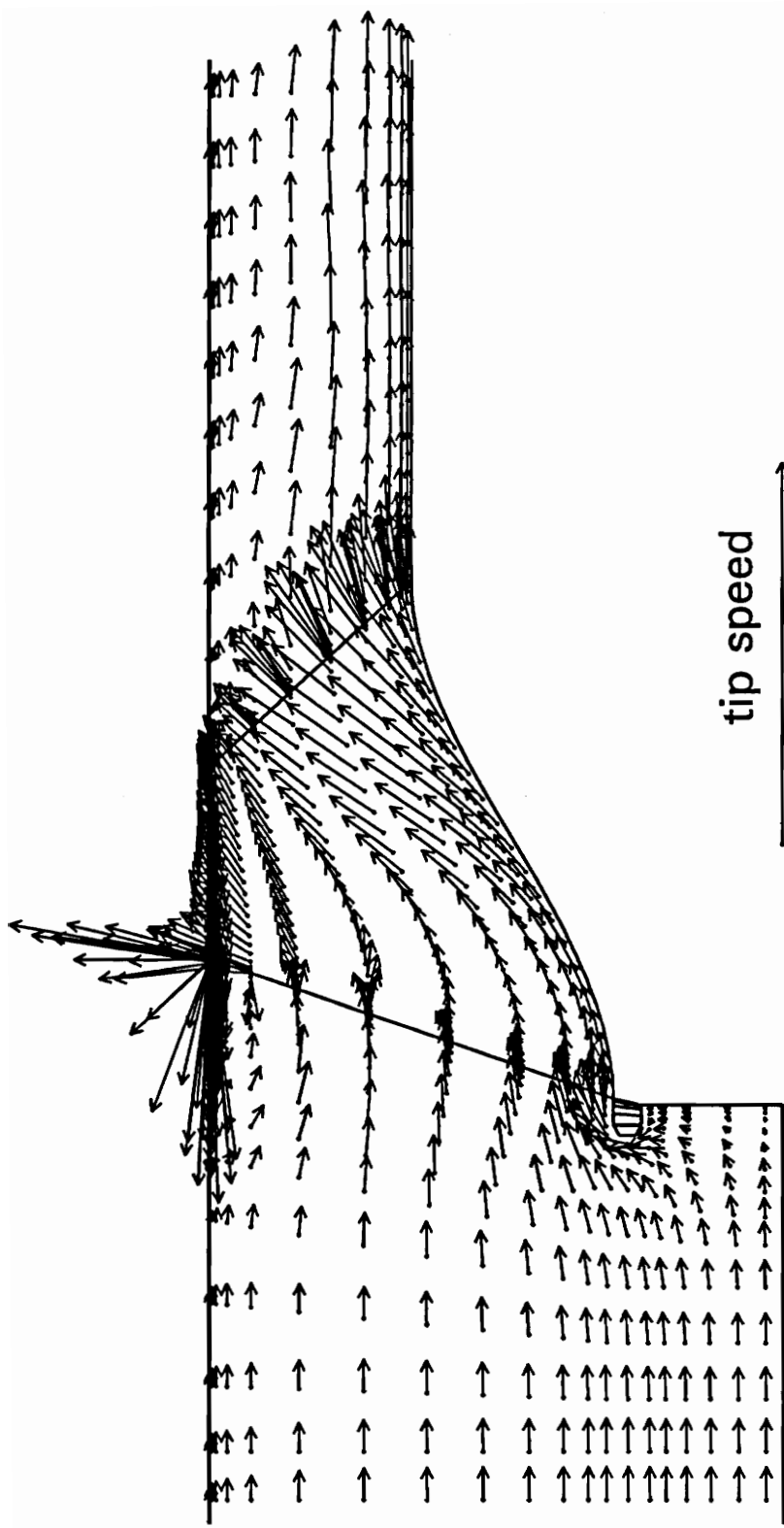


Figure 5.2 Meridional view near suction surface of calculated velocity vectors at design flow rate.

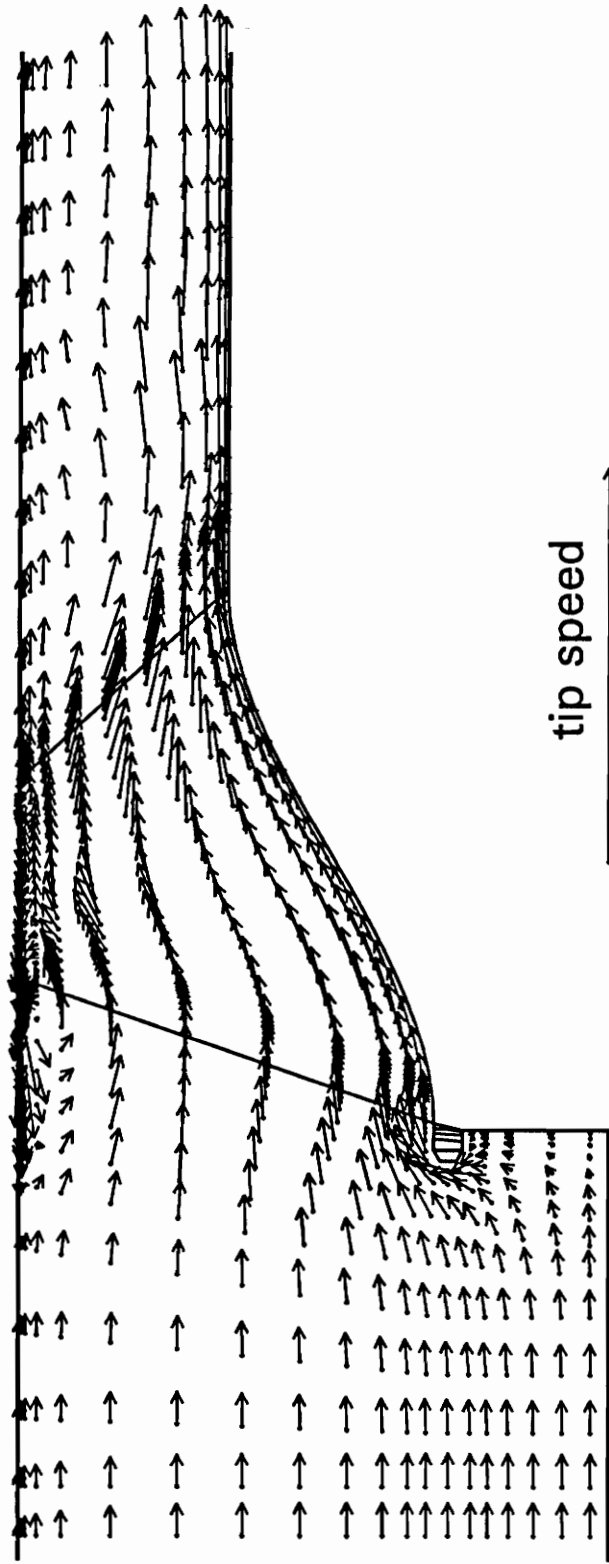
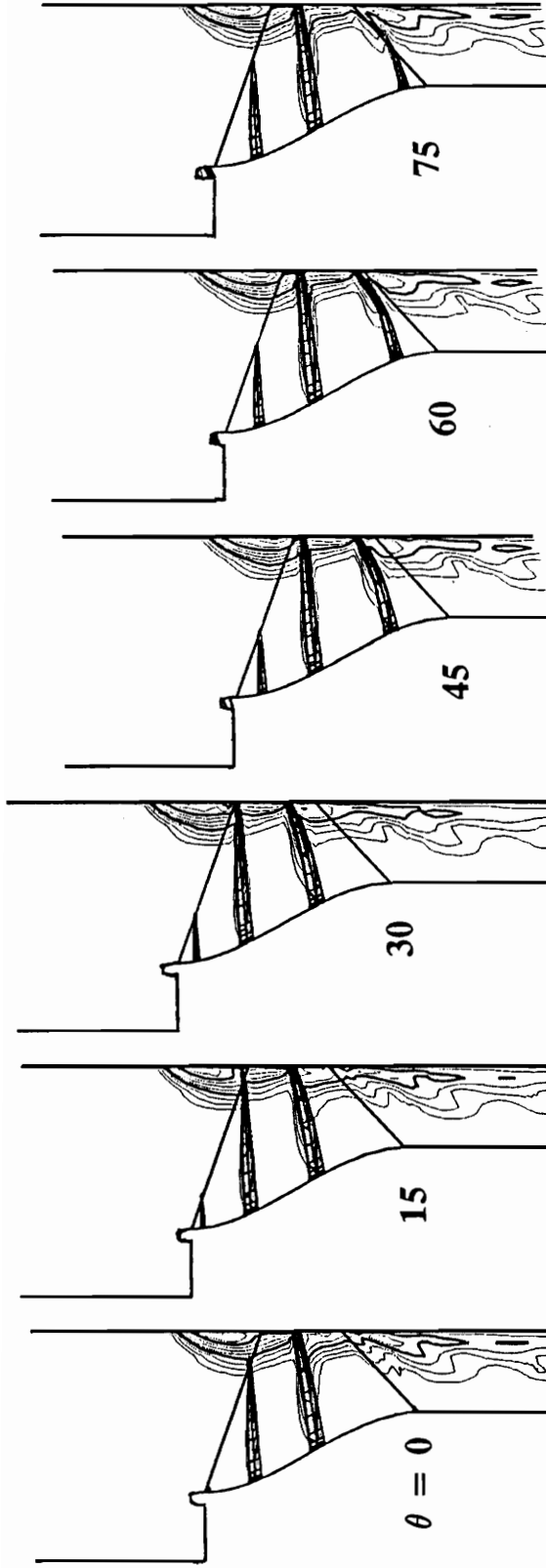


Figure 5.3 Meridional view at mid-passage of calculated velocity vectors at design flow rate.



Contours of P^* loss coefficient from .05 to .8 by .05

Figure 5.4 Meridional slices showing P^* at design flow rate

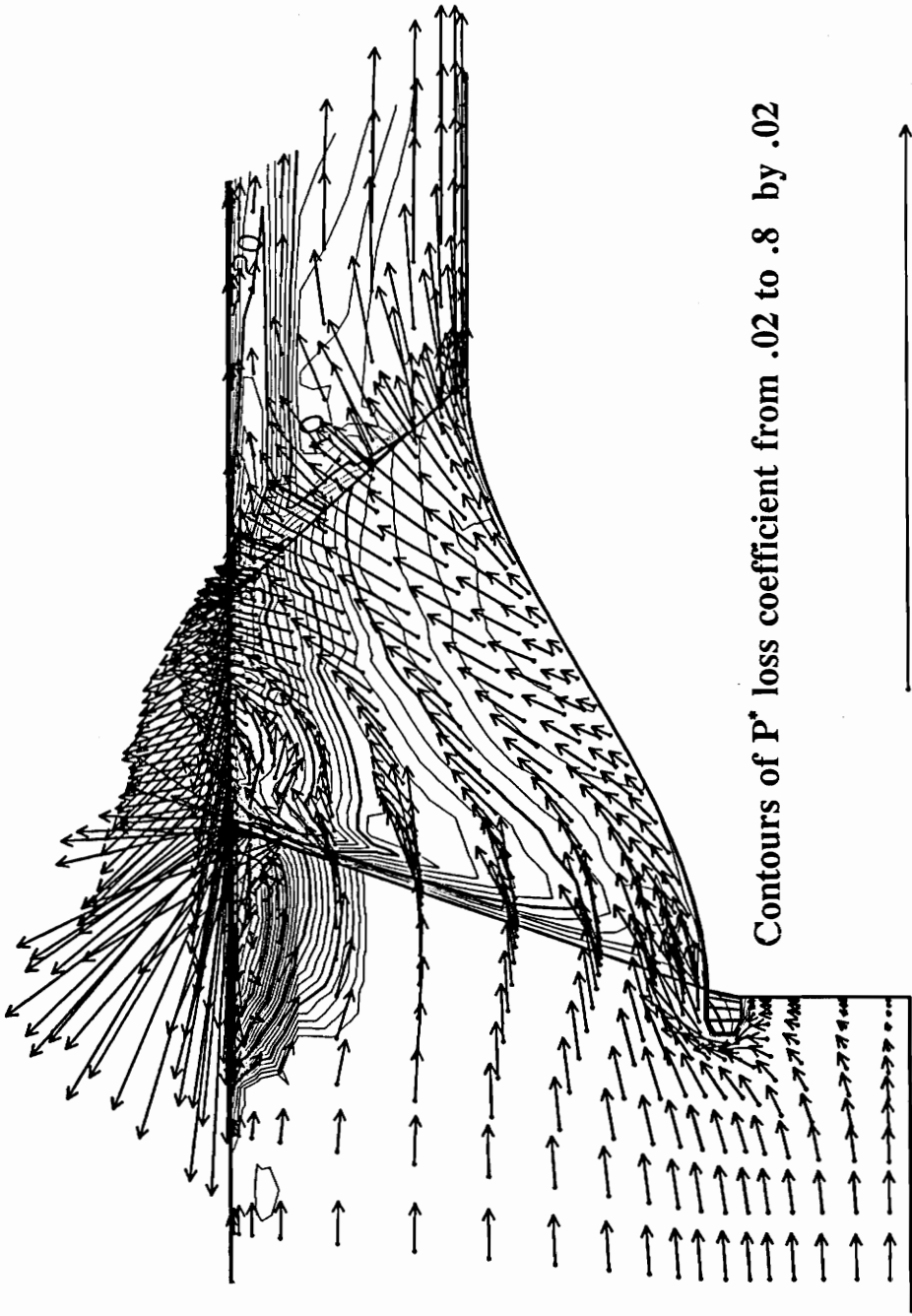
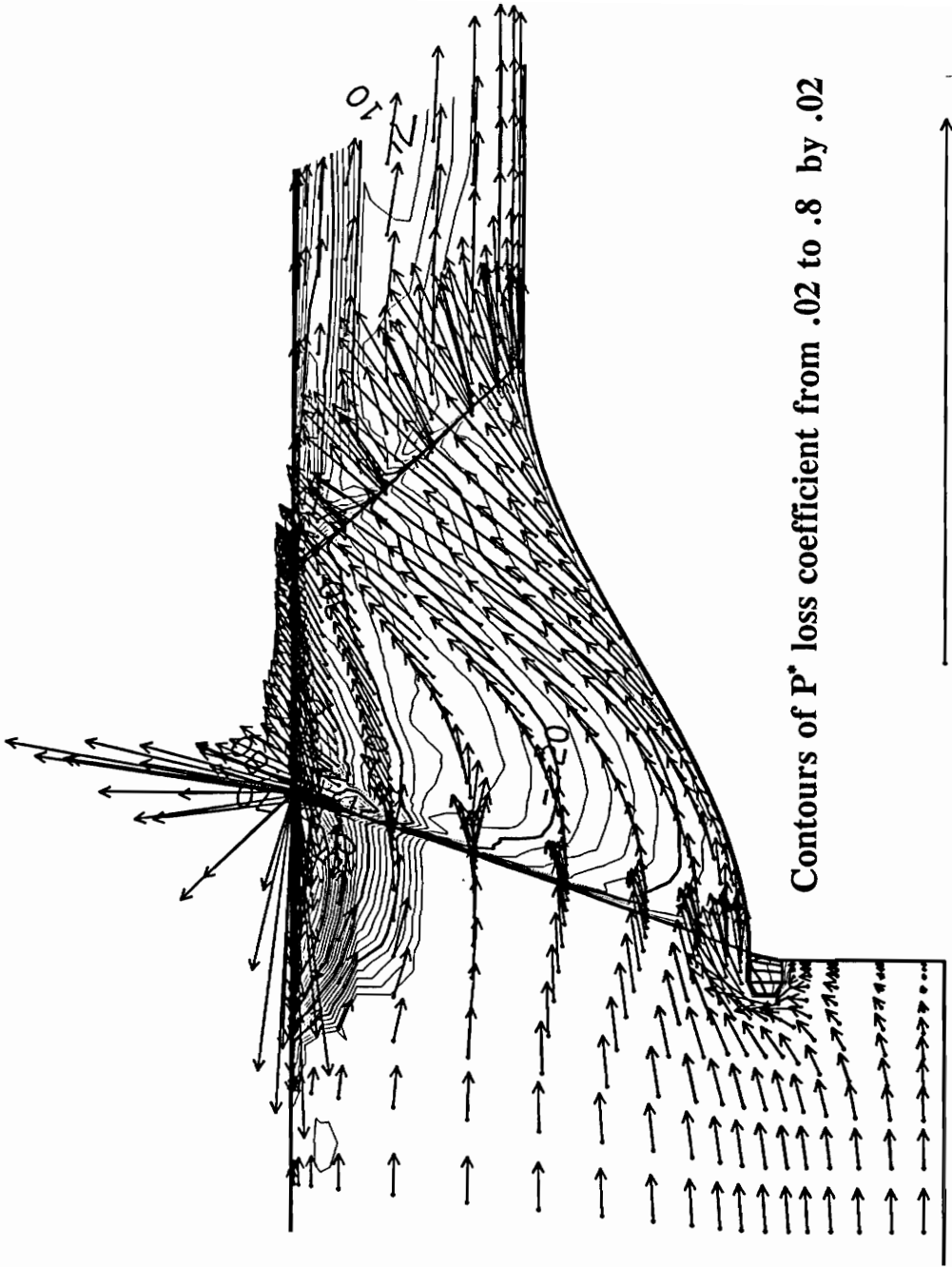
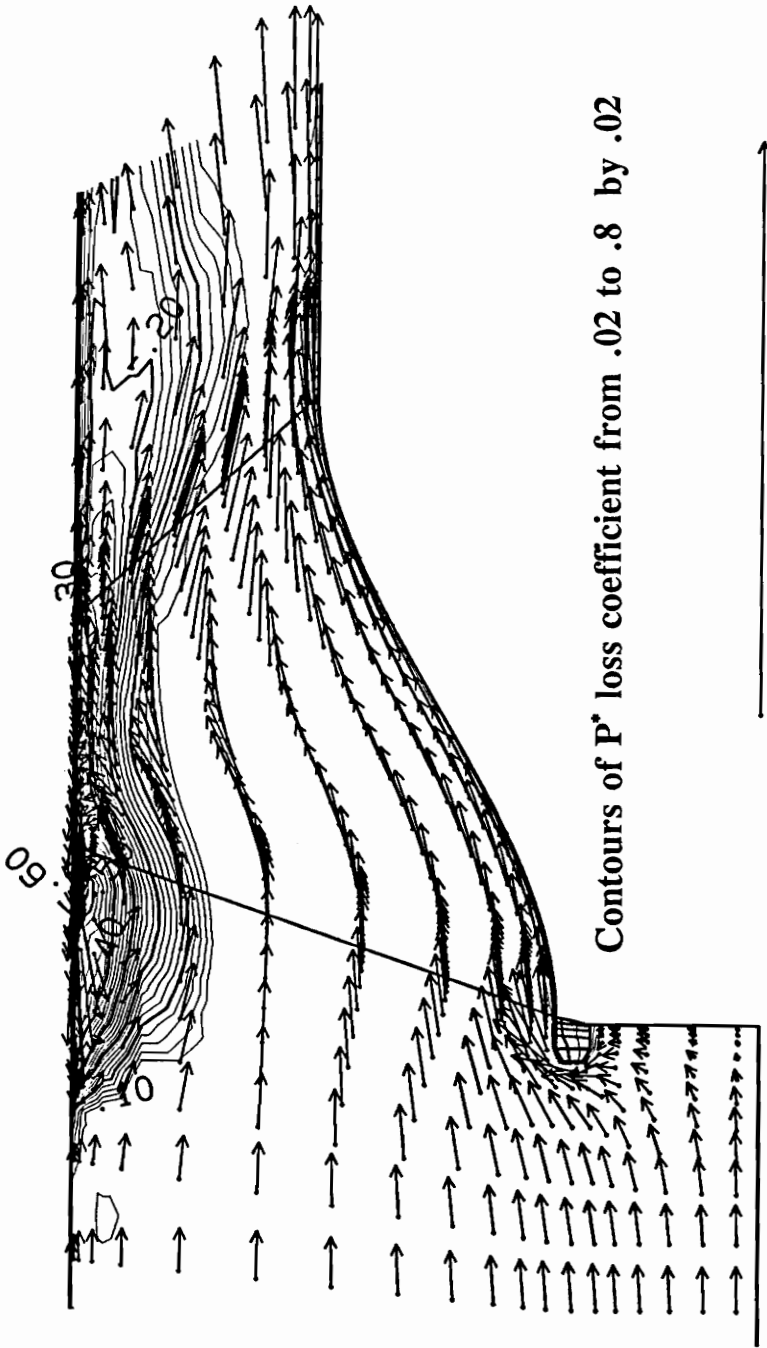


Figure 5.5 Meridional view near pressure surface of calculated P^* with velocity vectors at design flow rate.



Contours of P^* loss coefficient from .02 to .8 by .02

Figure 5.6 Meridional view near suction surface of calculated P^* with velocity vectors at design flow rate.



Contours of P^* loss coefficient from .02 to .8 by .02

Figure 5.7 Meridional view at mid-passage of calculated P^* with velocity vectors at design flow rate.

6 COMPARISON OF CALCULATION TO MEASUREMENT

6.1 Internal Data Planes

The 3-D laser measurements made by Rocketdyne were used for comparison. The locations of the 6 axial measurement planes are shown in Figure 4.3. The axial measurement planes A through E correspond to Figures 6.1 through 6.5. These five figures are axial views showing color contours of radial, tangential, and axial absolute velocities at design flow rate. The calculation results were interpolated to the 5 axial measurement planes. The calculated and measured results were both repeated to show the full 360 degrees, and were plotted on the same page for easy comparison. Note that the velocities are normalized with blade tip speed, U_{tip} . Also, the blade rotates in the $-\theta$ direction, clockwise.

There is both quantitative and qualitative agreement. Notice how the calculated velocity contours show the same colors, velocities, in the same locations as on the corresponding measured velocity contours. The velocity magnitudes as well as the flow patterns match well between the calculated and measured results.

Plane A is shown in Figure 6.1. Near the shroud the turbulence of the recirculation region prevented laser measurements. However, the existing measurements near the wall give some evidence of the negative tangential velocities, V_θ , and axial velocities, V_z , associated with the recirculation region. The calculation shows a thick ring of negative V_θ , indicating that work has been done on the flow. The corresponding layer of negative V_z is about half as thick, since the recirculation region is half backflow and half forward flow.

Planes B and C are shown in Figures 6.2 and 6.3. Notice in Plane B that the calculated radial velocities, V_r , are all outward. The general flow through inducer is radially outward due to hub ramping. There is no flow radially inward to balance the large outflows, since flow is carried upstream when it reaches the backflow near the shroud. V_r gets very large near the tip, because the tip leakage flow entrains the fluid radially outward from the blade tip corners and carries it upstream. There is a region

of strong backflow, $-V_z$, along the shroud on the pressure side. This strong backflow is caused by the incidence of tip leakage flow from the preceding blade.

Plane C shows radial inflow near the pressure side, evidence that secondary flow patterns begin to develop here. Plane C does not have strong tip leakage backflows as did Plane B. Otherwise, planes B and C are qualitatively very similar.

Figures 6.2 and 6.3 both show radial streaks through the measured radial velocity plots. These streaks are inconsistent with the rest of the flow and are considered errors in the measurement. The radial velocity is the most difficult to obtain, so it is understandable that there is some difficulty getting clean data.

Plane D is shown in Figure 6.4. The classic secondary flow patterns found in inducers, as presented by Lakshminarayana in Figure 2.1, are fully developed at Plane D. There is radially outward flow, $+V_r$, near the blades and radially inward flow, $-V_r$, at mid-passage. The largest radial outflow occurs near the suction surface where there are no measured velocities. V_θ is strongest at the shroud near the pressure side, because the radially outward flow along the pressure surface and the tip leakage flow from the preceding blade have built up low momentum fluid near the pressure surface. This region of high V_θ is stronger in the calculated results than the experimental results. Notice that the region of weak tangential velocity, V_θ , near the suction surface corresponds to a region of high axial velocity, V_z .

Plane E is just downstream of the blade. The radial velocities show the secondary flow patterns continue on downstream of the trailing edge. The axial and tangential velocities also have stronger and weaker regions corresponding to the jet and wake downstream of the blade. The higher calculated V_θ shows there is more work done than in the measured results.

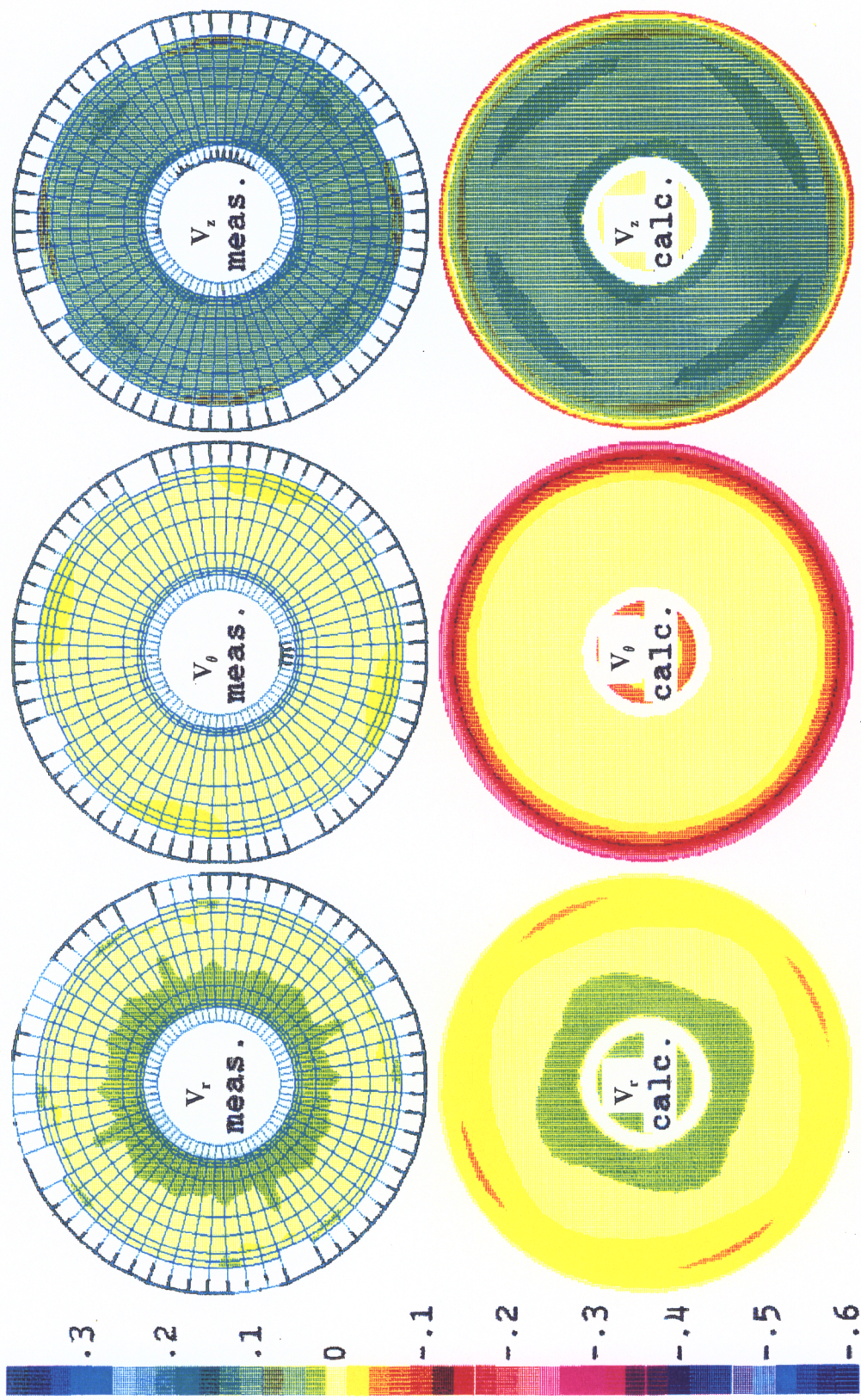


Figure 6.1 Axial comparison plane A, at $z/D = -0.0083$ showing calculated and measured velocity components at design flow rate.

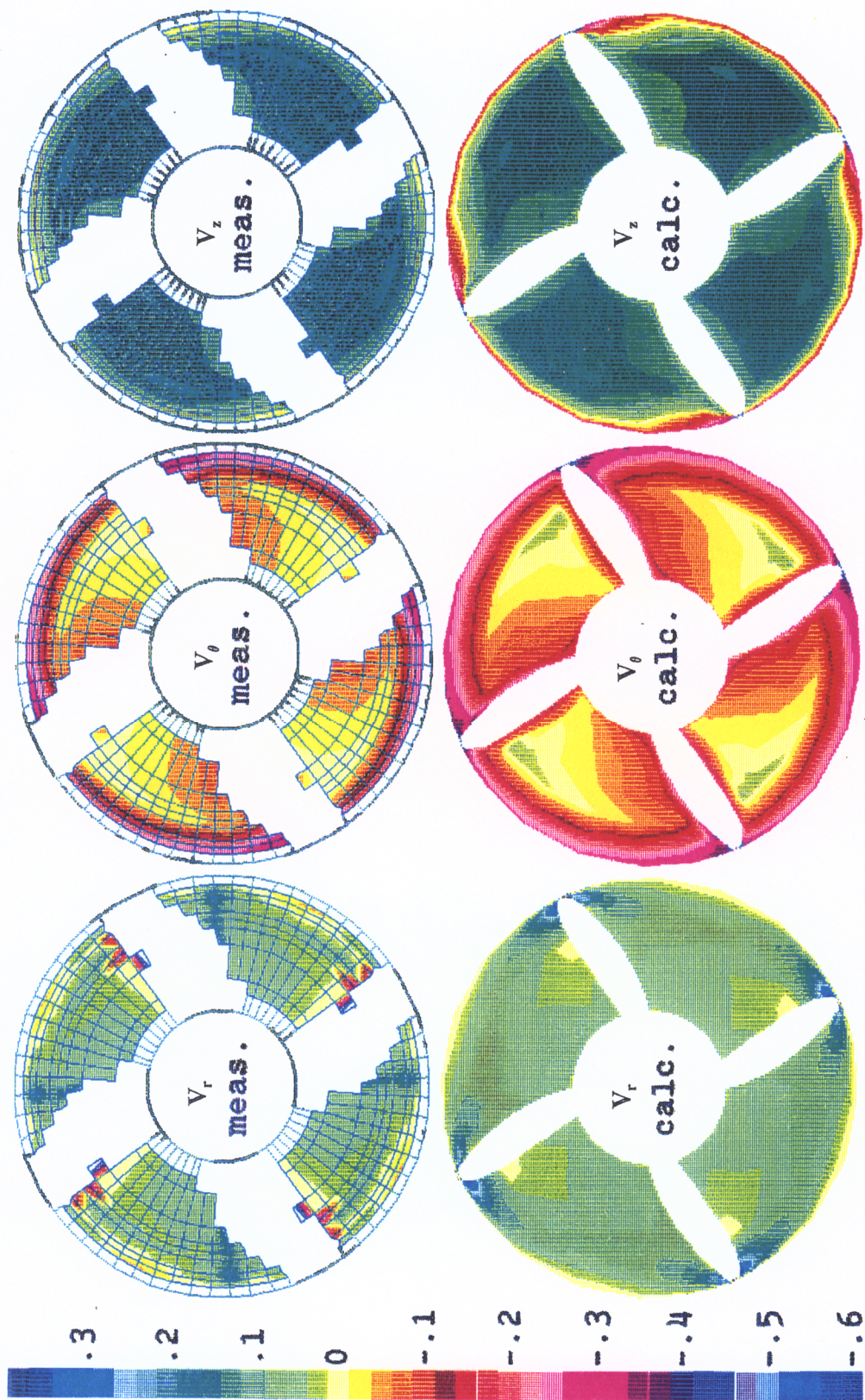


Figure 6.2 Axial comparison plane B, at $z/D = 0.1222$ showing calculated and measured velocity components at design flow rate.

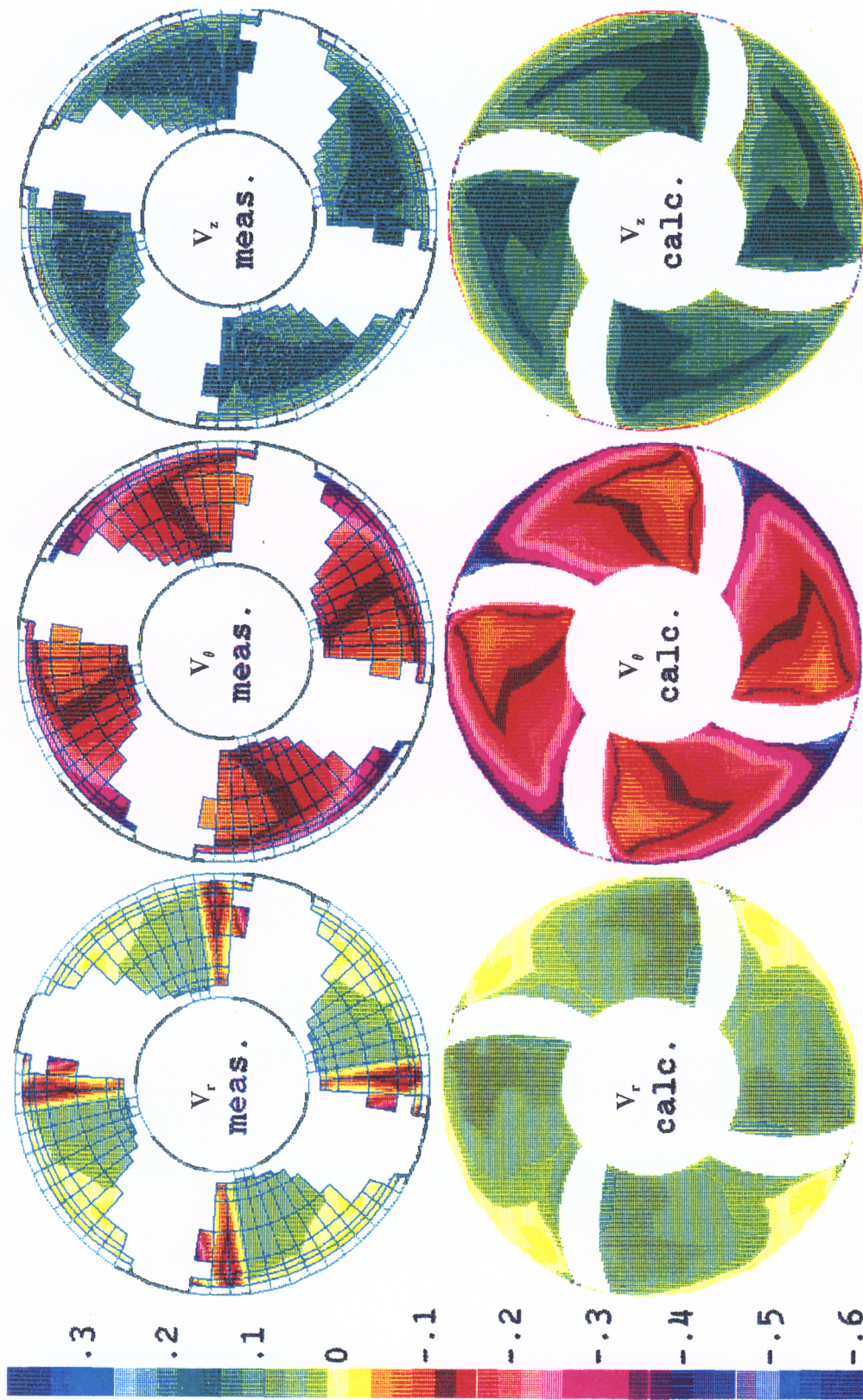


Figure 6.3 Axial comparison plane C, at $z/D = 0.1790$ showing calculated and measured velocity components at design flow rate.

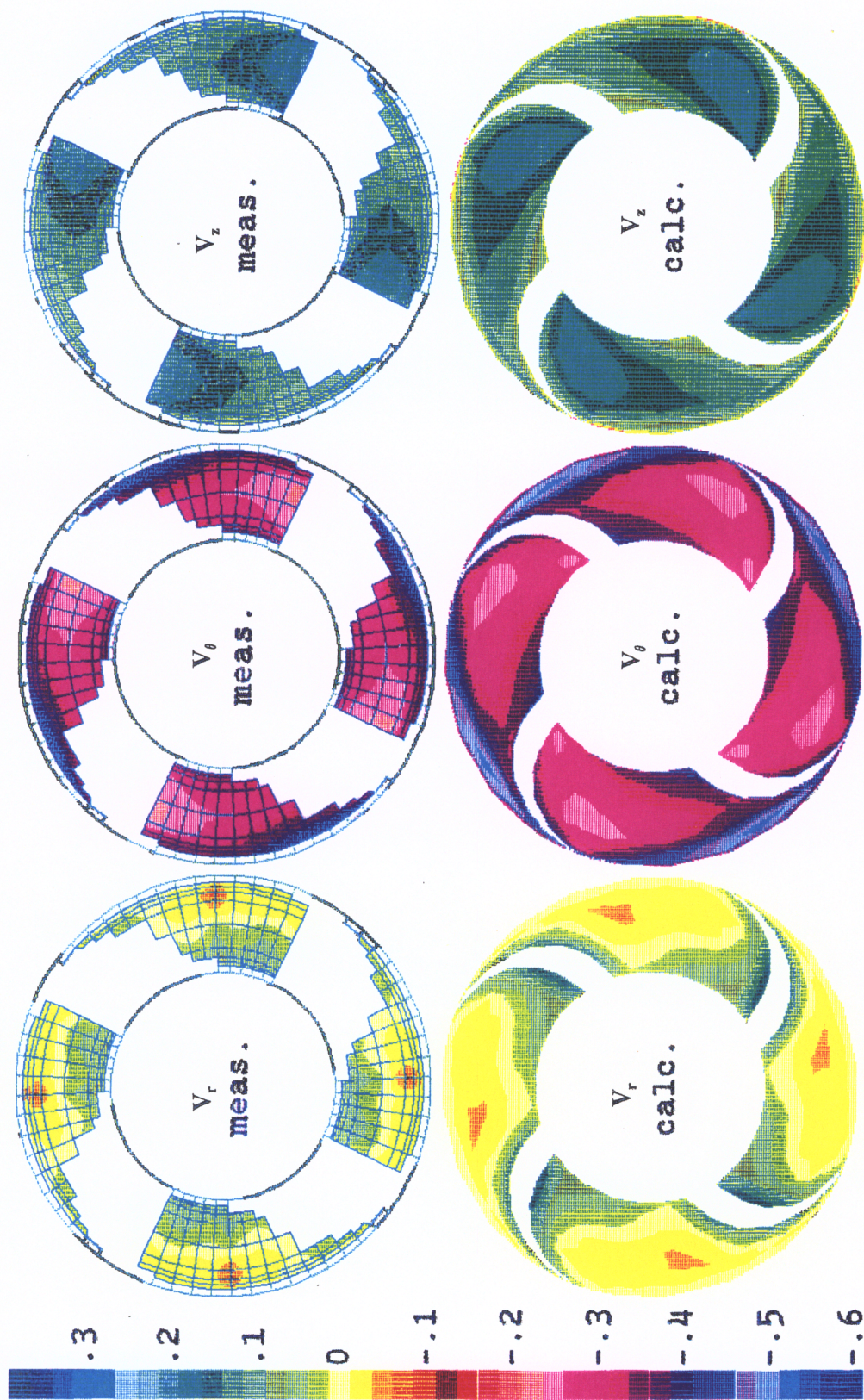


Figure 6.4 Axial comparison plane D, at $z/D = 0.2925$ showing calculated and measured velocity components at design flow rate.

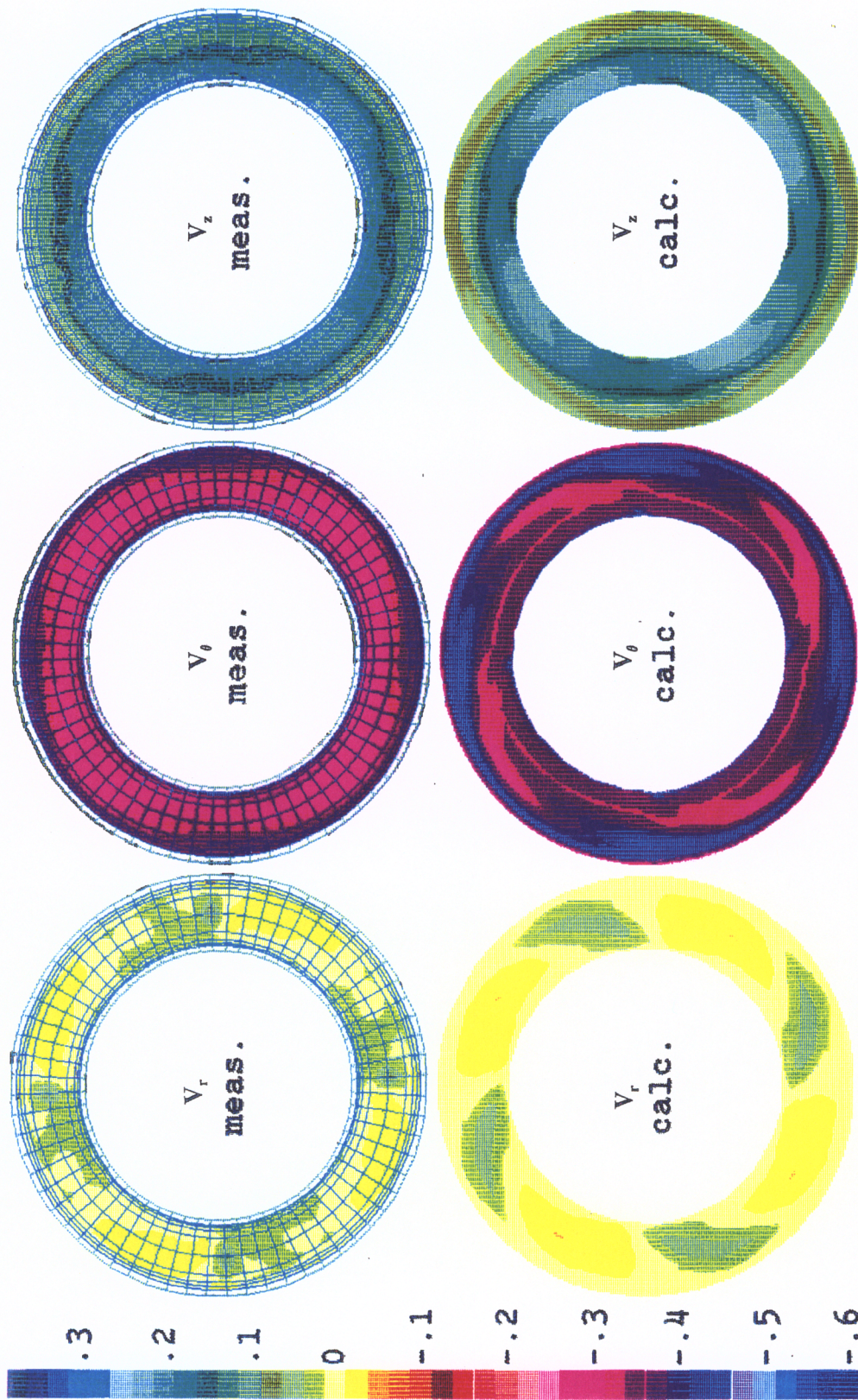


Figure 6.5 Axial comparison plane E, at $z/D = 0.4644$ showing calculated and measured velocity components at design flow rate.

6.2 Overall Performance

The impeller inlet survey plane is shown in Figure 4.3 as a dotted line downstream of the inducer. At the inlet survey plane 2-D laser measurements were made to define the inlet conditions for the impeller. This location is far enough from the impeller and the inducer that the pressure is essentially uniform circumferentially and the radial velocity is negligible. Some of the fluid is also assumed to reach the exit without any loss such that

$$P_{\max}^* = P_{\max,inlet}^* = P_{t,\max,inlet} = P_o \quad (1)$$

The radial equilibrium equation,

$$\frac{\partial P}{\partial r} = \rho \frac{V_\theta^2}{r} \quad (2)$$

is then solved to give the static pressure gradient as a function of radius and tangential velocity. All the pressures distributions are then calculated from the 2-D laser measurements using the pressure definitions given in Section 2.4.

The circumferentially averaged pressures and velocities are plotted in Figure 6.6 for comparison. Notice there is a large axial velocity distortion; the hub axial velocities are twice that of the tip. Both the axial velocity, and P^* , loss, distributions are well predicted by the calculation. The other parameters are modelled reasonably well, and are qualitatively correct. The calculated static and total pressures are higher than the measured results because the calculated work input is overpredicted by about 20%.

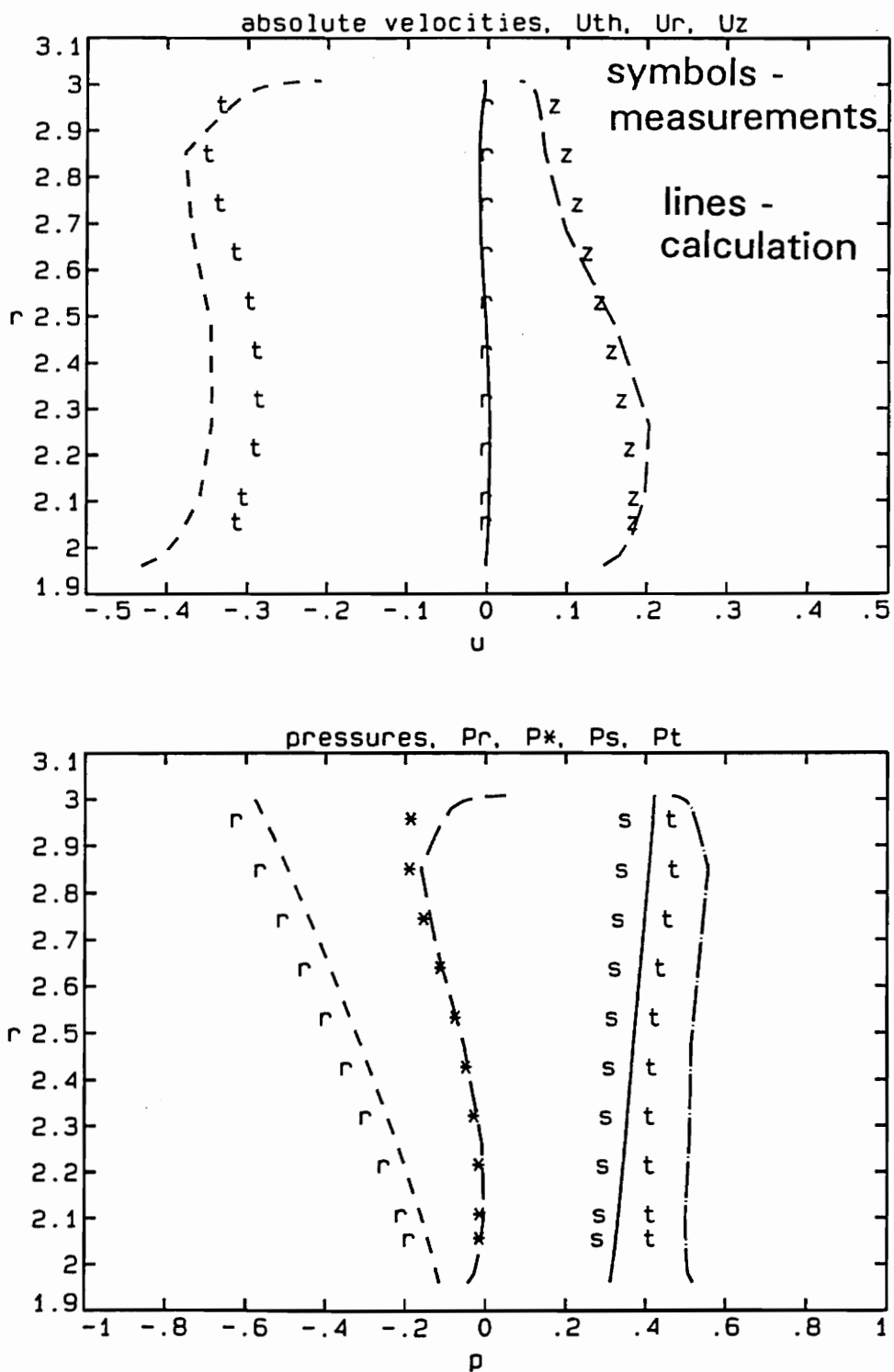


Figure 6.6 Circumferentially averaged pressures and velocities at impeller inlet survey plane

7 RECIRCULATION

The recirculation region is a toroidal shaped vortex at the tip leading edge of the blades easily seen in Figures 5.4, 5.5, and 5.6. The recirculation region is produced by the tip leakage flow and may be enhanced by incidence on the blade, a leading edge vortex, a 3-D horseshoe vortex, secondary flows within the passage, and the blockage formed by the backflow region itself. It is difficult to quantify these contributions to the recirculation region.

The tip leakage flow is most visible in Figure 7.1 , which is a blade-to-blade view of the velocity vectors in the tip gap, at the blade tip, $C=1.0$, near the tip, $C=.98$, and near the blade mid-height, $C=0.5$. Notice, the tip leakage velocity vectors have a strong component in the upstream direction. This is due to the high blade stagger angle and low flow coefficient. The tip leakage is driven by the pressure gradient across the blade, and is the main source of backflow.

Figure 7.2 shows meridional views of calculated static pressure at design flow rate. There are 12 view locations from the suction surface to the pressure surface, labeled in percent of the blade spacing. The location of the leading edge vortex is visible as a low pressure zone. It moves upstream and weakens as it extends across the passage from the leading edge suction surface. The vortex is mixed into the recirculation region as it approaches the leading edge of the next blade and is fully absorbed during the formation of the next vortex.

Figures 5.1, 5.2, 5.3, and 5.4 show meridional views of calculated velocity vectors at design flow rate. The backflow region is shown extending one sixth of the blade tip diameter upstream, where one diameter is 15.24 cm (6 inches). Figures 7.3, 7.4, 7.5, and 7.6 show meridional views of calculated velocity vectors and losses at 110% flow rate. The backflow region is now shown extending only one twelfth of the tip diameter upstream. Finally, Figures 7.7, 7.8, 7.9, and 7.10 show meridional views of calculated velocity vectors and losses at 89% flow rate. At this low flow rate a larger sustained backflow region is shown extending one half of the tip diameter upstream.

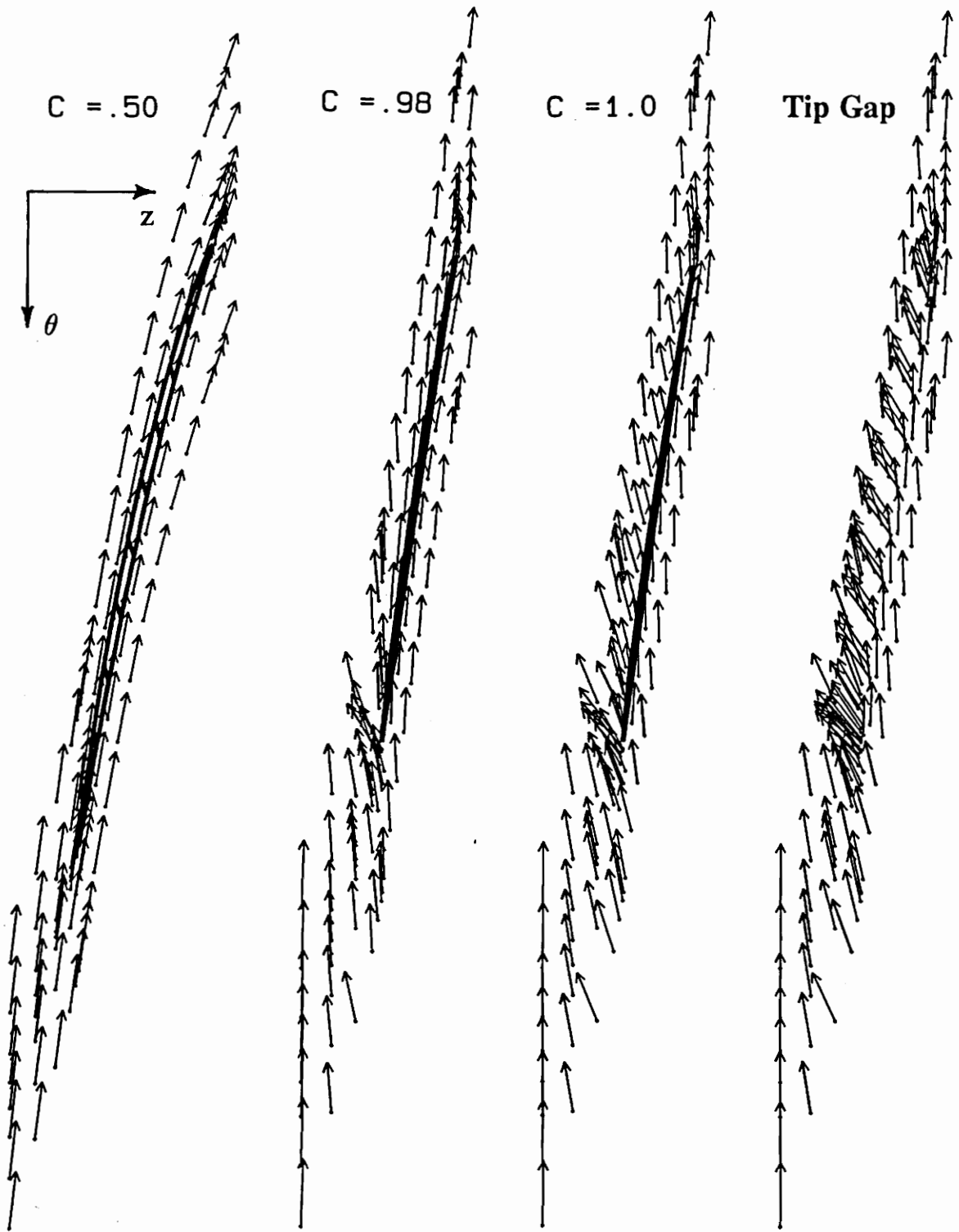


Figure 7.1

Blade-to-blade views showing tip leakage flow

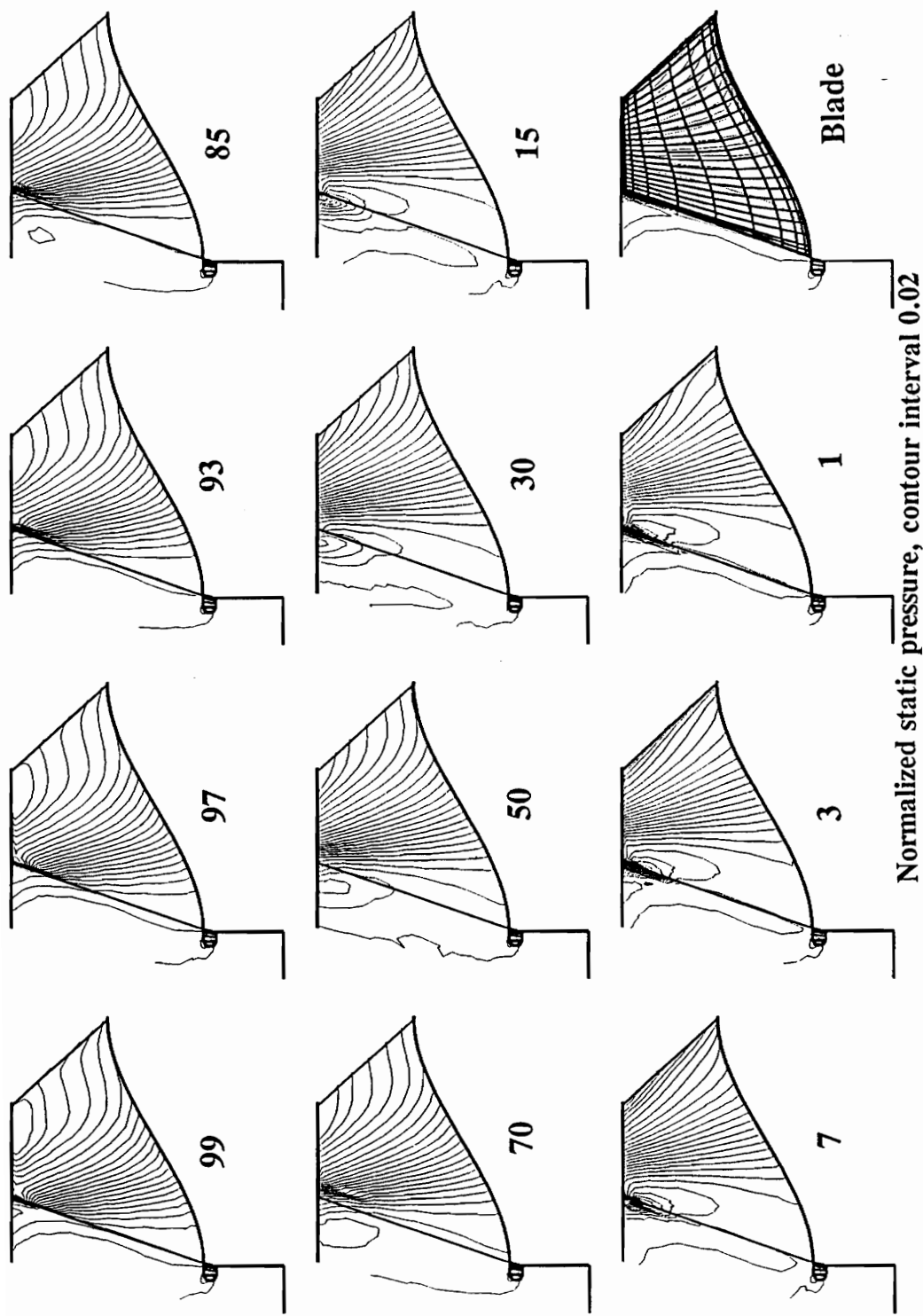


Figure 7.2 Meridional views of calculated static pressure at design flow rate, labeled in percent of the blade spacing

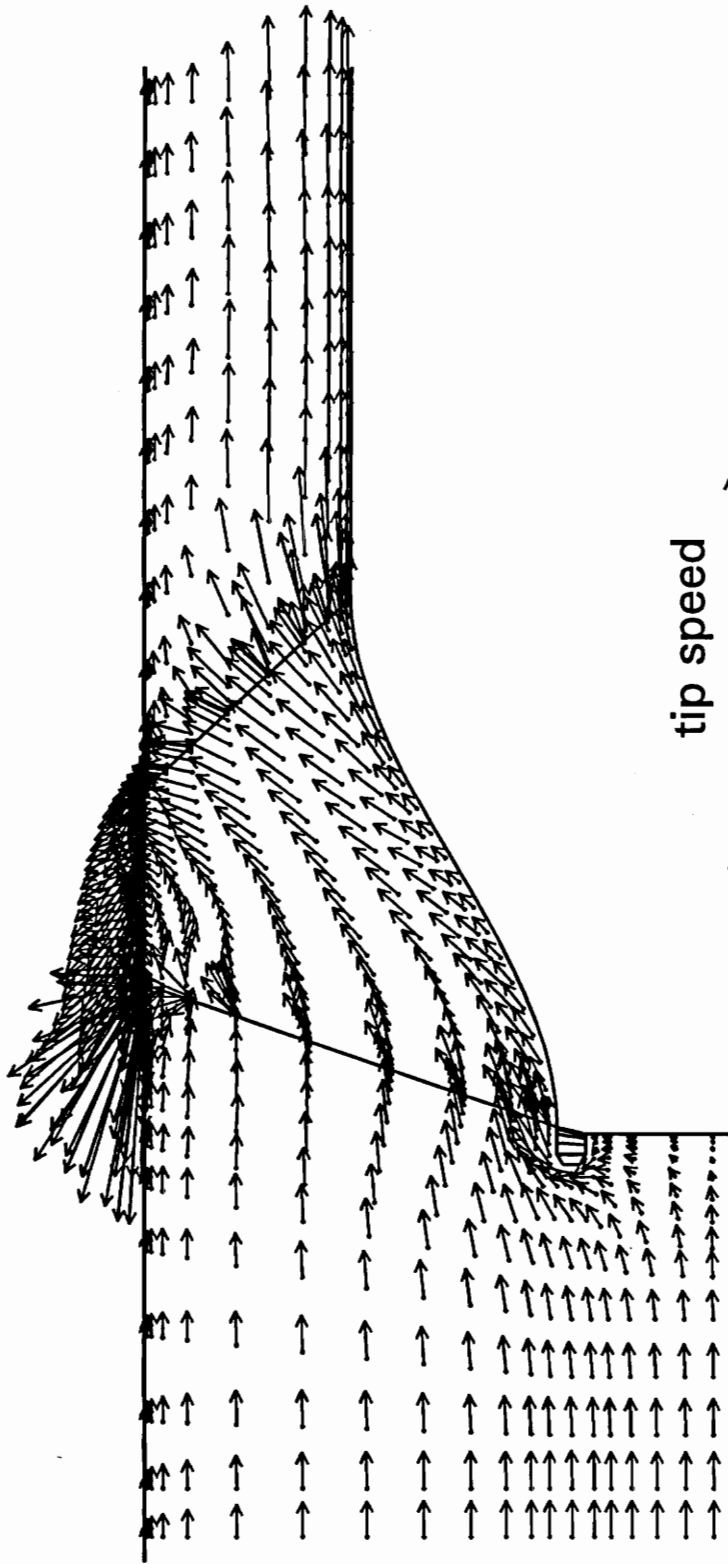


Figure 7.3 Meridional view near pressure surface of calculated velocity vectors at 110% flow rate.

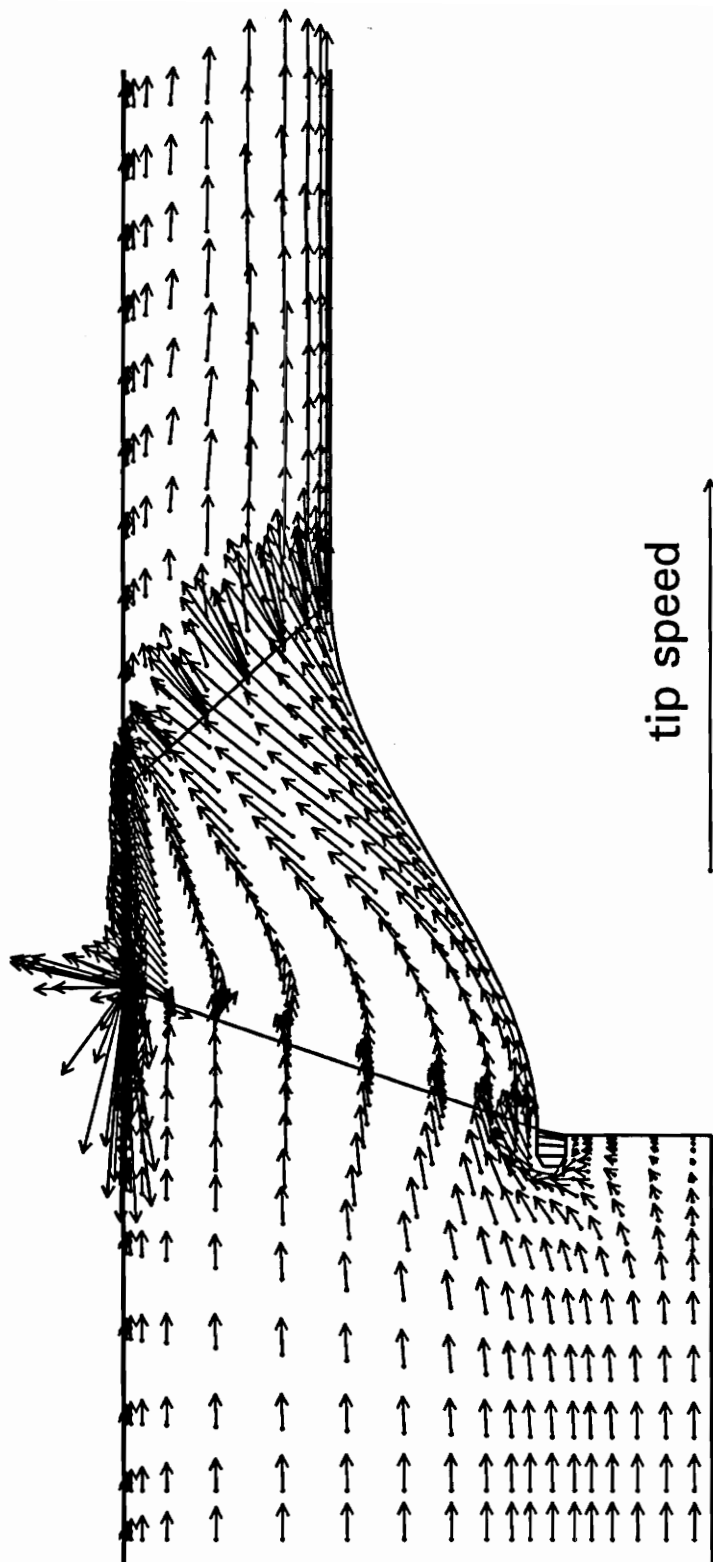


Figure 7.4 Meridional view near suction surface of calculated velocity vectors at 110% flow rate.

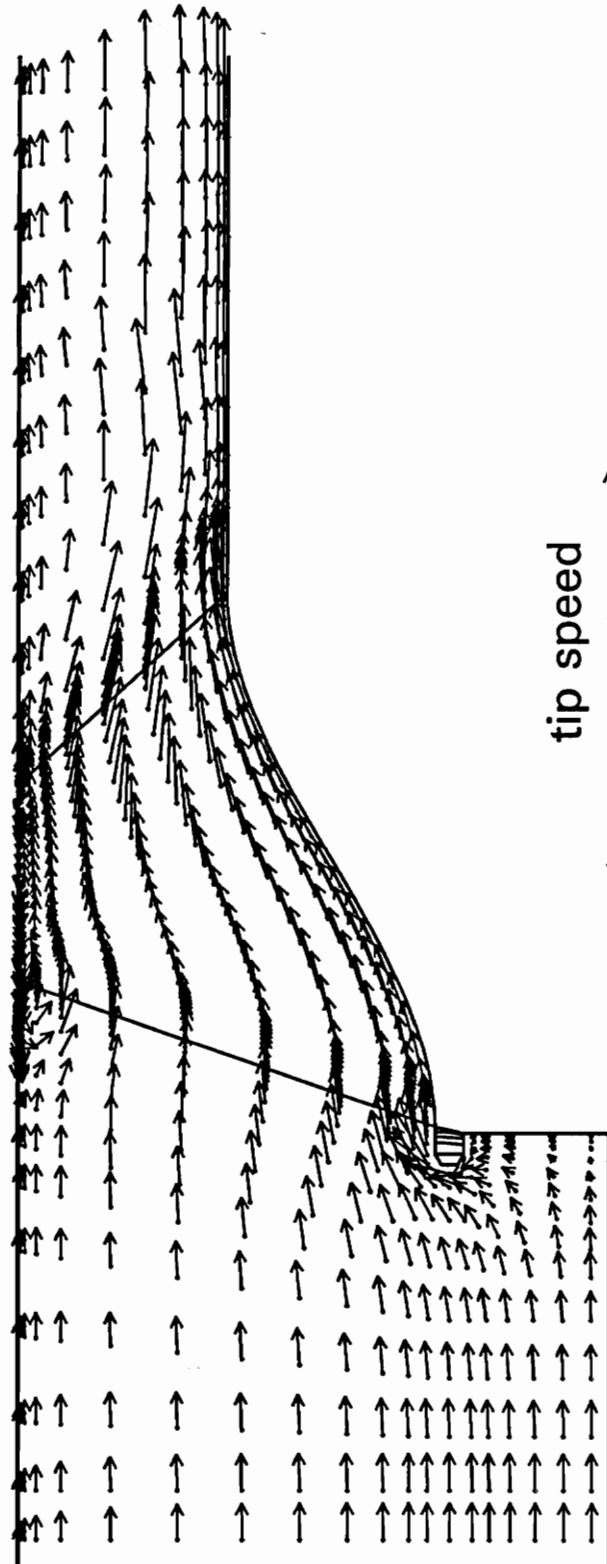
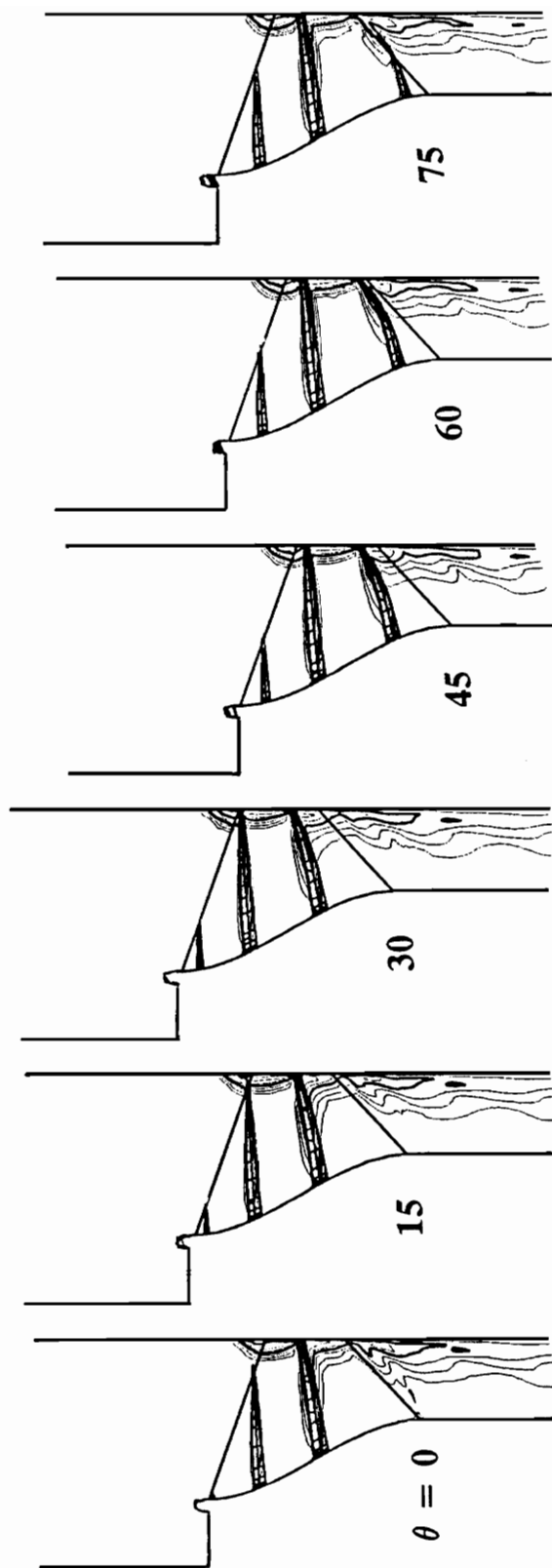


Figure 7.5 Meridional view at mid-passage of calculated velocity vectors at 110% flow rate.



Contours of P^* loss coefficient from .05 to .8 by .05

Figure 7.6 Meridional slices showing P^* at 110% flow rate

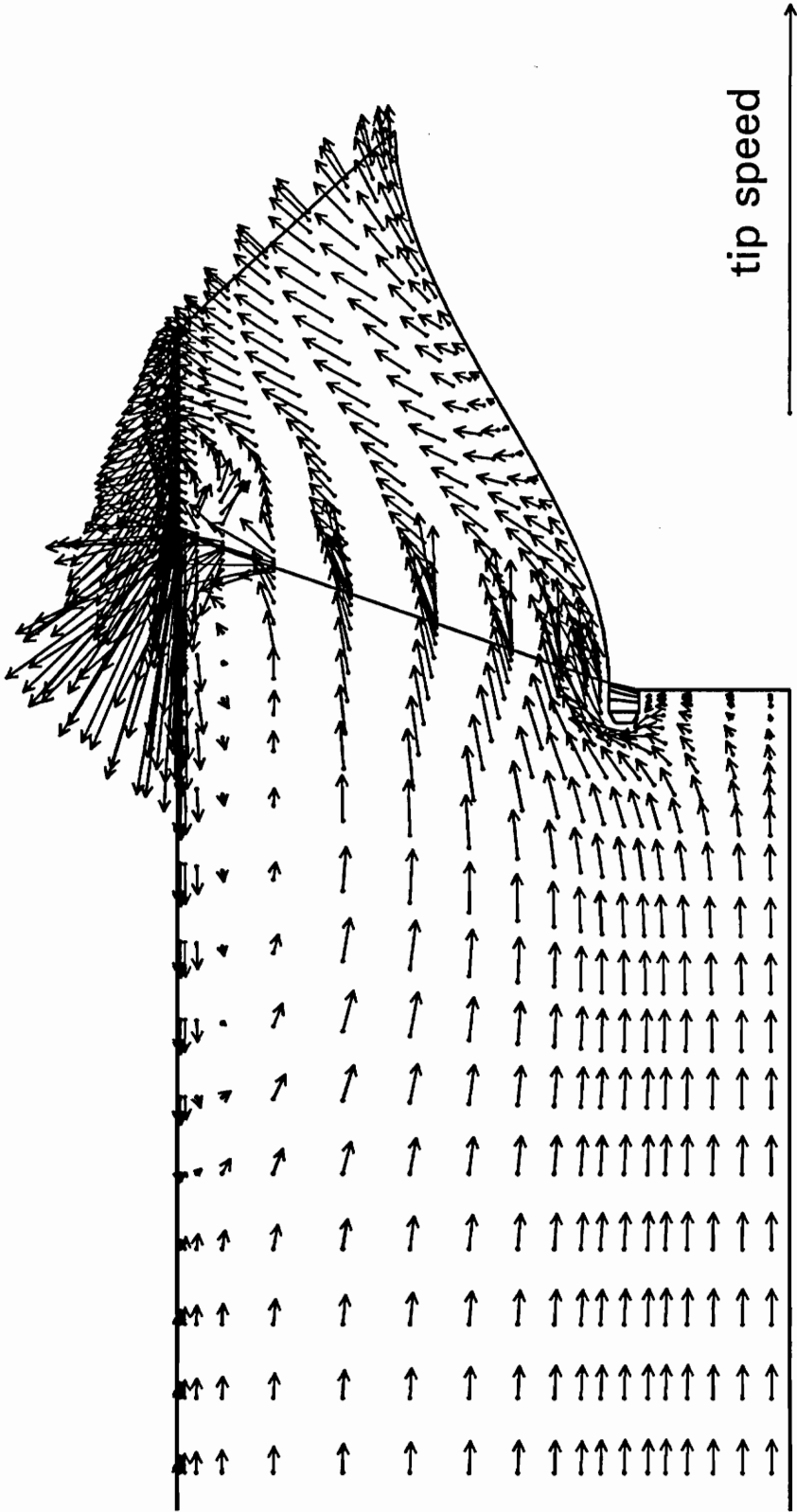


Figure 7.7 Meridional view near pressure surface of calculated velocity vectors at 89% flow rate.

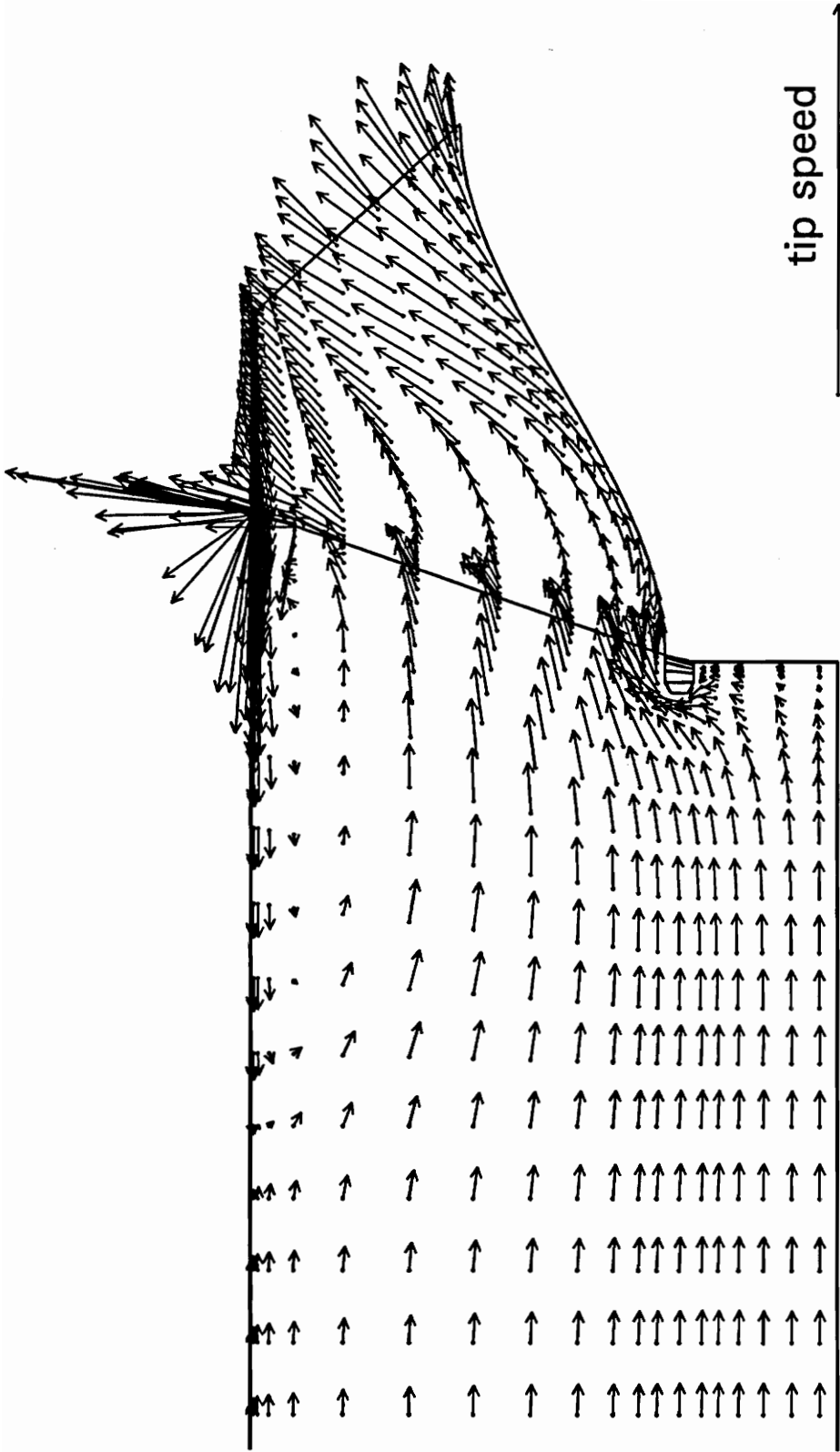


Figure 7.8 Meridional view near suction surface of calculated velocity vectors at 89% flow rate.

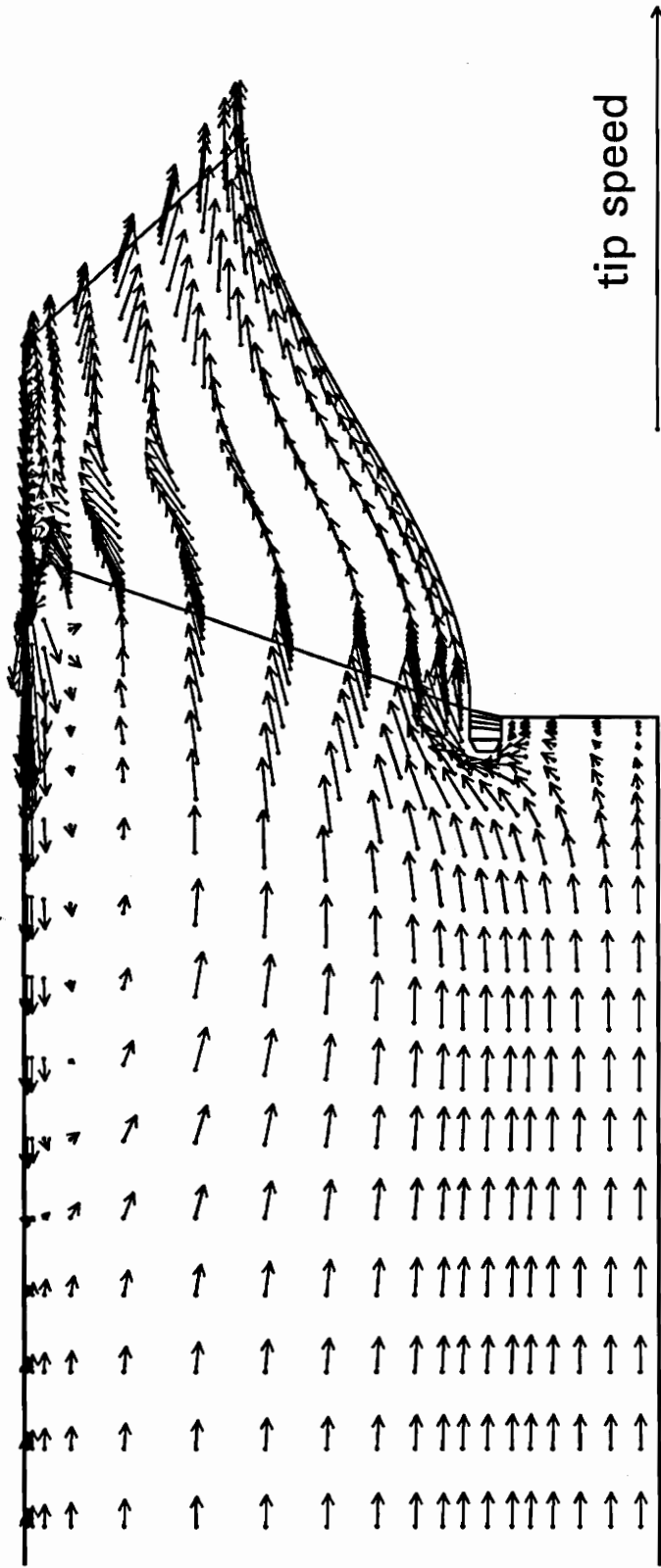
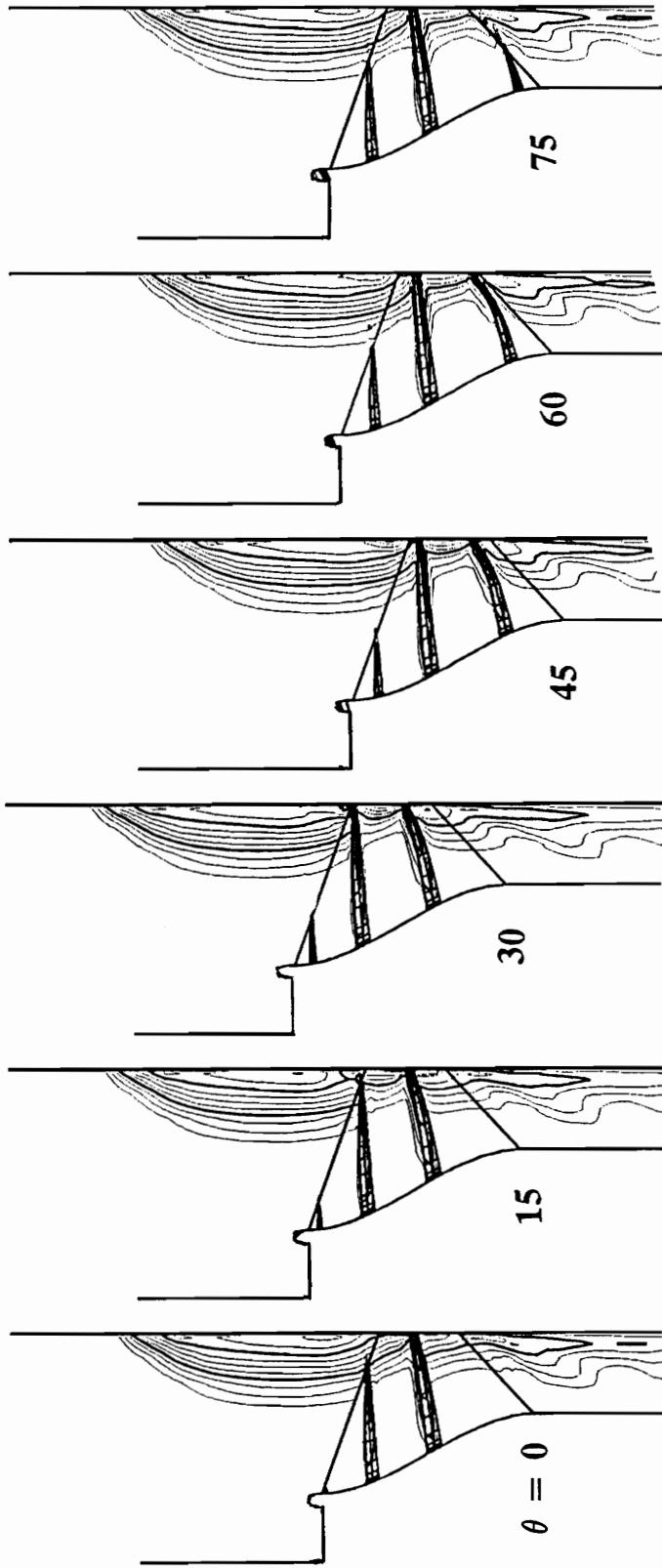


Figure 7.9 Meridional view at mid-passage of calculated velocity vectors at 89% flow rate.



Contours of P^* loss coefficient from .05 to .8 by .05

Figure 7.10 Meridional slices showing P^* at 89% flow rate

The backflow was integrated over each of the i -planes and normalized by the overall flow rate to obtain the normalized backflow plotted in Figure 7.11. The normalized backflow is plotted as a function of the axial parameter, A , which is shown in Figures 4.8 and 4.9. For all three flow rates the peak backflow occurs just upstream of the leading edge, $A=0$. The 89% flow rate has 22% of the flow across the surface going upstream and 122% of the flow across the surface going downstream. The overall flow in this case is the forward flow minus the backflow, 100%. Note that the changes in backflow are roughly proportional to the changes in flow rate. The head rise, shown later in Figures 8.1, 8.2, and 8.3, is also a function of the flow rate. This supports the hypothesis that the pressure difference across the blade drives the tip leakage which in turn drives the backflow.

The backflow also blocks part of the inlet flow. The effective inlet throat radius is reduced because the recirculation region forms a blockage around the outer annulus at the inlet. By comparing the recirculation region at the three flow rates it was shown that the backflow increased with decreasing flow rate. Therefore, the effective inlet throat radius decreases with decreasing flow rate.

The recirculation region also has an effect on the contributions to the total pressure rise. The centrifugal effect, $U_2^2 - U_1^2$, and the relative velocity effect, $W_2^2 - W_1^2$, are both altered by the change in effective inlet throat radius. The pump characteristic discussion in Section 8 explains the recirculation blockage effect on the total pressure rise contributions.

In the past, inducers have been designed using streamline curvature techniques. The significant effects of the recirculation region have been ignored. Just as secondary flows are a key factor in the design of axial turbine and compressor blades, the recirculation region and its effects should be influential in the design of inducers.

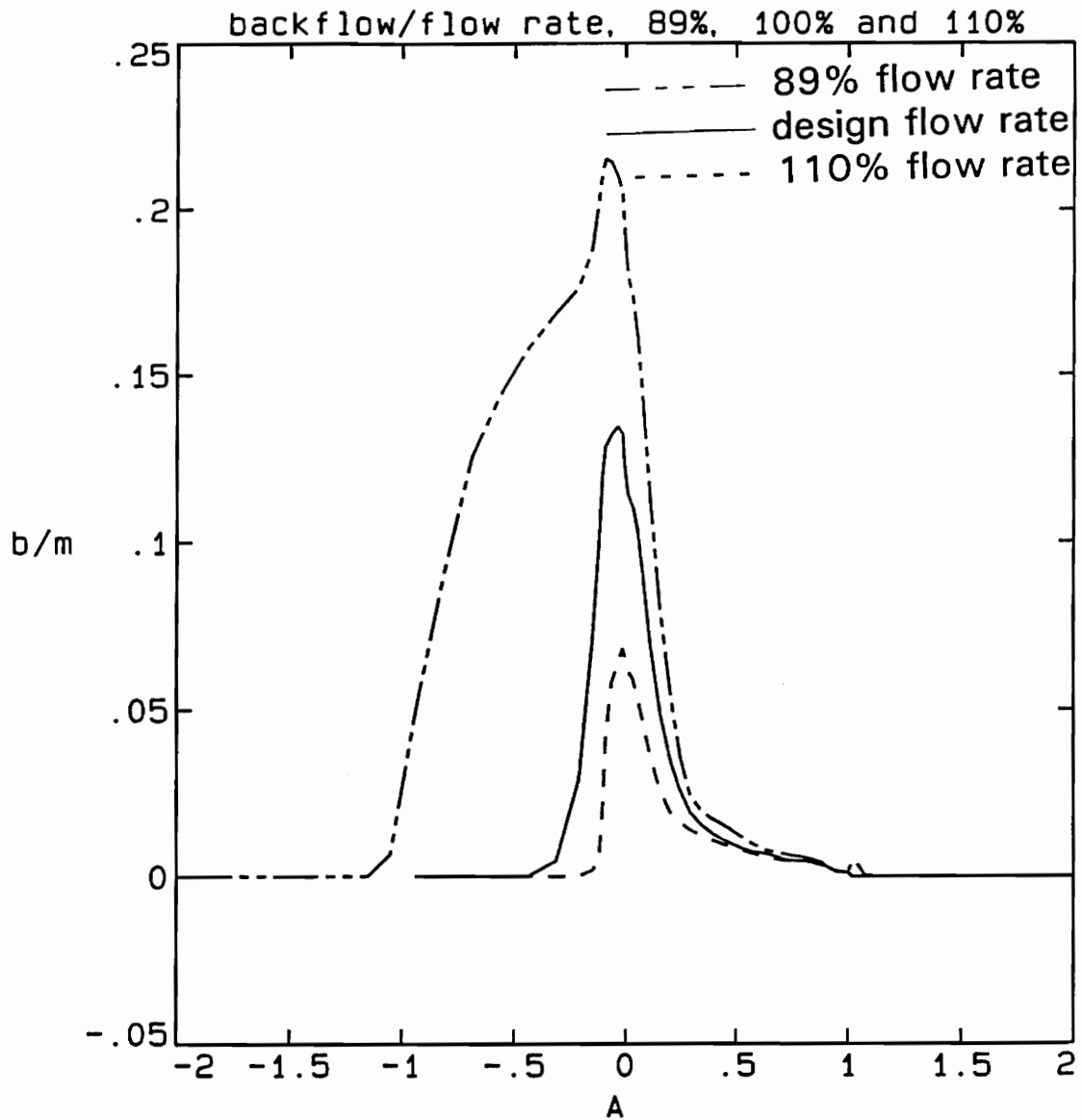


Figure 7.11 Backflow normalized with flow rate, plotted as a function of the axial parameter, A at 89%, design, and 110% flow rates

8 THERMODYNAMIC PERFORMANCE

8.1 Mass Averaged Properties

The pressures and velocities in the inducer were mass averaged over the i-grid planes, and are tabulated in Table 8.1. Note again that the A indices -1, 0, 1, and 2 correspond to the inlet, leading edge, trailing edge, and exit planes respectively, shown in detail in Figure 4.8. The properties listed are P^* , P , P_t , P_r , $U^2 = \omega^2 r^2$, W^2 , and V^2 . These properties are calculated and normalized as discussed in Section 2.4.

Figures 8.1, 8.2, and 8.3 show the development of the pressures as a function of the axial parameter, A, for the three flow rates. Notice the fluctuation in reduced pressure, P_r , upstream of the leading edge. This increase in reduced pressure is strongest at 89% flow rate where the recirculation region is the largest. Note that the usual definition of the head coefficient, ψ , is one half of the total pressure parameter listed in the tables and plotted in the figures.

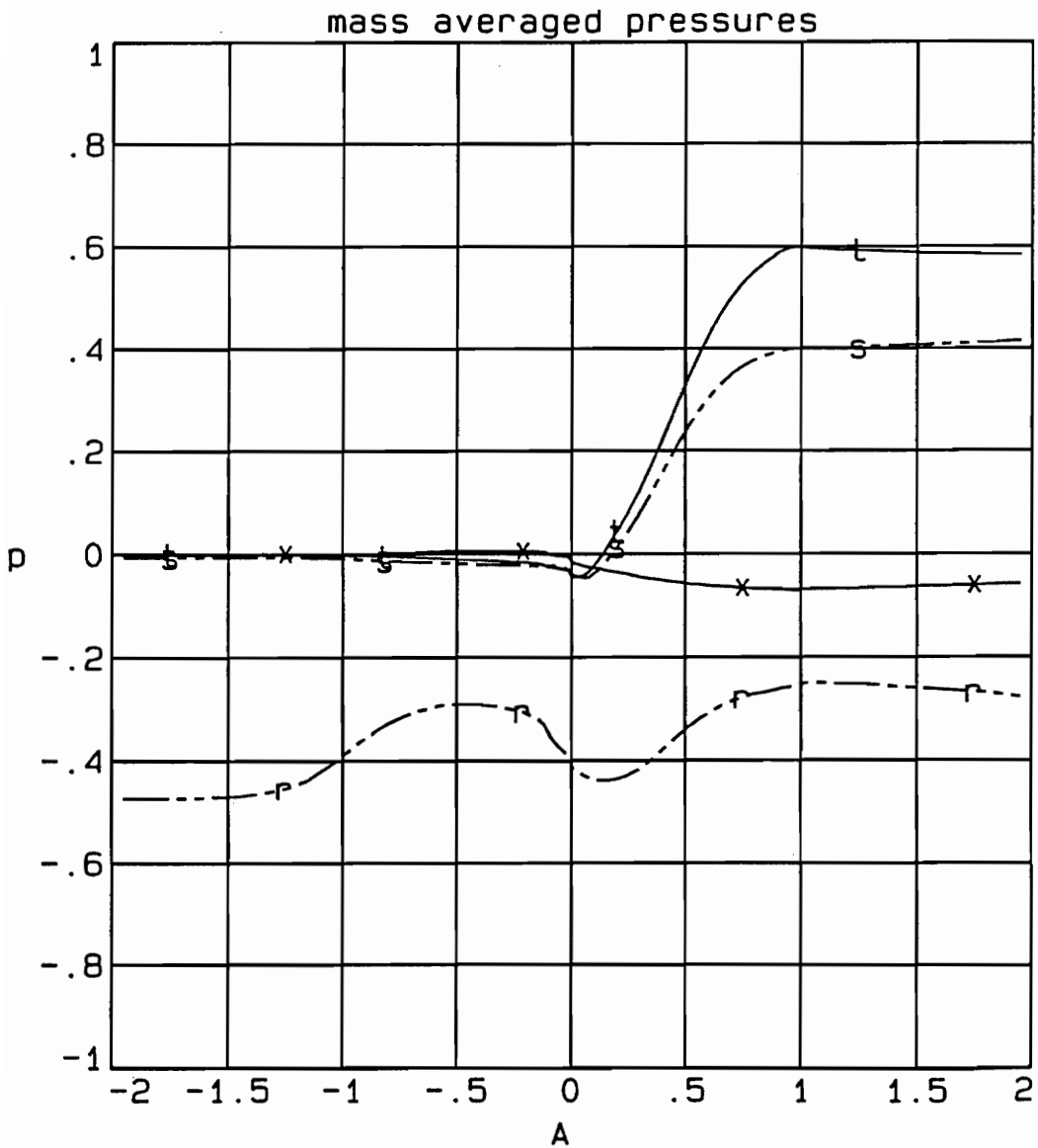
8.2 Contributions to Static and Total Pressure Rise

The definitions of rotary stagnation pressure and absolute total pressure, as shown in section 2.4, may be combined to form two equations for the static and total pressure rise across the inducer, shown on Tables 8.2 and 8.3. These equations express the pressure rises as a function of centrifugal effects, relative and absolute kinetic energy changes, and losses. The pressure rises are evaluated from leading edge(A=0) to trailing edge(A=1). Remember, no work is done by the inducer blades upstream of the inlet face. Also, note that high loss fluid is convected upstream through the recirculation region and then back to the inducer inlet. The contributions to head rise in Tables 8.2 and 8.3 are plotted with the pump characteristic, Figures 8.4 and 8.5.

In comparison to the SEP inducer previously studied by J. Moore, T. Le Fur, and J. G. Moore (9), the Rocketdyne inducer has a significant contribution from the change in relative kinetic energy. In fact, at the design flow rate, the relative kinetic energy change is about the same as the contribution from the centrifugal effect.

Table 8.1 Mass Averaged Pressures and Velocities

A	P*	P	P _t	P _r	$\frac{P-P_r}{U^2}$	$\frac{P^*-P_r}{W^2}$	$\frac{P_r-P}{V^2}$
89% Flow Rate							
-2.	0.0002	-0.0059	-0.0008	-0.4746	0.4687	0.4748	0.0051
-1.	-0.0023	-0.0103	-0.0022	-0.3681	0.3578	0.3658	0.0081
0.	-0.0125	-0.0364	-0.0411	-0.4070	0.3706	0.3945	-0.0047
1.	-0.0705	0.3998	0.5996	-0.2556	0.6554	0.1851	0.1998
2.	-0.0583	0.4151	0.5833	-0.2777	0.6928	0.2194	0.1682
Design Flow Rate							
-1.	-0.0011	-0.0075	-0.0010	-0.4770	0.4695	0.4759	0.0065
0.	-0.0111	-0.0250	-0.0205	-0.4664	0.4414	0.4553	0.0045
1.	-0.0640	0.3608	0.5306	-0.2955	0.6563	0.2315	0.1698
2.	-0.0554	0.3640	0.5190	-0.2939	0.6579	0.2385	0.1550
110% Flow Rate							
-1.	-0.0007	-0.0090	-0.0012	-0.4789	0.4699	0.4782	0.0078
0.	-0.0078	-0.0189	-0.0086	-0.5156	0.4967	0.5078	0.0103
1.	-0.0590	0.3231	0.4671	-0.3378	0.6609	0.2788	0.1440
2.	-0.0531	0.3254	0.4589	-0.3340	0.6594	0.2809	0.1335

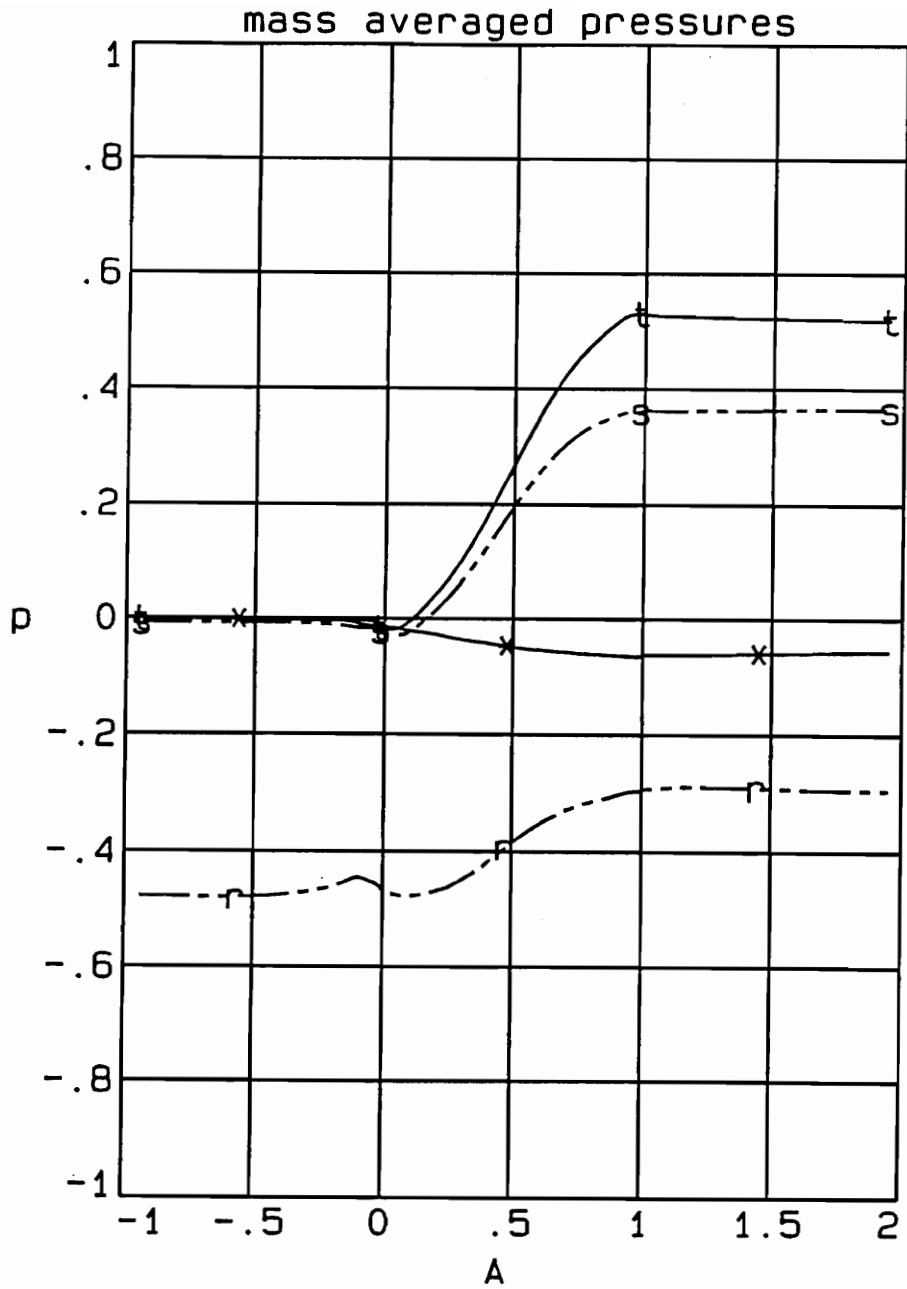


s-static, t-total, *-rotary stagnation, r-reduced

$$(p-p_o) / \frac{1}{2} \rho (\omega r_{tip})^2$$

Figure 8.1

The development of the pressures as a function of the axial parameter, A, at 89% flow rate

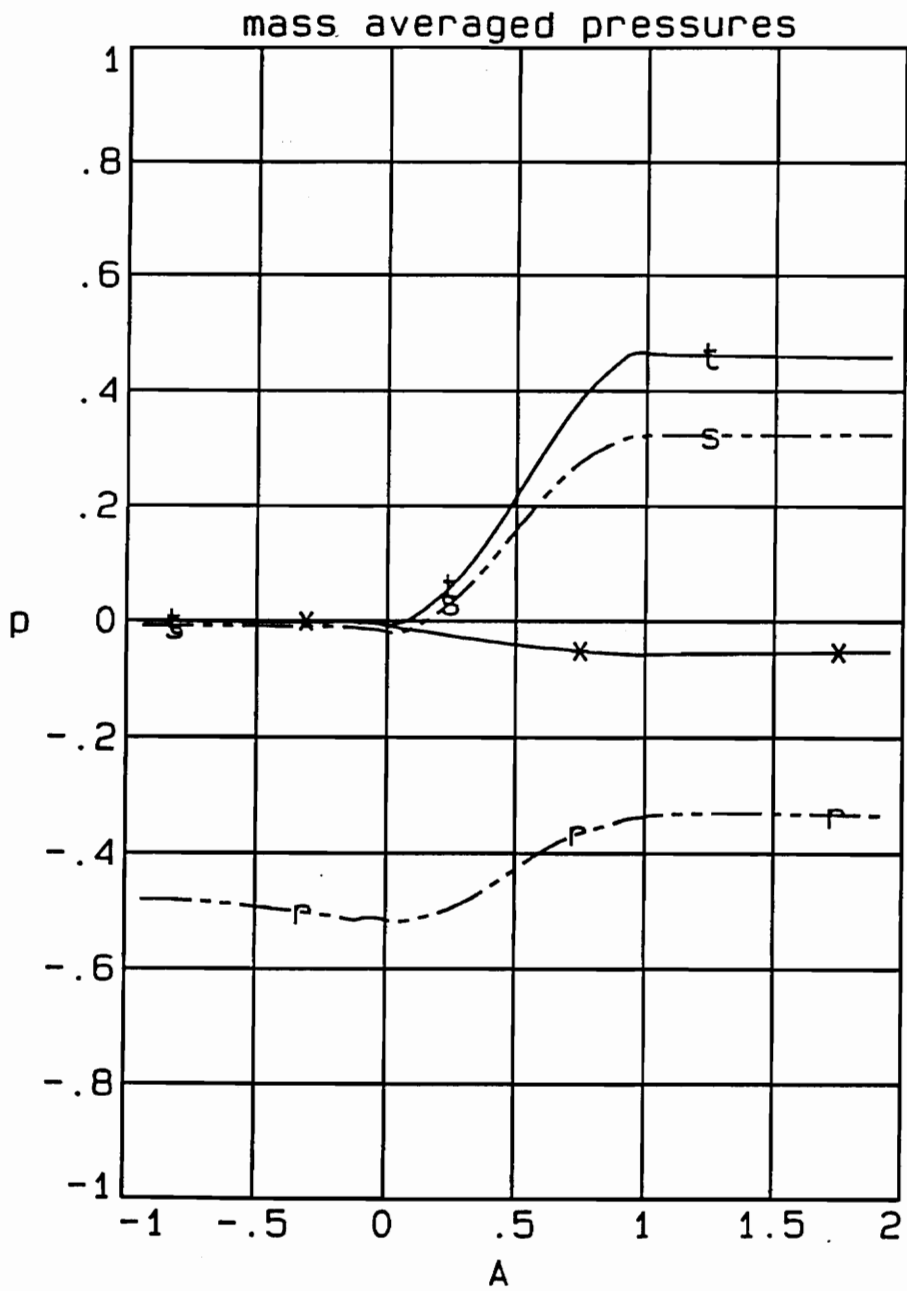


s-static, t-total, *-rotary stagnation, r-reduced

$$\frac{(p-p_o)}{\frac{1}{2} \rho (\omega I_{tip})^2}$$

Figure 8.2

The development of the pressures as a function of the axial parameter, A, at design flow rate



s-static, t-total, *-rotary stagnation, r-reduced

$$(p-p_o) / \frac{1}{2} \rho (\omega R_{tip})^2$$

Figure 8.3 The development of the pressures as a function of the axial parameter, A, at 110% flow rate

Table 8.2 Components of Static Pressure Rise

$$P_2 - P_i = U_2^2 - U_i^2 + W_i^2 - W_2^2 - (P_i^* - P_2^*)$$

centrifugal relative k.e. loss

89% Flow Rate

$$0.436 = 0.285 + 0.209 - 0.058$$

Design Flow Rate

$$0.385 = 0.215 + 0.224 - 0.053$$

110% Flow Rate

$$0.342 = 0.164 + 0.229 - 0.051$$

Table 8.3 Components of Total Pressure Rise

$$P_{t2} - P_{ti} = U_2^2 - U_i^2 + W_i^2 - W_2^2 + V_2^2 - V_i^2 - (P_i^* - P_2^*)$$

centrifugal relative k.e. absolute k.e. loss

89% Flow Rate

$$0.641 = 0.285 + 0.209 + 0.205 - 0.058$$

Design Flow Rate

$$0.551 = 0.215 + 0.224 + 0.165 - 0.053$$

110% Flow Rate

$$0.476 = 0.164 + 0.229 + 0.134 - 0.051$$

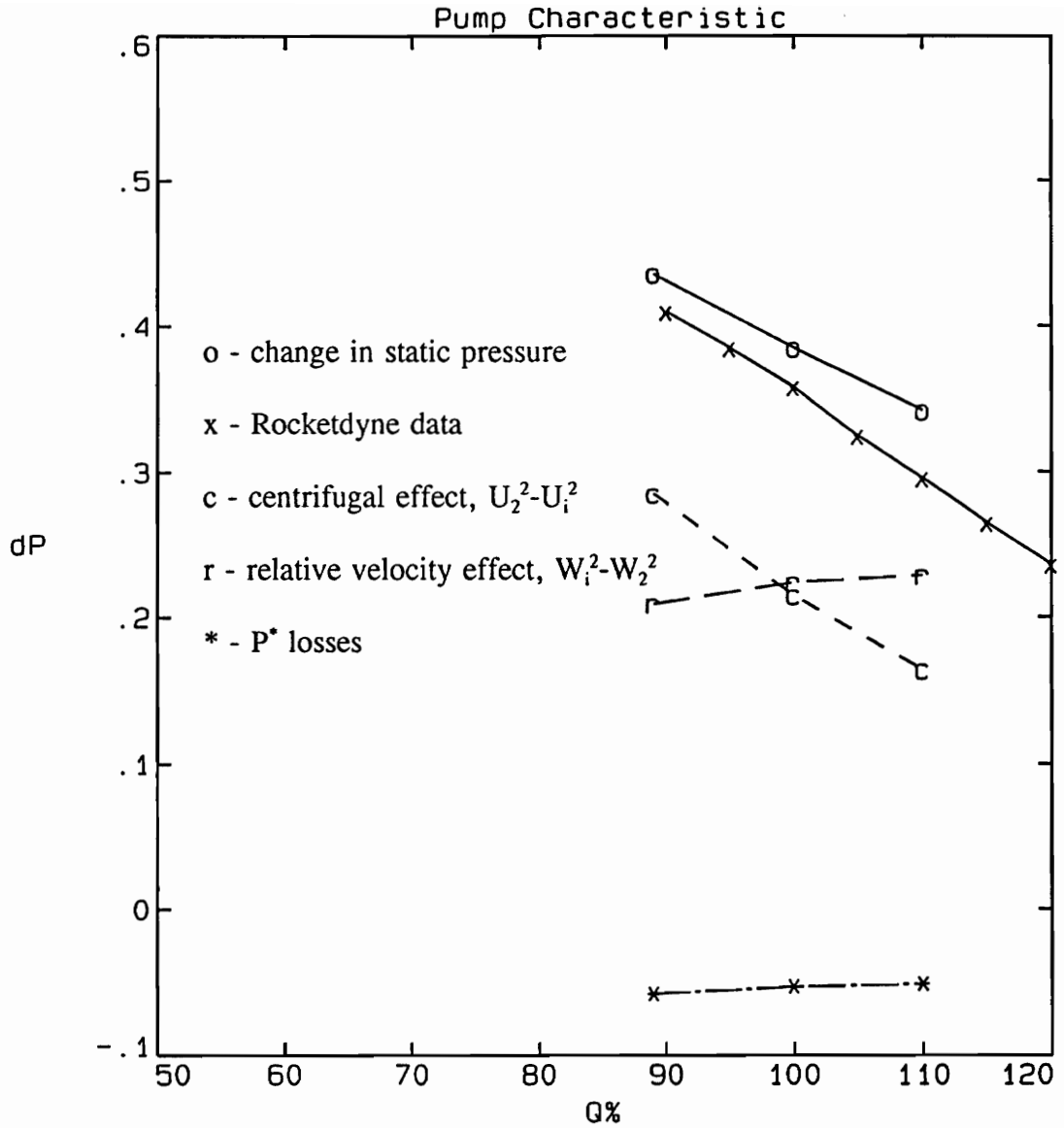


Figure 8.4 Pump Characteristic - static pressure rise characteristic plotted as a function of flow rate

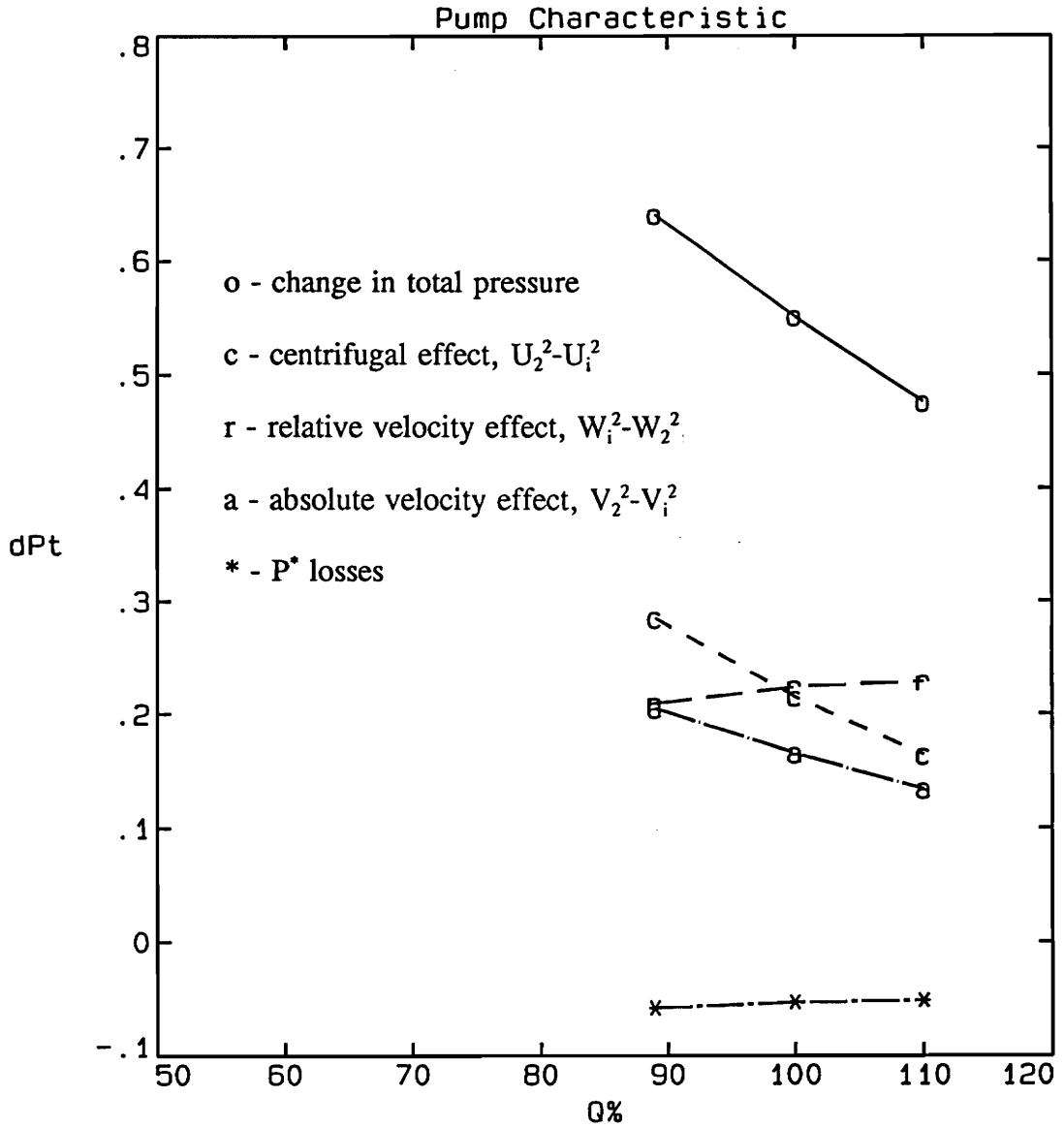


Figure 8.5 Pump Characteristic - total pressure rise characteristic plotted as a function of flow rate

8.3 Pump Characteristic

The head or pressure rise plotted as a function of flow rate is commonly known as the pump characteristic. The static pressure rise characteristic, Figure 8.4, shows both measured and calculated values. Note that the experimental static pressures were measured at the shroud. The shroud pressure at the exit is higher than the average exit pressure due to the swirling flow and radial equilibrium. Again, it is evident that the calculated pressure rise is overpredicted. Similarly, the total pressure rise characteristic, Figure 8.5, is plotted along with its contributions.

As mentioned in section 7 the recirculation region forms a blockage, which grows with decreasing flow rate. The blockage reduces the effective mean inlet radius. The relative flow diagrams, Figure 8.6, show that a reduced effective mean inlet radius also reduces U_i and W_i . The centrifugal effect is governed by U_i , and the relative velocity effect is governed by W_i .

At a low flow rate the blockage is larger and the flow has a larger change in radius from inlet to exit, therefore the centrifugal effect, $U_2^2 - U_i^2$, is larger. Conversely, at a high flow rate the blockage is smaller and the flow has a smaller change in radius from inlet to exit, therefore the centrifugal effect is smaller.

Again, at a low flow rate the blockage is larger and effective mean inlet radius is reduced. The relative inlet velocity, W_i , is smaller, therefore the relative velocity effect, $W_i^2 - W_2^2$, is smaller. The opposite is also true, at a high flow rate the effect of slowing the relative velocity is larger.

Notice that the recirculation blockage completely changes the shape of the relative velocity effect and the centrifugal effect. Normally, without a blockage, the centrifugal effect would be constant with flow rate. The relative velocity effect normally decreases with increasing flow rate, and defines the shape of the pump characteristic. With the blockage, however, the relative velocity effect increases and the centrifugal effect decreases with increasing flow rate. This can be seen in the pump characteristic, Figure 8.5. The centrifugal effect and the change in absolute kinetic energy determine the shape of this pump characteristic.

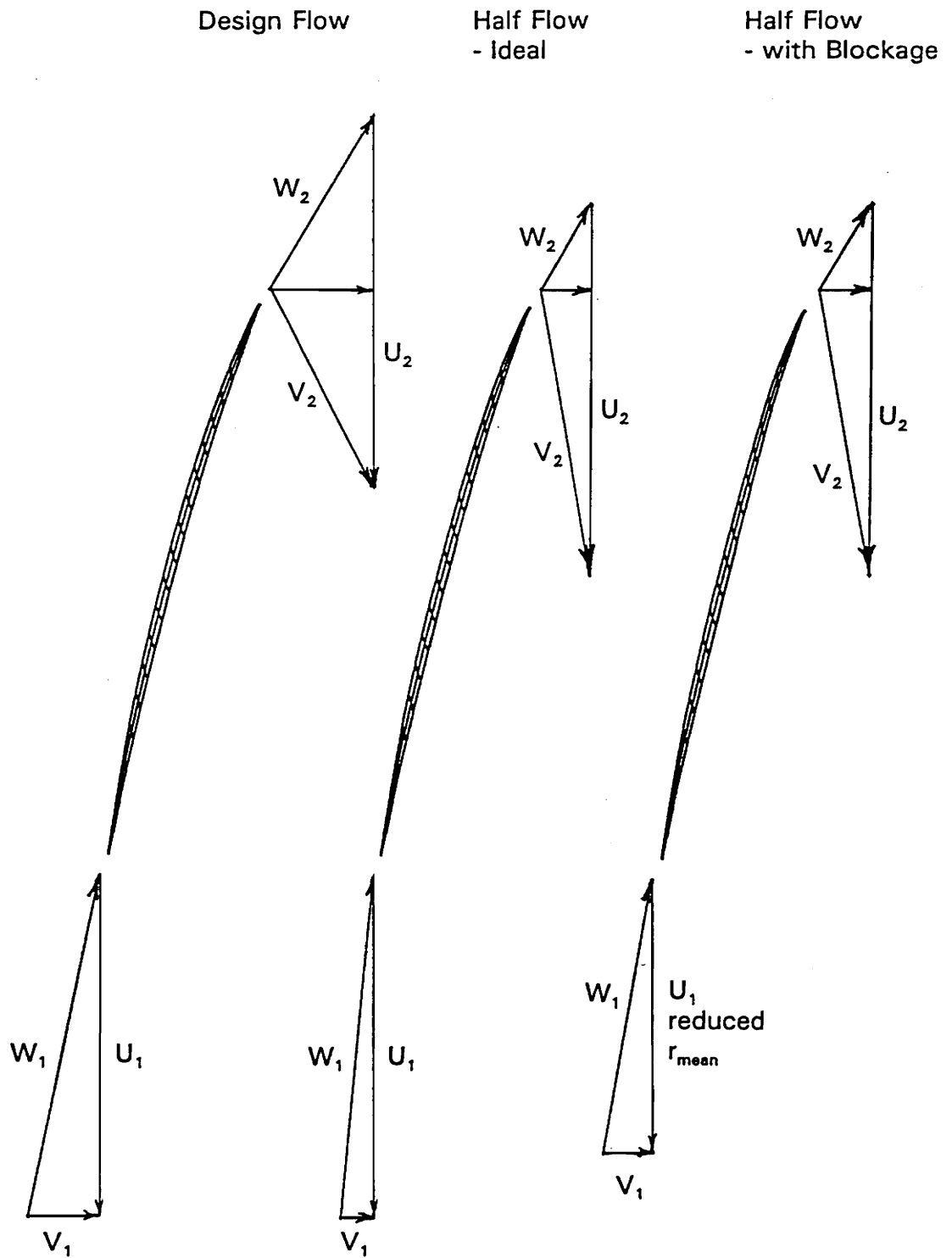


Figure 8.6 Velocity triangles showing the recirculation region blockage effects

8.4 Moment of Momentum

The tangential moment of momentum equation, derived in Appendix A, is:

$$\begin{aligned}
 & \oint \oint r V_{\theta} \rho u \cdot dA = \\
 & - [\iint P_{\theta+} r dr dz - \iint P_{\theta-} r dr dz] \\
 & + \oint \oint \mu r \left[\frac{\partial W_{\theta}}{\partial r} + \frac{1}{r} \frac{\partial W_r}{\partial \theta} - \frac{W_{\theta}}{r} \right] m_r \cdot dA \\
 & + \oint \oint \mu r^2 \left[\frac{1}{r} \frac{\partial W_{\theta}}{\partial \theta} + \frac{W_r}{r} \right] m_{\theta} \cdot dA \\
 & + \oint \oint \mu r \left[\frac{\partial W_{\theta}}{\partial z} + \frac{1}{r} \frac{\partial W_z}{\partial \theta} \right] m_z \cdot dA
 \end{aligned} \tag{1}$$

The left side of the equation is the work term, rV_{θ} . The right side of the equation was further broken down into torques due to the following components: pressure across the blades, shear on the rotor and shear on the shroud. The shear on the rotor includes the blades, the hub, and the tip.

The equation was also expressed in the form used by Moore, Le Fur, and Moore (9). For steady flow through the inducer rotor, the rate of change of moment of momentum, rV_{θ} , equals the torque acting on the fluid. For the flow entering the inducer at the inlet, i , and leaving at the exit, 2 ,

$$\dot{m}(\overline{r_2 V_{\theta 2}} - \overline{r_i V_{\theta i}}) = T_P + T_{Sr} - T_{Ss} \tag{2}$$

where the terms T represent contributions to the torque and \dot{m} is the mass flow rate. T_P is the torque due to the blade pressure forces; the work done by the pressure forces is thermodynamically reversible. The terms T_S represent the torques due to wall shear stresses. The rotor shear torque, T_{Sr} , combines the shear torques on the blade, hub, and unshrouded blade tip surfaces. At the stationary shroud wall, T_{Ss} , is an opposing torque which acts to dissipate some of the moment of momentum imparted by the inducer. All the contributions from the shear stresses are irreversible.

All the components were integrated from the calculated flow field and listed in Table 8.4. The integrations were carried out from upstream of the recirculation region to the trailing edge, from hub to shroud, and from blade to blade. The development of the moment of momentum components may be seen in Figure 8.7. To be sure the sum of the components equalled the work, the pressure term was calculated by difference,

$$T_P = \dot{m}rV_{\theta} - T_{Sr} - T_{Ss} \quad (3)$$

and the integrated pressure term was used to verify the result. This is different from the SEP inducer analysis, which determined the blade shear by difference.

The shear on the blades was checked by hand assuming steady turbulent flow over a flat plate. A blade shear torque of 1.5 Nm was calculated by hand to compare with the 1.6 Nm obtained from the integration. Since the two are very close, integrated blade shear torque can be trusted. The sum of the pressure and shear terms was also checked to verify that it equalled the work term.

Following Moore, Le Fur, and Moore (9) again, the moment of momentum is normalized with $U_{tip}^2/2\omega$ to be consistent with Lakshminarayana's definitions of head rise coefficient. Thus equation 2 becomes

$$\frac{2\omega}{U_{tip}^2}(\overline{r_2 V_{\theta 2}} - \overline{r_i V_{\theta i}}) = \frac{2\omega}{\dot{m}U_{tip}^2}[T_P + T_{Sr} - T_{Ss}] \quad (4)$$

Defining a moment of momentum coefficient, ψ_E , and torque coefficients, ψ_T , equation 4 reduces to

$$\begin{aligned} \psi_{E2} - \psi_{Ei} &= \psi_{TP} + \psi_{TSr} - \psi_{TSs} \\ 0.594 - 0.001 &= 0.565 + 0.044 - 0.016 \end{aligned} \quad (5)$$

The numbers beneath each term in equation 5 were evaluated from the flow calculation results in Table 8.4. Note that in Figure 8.7 the work at the inducer leading edge is negative, because the rotor has done work on the fluid and some of the work is dissipated at the shroud in the recirculation region. Therefore, the inlet plane considered here is upstream of the recirculation region.

Table 8.4 Moment of Momentum Components through the Inducer

A	$\dot{m}rV_\theta$	=	ΣT	=	T_p	+	T_{sr}	+	T_{sr}	+	shear on blade pressure side	+	shear on suction side	shear tip
	work		sum of torques		pressure gradient (integrated) (difference)		shear on shroud		shear on hub		shear on blade pressure side		shear on suction side	shear tip
-0.3750	0.0826		-0.0095		0.0000		-0.0095		0.0000		0.0000		0.0000	0.0000
-0.2500	0.0585		-0.0368		0.0953		-0.0368		0.0000		0.0000		0.0000	0.0000
-0.1700	-0.0426		-0.0675		0.0000		-0.0675		0.0000		0.0000		0.0000	0.0000
-0.1300	-0.2060		-0.0964		-0.1096		-0.0964		0.0000		0.0000		0.0000	0.0000
-0.1080	-0.3032		-0.1282		0.0000		-0.1282		0.0000		0.0000		0.0000	0.0000
-0.1000	-0.3322		-0.1492		-0.1830		-0.1492		0.0000		0.0000		0.0000	0.0000
-0.0800	-0.3238		-0.1621		0.0000		-0.1621		0.0000		0.0000		0.0000	0.0000
-0.0450	-0.3349		-0.1701		-0.1648		-0.1701		0.0000		0.0000		0.0000	0.0000
-0.0200	-0.3777		-0.1766		-0.2011		-0.1766		0.0000		0.0000		0.0000	0.0000
-0.0060	-0.3719		-0.1817		0.0000		-0.1817		0.0000		0.0000		0.0000	0.0000
0.0000	-0.2723		-0.1519		-0.0960		-0.1833		0.0002		0.0011		0.0056	0.0000
0.0227	-0.1748		-0.1061		-0.0098		-0.1848		0.0004		0.0051		0.0143	0.0000
0.0455	0.0074		0.1283		0.1219		-0.1878		0.0007		0.0189		0.0536	0.0002
0.0682	0.2583		0.3784		0.3199		-0.1916		0.0011		0.0374		0.0891	0.0004
0.0909	0.7883		1.1087		0.7414		-0.2037		0.0022		0.0891		0.1578	0.0015
0.1364	1.6038		1.9887		1.8403		-0.2166		0.0034		0.1341		0.2247	0.0030
0.1818	2.5161		3.0472		2.8054		-0.2310		0.0047		0.1754		0.2880	0.0048
0.2273	3.5541		4.2841		3.9576		-0.2462		0.0061		0.2120		0.3478	0.0068
0.2727	4.6931		5.6944		5.2909		-0.2621		0.0076		0.2440		0.4050	0.0090
0.3182	5.9623		7.2336		6.7603		-0.2792		0.0093		0.2724		0.4596	0.0112
0.3636	7.3406		8.8600		8.3239		-0.2973		0.0111		0.2981		0.5110	0.0132
0.4091	8.8011		10.5352		9.9437		-0.3168		0.0130		0.3215		0.5587	0.0151
0.4545	10.3010		12.1839		11.5437		-0.3377		0.0148		0.3433		0.6029	0.0169
0.5000	11.7759		13.7264		13.0421		-0.3589		0.0168		0.3644		0.6437	0.0184
0.5455	13.1908		15.1322		14.4083		-0.3808		0.0190		0.3848		0.6811	0.0198
0.5909	14.5220		16.3910		15.6312		-0.4029		0.0215		0.4049		0.7152	0.0211
0.6364	15.7586		17.4805		16.6868		-0.4249		0.0244		0.4251		0.7468	0.0222
0.6818	16.8739		18.3763		17.5496		-0.4468		0.0280		0.4458		0.7763	0.0234
0.7273	17.8551		19.0659		18.2053		-0.4684		0.0324		0.4675		0.8043	0.0244
0.7727	18.6874		19.5502		18.6543		-0.4884		0.0378		0.4903		0.8310	0.0253
0.8182	19.3958		19.8237		18.8914		-0.5086		0.0442		0.5141		0.8564	0.0262
0.8636	20.0005		19.8587		18.8896		-0.5294		0.0518		0.5389		0.8809	0.0271
0.9091	20.3884		19.6901		18.7032		-0.5402		0.0588		0.5516		0.8922	0.0281
0.9318	20.5784		20.4872		19.4884		-0.5458		0.0588		0.5644		0.8943	0.0271
0.9545	20.6764		20.4918		19.4901		-0.5477		0.0596		0.5670		0.8957	0.0271
0.9773	20.7007		20.5083		19.5055		-0.5491		0.0601		0.5689		0.8958	0.0271

l.e.

t.e.

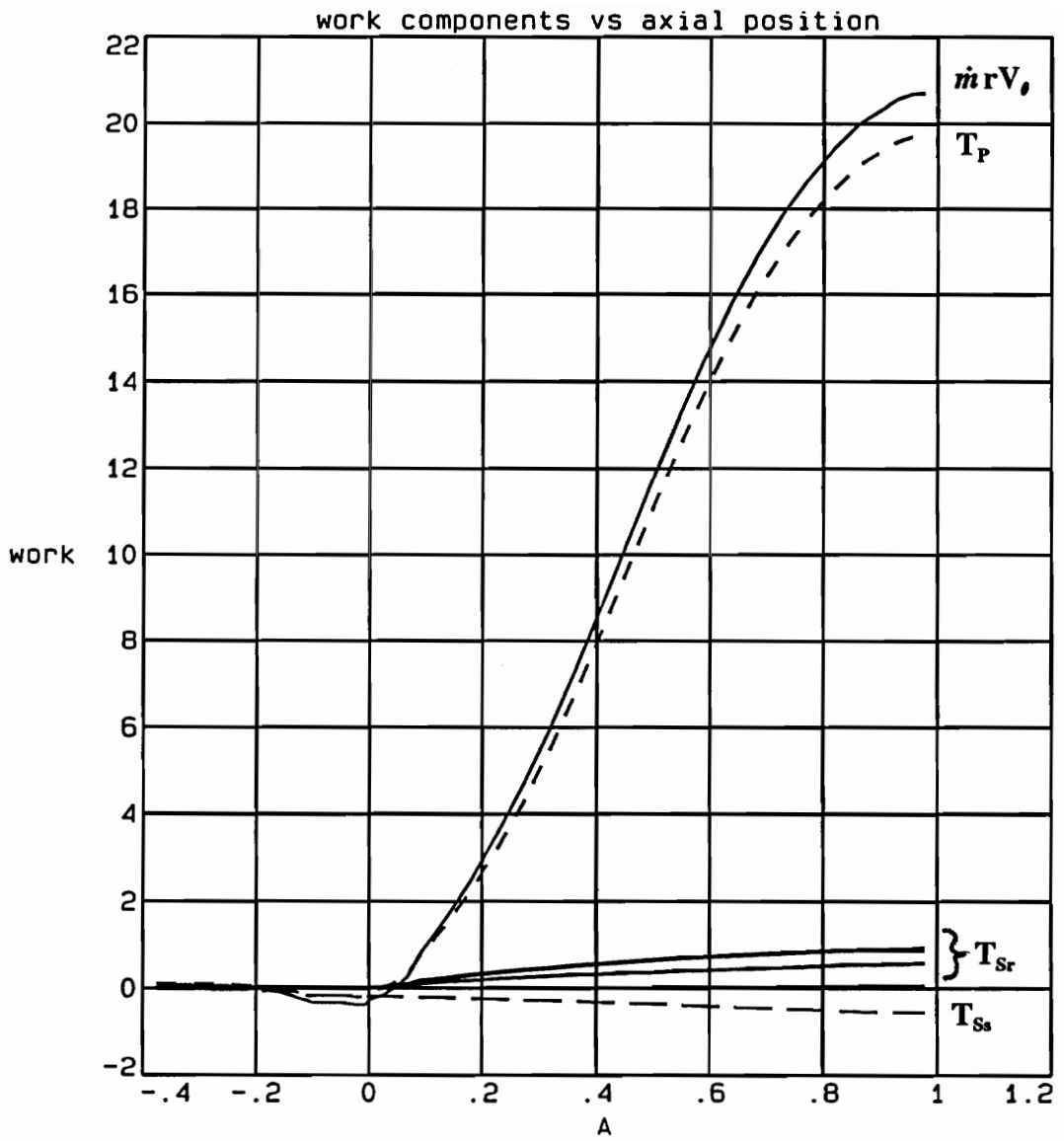


Figure 8.7 **Development of work through the inducer**

Considered another way,

$$\begin{aligned}
 \text{Work input to fluid} &= \psi_{TP} + \psi_{TSr} \\
 &= 0.565 + 0.044 \\
 &= \psi_{E2} - \psi_{Ei} + \psi_{TSs} \\
 &= 0.594 - 0.001 + 0.016 \\
 &= 0.609
 \end{aligned} \tag{6}$$

Notice from Figure 8.7 that 93% of the work done in the inducer is by the pressure forces, ψ_{TP} . The rest of the work, about 7%, is done by the shear on the blades, ψ_{TSr} . By the exit 2.6% of the total work is dissipated at the stationary shroud, ψ_{TSs} . Referring back to Figure 2.10, the SEP inducer was quite different from the Rocketdyne inducer. The SEP inducer produced 40% of the work by shear forces and only 60% by pressure forces. Also, 4.5% of that work was dissipated at the shroud wall before the rotor exit. There are two reasons for these differences. The Rocketdyne inducer has about three times the blade loading and thus its pressure forces are three times higher. The Rocketdyne inducer was also tested in water instead of air so the Reynolds number is about seven times higher and the shear forces are smaller.

8.5 Efficiency

An absolute total pressure coefficient is defined by

$$\psi_t = \frac{P_t - P_0}{\frac{1}{2}\rho U_{tip}^2} \tag{7}$$

In general,

$$\psi_t = \psi_E - \psi_{loss} \tag{8}$$

The efficiency was also calculated from the moment of momentum information using equations 6 and 8, as follows.

$$\begin{aligned}
 \eta &= \frac{\text{total pressure rise}}{\text{work}} \\
 &= \frac{\delta \psi_t}{\psi_E + \psi_{TSs}} \quad (9) \\
 &= \frac{\psi_E - \psi_{loss}}{\psi_E + \psi_{TSs}}
 \end{aligned}$$

ψ_E , and ψ_{loss} come from Table 8.3. The shroud shear torque, T_{Ss} , from Table 8.4 is used to calculate ψ_{TSs} . T_{Ss} is assumed constant with flow rate since it is considered a function of blade speed alone. The coefficients used are evaluated from leading edge to trailing edge to be consistent with the standard efficiency calculations.

$$\eta_{100} = \frac{0.604 - 0.053}{0.604 + 0.0157} = .889$$

$$\eta_{89} = \frac{0.699 - 0.058}{0.699 + 0.0157} = .897$$

$$\eta_{110} = \frac{0.527 - 0.051}{0.527 + 0.0157} = .877$$

Notice the efficiency decreases with increasing flow rate implying that the peak efficiency occurs below 89% design flow rate.

9 CONCLUSIONS

A 3-D Navier-Stokes flow code, the Moore Elliptic Flow Program, MEFP, was used to predict the flow field and the performance of a Rocketdyne inducer. The same low flow coefficient inducer was also tested by Rocketdyne using 3-D laser anemometry. The computational analysis performed using MEFP revealed the flow patterns in areas of the flow that were experimentally unobservable, such as near the blades, near the shroud, and in the recirculation region. The calculated flow field compared very well to the laser velocimetry data. The flow distributions on the internal data planes as well as the overall exit profiles agreed surprisingly well. The calculation matched the measured flow field well enough that the predicted flow patterns are believable, even in the unobservable regions. The calculation did overpredict the work and the head rise by about 20%. It was concluded that this was probably due to the trailing edge shape in the calculation grid, and its effect on the blade unloading characteristics.

This study has demonstrated that MEFP can be used to predict low flow coefficient inducer flow and performance at both design and off-design conditions. Also, it may be noted that the calculations were performed on a workstation, not on a mainframe computer.

The recirculation region is a toroidal shaped vortex that forms along the shroud at the leading edge of the blades. The recirculation is mainly driven by tip leakage flow. The computational analysis provided an accurate representation of the recirculation region. The recirculation region increased in length with decreasing flow rate. The backflow extended upstream one twelfth of the tip diameter at 110% of design flow rate. At 89% of design flow rate the length increased to one half the tip diameter.

The calculation results also quantified the recirculation region's effects on the rest of the flow field and on the inducer performance. The recirculation region acts as a blockage which reduces the effective mean inlet radius. It was found that the recirculation blockage modifies the influence of the relative velocity effect, $W_1^2 - W_2^2$, and the centrifugal effect, $U_2^2 - U_1^2$, on the performance characteristic. Normally, without a

blockage, the centrifugal effect would be constant with flow rate. The relative velocity effect normally decreases with increasing flow rate, and defines the shape of the pump characteristic. With the blockage, however, the relative velocity effect increases and the centrifugal effect decreases with increasing flow rate. This was seen in the computed pump characteristic. The centrifugal effect and the change in absolute kinetic energy determine the shape of this pump characteristic.

The contributions to changes in moment of momentum were found by integrating the calculated pressure and shear forces over the inducer surfaces. The development of the work and its components could then be seen. At the design flow rate, the pressure forces, ψ_{TP} , produce 93% of the work done in the inducer. The rest of the work, about 7%, is done by the shear on the blades, ψ_{TSr} . By the exit of the inducer, 2.6% of the total work is dissipated at the stationary shroud, ψ_{TSs} . The inducer efficiency is 89% at design flow rate. The efficiency increases with decreasing flow rate between 89% and 110% design flow rate, implying that the peak efficiency occurs below 89% of design flow rate.

In comparison to the SEP inducer previously studied by J. Moore, T. Le Fur, and J. G. Moore (9), the Rocketdyne inducer has a significant contribution from the change in relative kinetic energy. In fact, at the design flow rate, the relative kinetic energy change is about the same as the contribution from the centrifugal effect. The SEP inducer was quite different from the Rocketdyne inducer. The SEP inducer produced 40% of the work by shear forces and only 60% by pressure forces. Also, 4.5% of that work was dissipated at the shroud wall before the rotor exit. The efficiency was about 64%, which is much lower than that of the Rocketdyne inducer.

BIBLIOGRAPHY

- 1 Furst, R.B., "SSME Turbopump Design", Society of Automotive Engineers, National Aerospace Engineering and Manufacturing Meeting, SAE Paper 730926, 1973.
- 2 Furst, R.B., "SSME Turbopump Design and Performance", AIAA Paper 75-1301, 1975.
- 3 Lakshminarayana, B., "Fluid Dynamics of Inducers - A Review," Transactions of the ASME, Journal of Fluids Engineering, Vol.104, pp.411-427, December 1982.
- 4 Lakshminarayana, B., "Experimental and Analytical Investigation of Flow Through a Rocket Pump Inducer", Fluid Mechanics and Design Turbomachinery, NASA SP 304, pp.689-723, 1974.
- 5 Abramian, M., Howard, J. H. G., and Hermann, P., "An Investigation of Axial Pump Backflow and a Method for its Control", ASME Paper No. 88-GT-31, June 1988.
- 6 Boccazzi, A., Perdichizzi, A., Tabacco, U., "Flow Field Investigation in a Low Solidity Inducer by Laser Doppler Velocimeter", ASME Paper, 89-GT-54, June 1989.
- 7 Bario, F., Barral, L., and Bois, G., "Air Test Flow Analysis of the Hydrogen Pump of VULCAIN Rocket Engine," Pumping Machinery-1989, FED, Vol.81, July 1989.
- 8 Le Fur, T., "Computational Study of 3D Turbulent Air Flow in a Helical Rocket Pump Inducer", M.S.Thesis, VPI&SU, December 1989.
- 9 Moore, J., Le Fur, T., Moore, J. G., "Computational Study of 3-D Turbulent Air Flow in a Helical Rocket Pump Inducer", AIAA Paper 90-2123, July 1990.
- 10 Excoffon, T., "3-D Flow and Performance of a Tandem-Bladed Rocket Pump Inducer", M.S.Thesis, VPI&SU, April 1992.
- 11 Moore, J., Moore, J. G., Lupi, A., "Use of Blade Lean in Turbomachinery Design", Eleventh Workshop for Computational Fluid Dynamic Applications in Rocket Propulsion, NASA CP-3221, Part 1, 1993.

- 12 Lupi, A., "CFD Analysis and Redesign of Centrifugal Impeller Flows for Rocket Pumps", M.S.Thesis, VPI&SU, December 1993.
- 13 Moore, J. G., Moore, J., "The Moore Elliptic Flow Program for Turbomachinery Flow Calculations 1990 Users Guide", Turbomachinery Research Group, Report No. JM/90-3, Mechanical Engineering Department, VPI&SU, February 1990.
- 14 Moore, J. G., "An Elliptic Calculation Procedure for 3-D Viscous Flow", AGARD Lecture Series No. 140 on 3-D Techniques Applied to Internal Flows in Propulsion Systems, Rome, Italy, Cologne, West Germany, Paris, France, June 1985.
- 15 Moore, J. G., Doan, A., Moore, J., "3-D Flow Calculations for the ADP Inducer at Design and Off-Design Conditions", Turbomachinery Research Group, Report No. JM/94-2, Mechanical Engineering Department, VPI&SU, March 1994.
- 16 Rojas L., Brozowski L.A., Ferguson T.V., "Pump CFD Code Validation Tests Status", NASA Marshall Pump Consortium Meeting, Huntsville AL, July 28 1993.
- 17 Rojas L., Brozowski L.A., Ferguson T.V., "Pump CFD Code Validation Tests ADP Inducer Data Summary", NASA Marshall Pump Consortium Meeting, Huntsville AL, October 27 1993.
- 18 Brozowski L.A., Ferguson T.V., Rojas L., "Three-Dimensional Inducer Flow Field Characterization", 12th Workshop for Computational Fluid Dynamics Applications in Rocket Propulsion, NASA Marshall Space Flight Center, Huntsville AL, April 19-21 1994.
- 19 Moore, J.G., "Evaluation of the Curvature/Rotation Force Terms", Turbomachinery Research Group, Report No. JM/92-5, Mechanical Engineering Department, VPI&SU, June 1992.
- 20 Moore, J., Personal Communications, August 1994.

APPENDIX A

Derivation of tangential Moment of Momentum Equation

The tangential momentum equation, derived in reference 19, is

$$\begin{aligned}
 & \rho W \cdot \nabla W_\theta + 2\rho W_r \omega + \rho W_\theta \frac{W_r}{r} = \\
 & - \frac{1}{r} \frac{\partial P}{\partial \theta} \\
 & + \nabla \cdot \mu \nabla (W_\theta + \omega r) \\
 & + \nabla \cdot \frac{\mu}{r} \left[m_r \frac{\partial W_r}{\partial \theta} + m_\theta \frac{\partial (W_\theta + \omega r)}{\partial \theta} + m_z \frac{\partial W_z}{\partial \theta} \right] \\
 & + \nabla \cdot \frac{\mu}{r} [2m_\theta W_r - m_r (W_\theta + \omega r)] \\
 & + \frac{\mu}{r} \left[\frac{\partial (W_\theta + \omega r)}{\partial r} - \frac{W_\theta + \omega r}{r} + \frac{1}{r} \frac{\partial W_r}{\partial \theta} \right]
 \end{aligned} \tag{A.1}$$

To get the integral form of the tangential moment of momentum equation, the tangential momentum equation, equ. 1, is multiplied by radius then integrated over a volume. The following equations will be useful in manipulating the terms of the equation.

$$\rho W \cdot \nabla W_\theta = \nabla \cdot \rho W W_\theta \quad \text{because} \quad \nabla \cdot \rho W = 0 \tag{A.2}$$

$$\iiint_{vol} \nabla \cdot \rho W W_\theta dvol = \oiint_{area} W_\theta \rho W \cdot dA \tag{A.3}$$

$$W \cdot \nabla r = W \cdot m_r = W_r \quad (\text{A.4})$$

$$W \cdot \nabla r = W \cdot m_r = W_r \quad (\text{A.5})$$

The convection term for the moment of momentum equation will take the form:

$$\nabla \cdot \rho W r V_\theta \quad (\text{A.6})$$

This convection term, eq. 6, can be manipulated as follows to equal the radius times the convection term in equation 1.

$$\begin{aligned} &= \nabla \cdot \rho W r (W_\theta + \omega r) \\ &= r \nabla \cdot \rho W (W_\theta + \omega r) + (W_\theta + \omega r) \rho W \cdot \nabla r \\ &= (r \nabla \cdot \rho W W_\theta + \omega r \rho W \cdot \nabla r) + (W_\theta \rho W \cdot \nabla r + \omega r \rho W \cdot \nabla r) \\ &= r \nabla \cdot \rho W W_\theta + 2 \omega r \rho W_r + W_\theta \rho W_r \\ &= r \left[\rho W \cdot \nabla W_\theta + 2 \rho \omega W_r + \frac{W_\theta \rho W_r}{r} \right] \end{aligned} \quad (\text{A.7})$$

The integral form of the convection term is

$$\iiint \nabla \cdot \rho W r V_\theta dvol = \oint \oint r V_\theta \rho W \cdot dA \quad (\text{A.8})$$

The integral form of the pressure term is

$$\begin{aligned}
 & \iiint r \left(-\frac{1}{r} \frac{\partial P}{\partial \theta} \right) dvol \\
 &= - \iiint \frac{\partial P}{\partial \theta} dvol \\
 &= - \iint \left(\int \frac{dP}{d\theta} d\theta \right) r dr dz \\
 &= - \left[\iint P_{pressure} r dr dz - \iint P_{suction} r dr dz \right]
 \end{aligned} \tag{A.9}$$

There are four shear terms in the tangential moment of momentum equation.

$$\begin{aligned}
 & r \nabla \cdot \frac{\mu}{r} \left(m_r \frac{\partial W_r}{\partial \theta} + m_\theta \frac{\partial (W_\theta + \omega r)}{\partial \theta} + m_z \frac{\partial W_z}{\partial \theta} \right) \\
 &= \nabla \cdot \mu \left(m_r \frac{\partial W_r}{\partial \theta} + m_\theta \frac{\partial (W_\theta + \omega r)}{\partial \theta} + m_z \frac{\partial W_z}{\partial \theta} \right) - \frac{\mu}{r} \frac{\partial W_r}{\partial \theta}
 \end{aligned} \tag{A.10}$$

$$\begin{aligned}
 & r \nabla \cdot \mu \nabla (W_\theta + \omega r) \\
 &= \nabla \cdot r \mu \nabla (W_\theta + \omega r) - \mu [\nabla (W_\theta + \omega r)] \nabla r \\
 &= \nabla \cdot r \mu \nabla (W_\theta + \omega r) - \mu \frac{\partial}{\partial r} (W_\theta + \omega r)
 \end{aligned} \tag{A.11}$$

$$\begin{aligned}
 & r \nabla \cdot \frac{\mu}{r} [2m_\theta W_r - m_r (W_\theta + \omega r)] \\
 &= \nabla \cdot \mu [2m_\theta W_r - m_r (W_\theta + \omega r)] + \frac{\mu}{r} (W_\theta + \omega r)
 \end{aligned} \tag{A.12}$$

$$\mu \frac{\partial (W_\theta + \omega r)}{\partial r} - \frac{\mu}{r} (W_\theta + \omega r) + \frac{\mu}{r} \frac{\partial W_r}{\partial \theta} \tag{A.13}$$

The four shear terms, 10 through 13, combine to form

$$\begin{aligned}
 & \nabla \cdot \mu [r \nabla (W_\theta + \omega r) \\
 & + m_r \frac{\partial W_r}{\partial \theta} + m_\theta \frac{\partial (W_\theta + \omega r)}{\partial \theta} + m_z \frac{\partial W_z}{\partial \theta} \\
 & + 2m_\theta W_r - m_r (W_\theta + \omega r)]
 \end{aligned} \tag{A.14}$$

The first term in equation 14 is broken down as follows.

$$\begin{aligned}
 r \nabla (W_\theta + \omega r) &= m_r r \frac{\partial (W_\theta + \omega r)}{\partial r} \\
 &+ m_\theta \frac{r}{r} \frac{\partial (W_\theta + \omega r)}{\partial \theta} + m_z r \frac{\partial (W_\theta + \omega r)}{\partial z}
 \end{aligned} \tag{A.15}$$

Equation 15 is substituted into equation 14 to yield

$$\begin{aligned}
 & \nabla \cdot \mu \left\{ m_r \left[r \frac{\partial (W_\theta + \omega r)}{\partial r} + \frac{\partial W_r}{\partial \theta} - (W_\theta + \omega r) \right] \right. \\
 & + m_\theta \left[\frac{\partial (W_\theta + \omega r)}{\partial \theta} + \frac{\partial (W_\theta + \omega r)}{\partial \theta} + 2W_r \right] \\
 & \left. + m_z \left[r \frac{\partial (W_\theta + \omega r)}{\partial z} + \frac{\partial W_z}{\partial \theta} \right] \right\}
 \end{aligned} \tag{A.16}$$

which simplifies to

$$\begin{aligned}
 & \nabla \cdot \mu \left(m_r \left[r \frac{\partial W_\theta}{\partial r} + \frac{\partial W_r}{\partial \theta} - W_\theta \right] \right. \\
 & + m_\theta 2 \left[\frac{\partial W_\theta}{\partial \theta} + W_r \right] \\
 & \left. + m_z \left[r \frac{\partial W_\theta}{\partial z} + \frac{\partial W_z}{\partial \theta} \right] \right)
 \end{aligned} \tag{A.17}$$

pulling out an r gives

$$\begin{aligned}
 \nabla \cdot \mu r \{ & m_r \left[\frac{\partial W_\theta}{\partial r} + \frac{1}{r} \frac{\partial W_r}{\partial \theta} - \frac{W_\theta}{r} \right] \\
 & + m_\theta 2 \left[\frac{1}{r} \frac{\partial W_\theta}{\partial \theta} + \frac{W_r}{r} \right] \\
 & + m_z \left[\frac{\partial W_\theta}{\partial z} + \frac{1}{r} \frac{\partial W_z}{\partial \theta} \right] \}
 \end{aligned} \tag{A.18}$$

The volume integral shear term is of the form

$$\iiint \nabla \cdot \mu r \{ \ } dvol = \oint \oint \mu r \{ \ } \cdot dA \tag{A.19}$$

The integral form of the tangential moment of momentum equation is formed by combining the convection term (8), pressure term (9), and shear term (18,19) as follows.

$$\begin{aligned}
 \oint \oint r V_{\theta\rho} W \cdot dA = & \\
 - [\iint P_{\theta+} r dr dz - \iint P_{\theta-} r dr dz] & \\
 + \oint \oint \mu r \left[\frac{\partial W_\theta}{\partial r} + \frac{1}{r} \frac{\partial W_r}{\partial \theta} - \frac{W_\theta}{r} \right] m_r \cdot dA & \\
 + \oint \oint \mu r 2 \left[\frac{1}{r} \frac{\partial W_\theta}{\partial \theta} + \frac{W_r}{r} \right] m_\theta \cdot dA & \\
 + \oint \oint \mu r \left[\frac{\partial W_\theta}{\partial z} + \frac{1}{r} \frac{\partial W_z}{\partial \theta} \right] m_z \cdot dA &
 \end{aligned} \tag{A.20}$$

APPENDIX B

Rotary Stagnation Pressure, P^* (reference 20)

Rotary stagnation pressure is conserved along a streamline in steady, inviscid flow in a rotor. For steady, inviscid flow in a rotor the momentum equation may be written

$$(W \cdot \nabla)W = -\frac{1}{\rho}\nabla P - 2\omega \times W - \omega \times (\omega \times r) \quad (\text{B.1})$$

Using the vector identity

$$2(W \cdot \nabla)W + 2W \times (\nabla \times W) = \nabla(W \cdot W) \quad (\text{B.2})$$

equation B.1 becomes

$$\frac{1}{2}\nabla(W \cdot W) - W \times (\nabla \times W) = -\frac{1}{\rho}\nabla P - 2\omega \times W - \omega \times (\omega \times r) \quad (\text{B.3})$$

$$\text{or} \quad W \times (\nabla \times W + 2\omega) = \frac{1}{\rho}\nabla P + \frac{1}{2}\nabla W^2 - \frac{1}{2}\nabla \omega^2 r^2 \quad (\text{B.4})$$

Now, for incompressible flow, $\nabla \rho = 0$, therefore

$$W \times (\nabla \times W + 2\omega) = \frac{1}{\rho}\nabla(P + \frac{1}{2}\rho W^2 - \frac{1}{2}\rho \omega^2 r^2) \quad (\text{B.5})$$

$$\text{and} \quad W \times (\nabla \times W + 2\omega) = \frac{1}{\rho}\nabla P^* \quad (\text{B.6})$$

Taking the dot product of W with equation B.6 yields

$$W \cdot \nabla P^* = 0 \quad (\text{B.7})$$

which shows that P^* is constant along a streamline.

Flow with uniform P^* at the inlet will have uniform P^* throughout the flowfield.

With axial flow at the inlet,

$$P^* = P + \frac{1}{2}\rho W^2 - \frac{1}{2}\rho\omega^2 r^2 = P + \frac{1}{2}\rho V^2 = P_t \quad (\text{B.8})$$

Rotary stagnation pressure losses in a rotor can be expressed as

$$\begin{aligned} & P_{t,max,inlet} - P^* \\ \text{or} & P_o - P^* \end{aligned} \quad (\text{B.9})$$

and a loss coefficient is defined as

$$\frac{P_o - P^*}{\frac{1}{2}\rho U_{tip}^2} \quad (\text{B.10})$$

For steady, viscous flow in a rotor, the rotary stagnation pressure loss coefficient (B.10) is used as a measure of the losses.

VITA

Andrew Doan was born in Jacksonville, Arkansas, to Kenneth and Barbara Doan on July 16, 1970. He grew up in Winchester, Virginia, where he graduated from James Wood High School in 1988. That year he entered Virginia Polytechnic Institute and State University. He received a Bachelor of Science degree in Mechanical Engineering in May 1993. During his undergraduate studies, he gained four semesters of cooperative education (co-op) experience at Newport News Shipbuilding. He was also a member of the Virginia Tech Solar Car team, and participated in Sunrayce '93. In August 1993, he returned to Virginia Polytechnic Institute and State University to earn a Master of Science degree in Mechanical Engineering. At the completion of his thesis he will go wherever God provides.

Andrew W. Doan